DISSERTATION

Novel phenomena in multiferroic rare-earth metal oxides

ausgeführt zum Zwecke der Erlangung des akademischen Grades eines Doktors der Naturwissenschaften, eingereicht an der TU Wien, Fakultät für Physik, von

Janek Wettstein
Matrikelnummer: 11935988

unter der Leitung von

Dr. Dávid Szaller

und

Univ.Prof. Dr. Andrei Pimenov
Institut für Festkörperphysik, E138

Wien, 14. Oktober 2023

Begutachtet von

.....	.....
Prof. Wilfried Schranz	Prof. István Kézsmárki

Ich nehme zur Kenntnis, dass ich zur Drucklegung dieser Arbeit nur mit Bewilligung der Prüfungskommission berechtigt bin.

Eidesstattliche Erklärung
Ich erkläre an Eides statt, dass die vorliegende Arbeit nach den anerkannten Grundsätzen für wissenschaftliche Abhandlungen von mir selbstständig erstellt wurde. Alle verwendeten Hilfsmittel, insbesondere die zugrunde gelegte Literatur, sind in dieser Arbeit genannt und aufgelistet. Die aus den Quellen wörtlich entnommenen Stellen, sind als solche kenntlich gemacht. Das Thema dieser Arbeit wurde von mir bisher weder im In- noch Ausland einer Beurteilerin/einem Beurteiler zur Begutachtung in irgendeiner Form als Prüfungsarbeit vorgelegt. Diese Arbeit stimmt mit der von den Begutachterinnen/Begutachtern beurteilten Arbeit überein. Ich nehme zur Kenntnis, dass die vorgelegte Arbeit mit geeigneten und dem derzeitigen Stand der Technik entsprechenden Mitteln (Plagiat-Erkennungssoftware) elektronisch-technisch überprüft wird. Dies stellt einerseits sicher, dass bei der Erstellung der vorgelegten Arbeit die hohen Qualitätsvorgaben im Rahmen der geltenden Regeln zur Sicherung guter wissenschaftlicher Praxis „Code of Conduct“ an der TU Wien eingehalten wurden. Zum anderen werden durch einen Abgleich mit anderen studentischen Abschlussarbeiten Verletzungen meines persönlichen Urheberrechts vermieden.

Wien, 14. Oktober 2023

. . . . . .

Janek Wettstein

Kurzfassung

In dieser Arbeit wurden neuartige Phänomene in multiferroischen und magnetoelektrischen Materialien erforscht. Magnetoelektrische Materialien zeichnen sich durch eine starke Kopplung zwischen magnetischen und elektrischen Eigenschaften aus, wodurch eine elektrische Polarisation durch Magnetfelder bzw. Magnetisierungen durch elektrische Felder induziert werden können. Aus diesem Grund sind sie von besonderem Interesse für das Schalten von digitalen Informationen, insbesondere für die Datenspeicherung [1]. Trotz großer Fortschritte bei der Erforschung der mikroskopischen magnetoelektrischen Kopplungsmechanismen [2–6], ist es nach wie vor schwierig magnetoelektrische Umschaltprozesse zu steuern. Das liegt an den verschiedenen Symmetrie-Eigenschaften der ferroelektrischen und ferromagnetischen Ordnung, weshalb es noch weiterer Forschung bedarf [1,7–10].
Ziel dieser Arbeit ist es die ungewöhnlichen Eigenschaften von zwei multiferroischen Materialen zu untersuchen, um physikalische Besonderheiten von solchen Systemen besser zu verstehen. Die Experimente in dieser Arbeit wurden mithilfe von statischen und dynamischen Messmethoden durchgeführt.
Das Material Gadolinium Manganit $GdMn_2O_5$ hat eine starke magnetoelektrische Kopplung, wodurch seine sehr große ferroelektrische Polarisation in externen Magnetfeldern umgeschaltet werden kann [11,12]. Wenn ein externes Magnetfeld unter einem „magischen“ Winkel von etwa 10° zur kristallografischen a-Achse angelegt wird, tritt eine ungewöhnliche Hysterese-Kurve mit vier verschiedenen magnetoelektrischen Zuständen auf [13]. Der Ausgangszustand wird erst nach zweimaligem Ein- und wieder Ausschalten des Magnetfeldes erreicht. Dieser Effekt lässt sich gut durch ein semiklassische Spin-Modell erklären. Laut dem Modell rotiert die Hälfte der Spins jedes Mal um etwa 90°, wenn das Magnetfeld ein- bzw. ausgeschaltet wird. Dadurch wirkt $GdMn_2O_5$ wie eine Kurbelwelle, die die lineare Veränderung des externen Magnetfeldes in eine Rotationsbewegung der Spins umwandelt. Dieser magnetoelektrische Schaltprozess findet in einer topologisch geschützten nicht-trivialen Grenzregion zwischen zwei trivialen topologischen Regionen statt, was einen Effekt wie diesen auch in anderen Materialien vermuten lässt. Darüber hinaus ist es möglich den magnetoelektrischen Schaltprozess durch das Anlegen einer konstanten elektrischen Spannung zu kontrollieren, was die Anwendungsmöglichkeiten deutlich erweitert.
In dem multiferroischen Material Samarium-Eisen-Borat $SmFe_3(BO_3)_4$ wird die Wechselwirkung der optisch aktiven Spinwelle (Magnon) der Eisen-Ionen mit der Samarium Quasispin-Anregung in magnetischen Feldern untersucht. Die vermiedene Kreuzung der beiden Anregungen lässt sich gut durch das Dicke-Modell beschreiben, welches zu fundamentalen Modellen der Quantenoptik zählt. Dieses Modell sagt einen Quantenphasenübergang zur sogenannten Superradianz voraus, sofern die Kopplung zwischen den beiden Moden stark genug wird. Aus diesem Grund wurde die Kopplung zwischen den beiden Resonanzen untersucht, sowie der Einfluss verschiedener Parameter auf die Kopplungsstärke erforscht. Es wurde eine Kopplungsstärke von etwa 55% der kritischen Kopplungsstärke erreicht, welche für einen superradianten Phasenübergang erforderlich wäre.

Abstract

In this thesis novel phenomena in multiferroic and magnetoelectric materials are investigated. Magnetoelectric materials are characterized by strong coupling of magnetism and electricity. This enables tuning of electric properties via magnetic fields and vice versa, which is a desired feature for many kinds of electronics. They are especially relevant for manipulation of digital information and for innovative data storage applications [1]. Despite advances in the understanding of microscopic magnetoelectric mechanisms in multiferroic coupling [2–6], magnetoelectric switching is still difficult to realize due to different symmetry properties of ferroelectric and magnetic orders and not sufficiently strong coupling of magnetic and electric degrees of freedom [1,7–10].
The aim of this thesis is to investigate unusual behavior of two multiferroic materials in order to improve our understanding of the properties of these exotic systems. The main experimental methods used in this thesis are measurements of the electric polarization and capacity and dynamical measurements in the terahertz and infrared regimes.
In the first material studied in this thesis, belonging to the $R\mathrm{Mn_2O_5}$ (R = rare-earth ion) crystal family, a novel switching mechanism between various multiferroic states is observed. The rare earth manganites $R\mathrm{Mn_2O_5}$ are of great interest due to colossal magnetoelectric effect in $\mathrm{TbMn_2O_5}$ and $\mathrm{DyMn_2O_5}$ [14,15] and large tunable ferroelectric polarization connected to a strong magnetoelectric coupling in $\mathrm{GdMn_2O_5}$ [11,12]. In this thesis an unusual magnetoelectric switching behavior in multiferroic $\mathrm{GdMn_2O_5}$ is investigated. The application and subsequent removal of a magnetic field reverses the electric polarization of the material and appears together with an unusual 4-state hysteresis cycle [13]. In this cycle half of the spins undergo a rotation of about 90° each time the magnetic field is ramped leading to a full-circle rotation when applying and removing a magnetic field two times in a series. Thus, $\mathrm{GdMn_2O_5}$ acts as a magnetic crankshaft that converts the back-and-forth variations of the magnetic field into a circular spin motion. This peculiar four-state magnetoelectric switching emerges as a topologically protected boundary between different two-state switching regimes. The influence of electric and magnetic fields on the switching process is investigated in detail. It is found that the four magnetoelectric states can be controlled through the application of constant electric voltages during the switching process which opens up new possibilities for magnetoelectric switching.
In the second material, samarium iron borate $\mathrm{SmFe_3(BO_3)_4}$, we focus on the dynamics of magnetic moments. Namely, we investigate the avoided crossing of the optically active low-frequency iron magnon and the Sm quasispin excitations in magnetic fields. The behavior of these modes can be described using the Dicke model, a fundamental model of quantum optics, which predicts a quantum phase transition in an ensemble of non-interacting two-level quantum systems and a bosonic field when the strength of the interaction reaches a sufficiently large critical value [16]. In this superradiant phase, the individual two-level systems begin to radiate coherently through their coupling through the bosonic field. The influence of the superradiant phase on the interaction between the Sm quasi-spin (two-level system) and the Fe spin wave (boson) is discussed and their

interaction strength is tuned by varying density and population of the Sm two-level systems. The interaction strength of the two excitations reaches approx. 55% of the critical value needed for the superradiant phase transition.

Contents

1. Introduction

1.1 Motivation

Multieferroic materials show the simultaneous existence of different ferroic orders such as ferromagnetism, ferroelectricity or ferroelasticity [17]. The presence of several order parameters leads to rich and interesting physics and can have a huge impact on magnetic information storage, spintronics and high-frequency magnetic devices [18]. Especially relevant is the cross-coupling between magnetic and electric order, which is referred to as magnetoelectric coupling [4]. This enables the control of an electric polarization **P** through the application of a magnetic field **H**, and, vice versa the control of a magnetization **M** through an electric field **E**. These properties can be used for novel types of memory storage devices. For example, the possibility to encode information in polarization and magnetization simultaneously allows the realization of four-state logic in one device [19]. On the other hand it is possible to improve modern magnetic random access memories (MRAMs) by manipulating their magnetization through electric voltage instead of currents, as it is done today. This could drastically reduce their high writing energy cost [1]. For this reason, the field of multiferroics is a fast growing community since the last two decades and many new magnetoelectric materials have been discovered since then [3]. The understanding of the microscopic mechanisms in magnetoelectric coupling have been improved drastically [2–6]. However, magnetoelectric switching is still difficult to realize and there is still a lot of research needed to fully understand the basic physics of this material class [1,7–10].
Besides the promising applications, multiferroics show very interesting physics with various exotic phenomena. The coupling between spin and charge degrees of freedom promises non-trivial features in the dynamic properties and elementary excitations in multiferroic materials. One example is the possibility to excite collective magnetic resonances, magnons, through an electric field, the so-called "electromagnons" [20]. Also effects like directional anisotropy could be observed, where the optical properties of a sample differ for the forward

and backward direction of propagation of light [21]. Significant directional anisotropy can be observed in d-d electronic transitions in the near-infrared spectral range [22,23] and in magnon modes in the THz frequency range [24,25]. Directional anisotropy and electromagnons were observed previously in multiferroic $SmFe_3(BO_3)_4$ [26,27] and are also presented in this thesis.

1.2 About this thesis

In this work, two different multiferroic materials are investigated using static and dynamic experimental methods. An overview over the physics of magnetoelectric materials is given in chapter 2. In chapter 3 the experimental setups for the main measurements of this thesis are introduced and the data evaluation is discussed. The quasi-optical measurements in the low THz range (0.2-2 THz) were performed using a Terahertz Time-Domain Spectrometer (THz TDS) and a Fourier Transform Infrared Spectrometer (FTIR). The measurements were conducted in the temperature range from 2-300 K in magnetic fields of up to 30 T. Static experiments were performed using a Physical Measurement Property System (PPMS) which was connected to a Keithley electrometer in order to measure electric polarization at low temperatures in magnetic fields of up to 12 T.
The main body of this thesis contains the experimental results of the measurements of $GdMn_2O_5$ and $SmFe_3(BO_3)_4$ in chapters 4 and 5.
In chapter 4 an unusual topologically protected magnetoelectric four-state hysteresis loop of the multiferroic $GdMn_2O_5$ is investigated. After introducing the general properties of the material, its behavior in magnetic fields is discussed. Typically in this material the application of an external magnetic field along the crystallographic a-axis leads to a reversal of its ferroelectric polarization. Changing the angle under which the magnetic field is applied, heavily influences this behavior. At a "magic" angle of approx 10°, an unusual hysteresis curve is observed, where the magnetic field needs to be applied and removed two times in order to reach the initial state of the sample. A classical spin model is described in order to understand this switching process. Further, it is found that the magnetoelectric switching behavior can be controlled through the application of constant electric fields during the magnetic field sweep.
In chapter 5 the avoided crossing of two resonances in multiferroic $SmFe_3(BO_3)_4$ is discussed in terms of Dicke cooperativity and the influence of a superradiant phase transition on the interaction is investigated. At first, the Dicke model, an important model in quantum optics, is introduced which is followed by the general properties of rare earth iron borates and specifically of $SmFe_3(BO_3)_4$. The origin and excitation conditions of low-frequency magnetic resonances of $SmFe_3(BO_3)_4$ are discussed in detail in order to understand their behavior at different temperatures and magnetic fields. This knowledge is then used to investigate the coupling between the optically active low-frequency magnon of the iron sublattice and the Sm quasispin excitation using the theory derived from the Dicke model. The influence of the superradiant phase on the interaction of the two resonances is explorated for different temperatures and different doping of $Sm_xLa_{1-x}Fe_3(BO_3)_4$ ($x = 0.25, 0.5, 1$).

The conclusion of this work and additional research ideas are provided in chapter 6.

This thesis was completed under the supervision of Prof. Andrei Pimenov and Dr. Dávid Szaller at the Institute of Solid State Physics at TU Wien from 2020 to 2023. The experiments were performed at the TU Wien in the laboratories of the Solid State Spectroscopy Group (PPMS and THz TDS measurements), as well as at the High Field Magnet Laboratory of the Radboud University Nijmegen, Netherlands and the National Institute of Chemical Physics and Biophysics in Tallin, Estonia (high-field measurements with a FTIR).
The experimental work on $SmFe_3(BO_3)_4$ was partially funded by the FWF Austrian Science Fund grants I 2816-N27 and TAI 334-N. Further, this work was funded by the FWF Austrian Science Fund grant I 5539-N.

2. Magnetoelectric coupling

Historically the term magnetoelectric multiferroic described materials with ferroelectric and ferromagnetic orders coexisting in the same phase. Today the term is used in a broader sense where ferroelectricity emerges in the same phase with long-range magnetic orders such as ferromagnetism, ferrimagnetsim and antiferromagnetism. When the electric and magnetic orders are coupled, the material is expected to show strong magnetoelectric (ME) effects. The idea of such a cross-coupling follows from symmetry considerations which were first discussed by Pierre Curie (1894)[28] and by Landau and Lifshitz (1959)[29]. Soon after, the linear magnetoelectric effect in chromium oxide Cr_2O_3 was predicted by Dzyaloshinskii [30] and observed by Astrov [31].
Phenomenologically, the linear magnetoelectric effect can be described by adding an additional ME term

$$F^{\mathrm{me}} = -\chi^{\mathrm{me}}_{\alpha\beta} H_\alpha E_\beta / c \tag{2.1}$$

to the free energy density [4]. In analogy with the magnetic and electric susceptibility, $\chi^{\mathrm{me}}_{\alpha\beta}$ is the magnetoelectric susceptibility tensor. Here α and β are the Cartesian coordinates, c is the speed of light and H_α and E_β are the components of the magnetic and electric field, respectively. Due to this term, external electric fields can induce a magnetization and external magnetic fields can induce an electric polarization. The additional ME contribution to the magnetization and polarization can be described with

$$\Delta M_\alpha = \sqrt{\frac{\varepsilon_0}{\mu_0}} \chi^{\mathrm{me}}_{\alpha\beta} E_\beta \tag{2.2}$$

$$\Delta P_\beta = \frac{1}{c} \chi^{\mathrm{em}}_{\beta\alpha} H_\alpha \,, \tag{2.3}$$

where ε_0 and μ_0 are the vacuum permittivity and permeability, respectively. In the static limit $\chi^{\mathrm{me}}_{\alpha\beta} = \chi^{\mathrm{em}}_{\beta\alpha}$.
According to Neumann's principle the magnetoelectric tensor should reflect the same symmetry as the crystal ("if a crystal is invariant with respect to certain symmetry

elements, any of its physical properties must also be invariant with respect to the same symmetry elements") [32]. That means that the spatial inversion symmetry needs to be broken in order for the magnetoelectric susceptibility to be non-zero. The magnetization **M** and magnetic field **H** are preserved upon inversion symmetry operations while electric polarization **P** and electric field **E** are reversed. Thus the breaking of spatial inversion symmetry connects both quantities. This limits the magnetoelectric effect to material that fulfil this property such as non-centrosymmetric compounds. Other mechanisms that break the inversion symmetry can also lead to magnetoelectric coupling like for example spin ordering.

To date, the identification of the specific mechanism underlying the magnetoelectric effect in each compound remains a subject of ongoing research. A good overview over different proposed mechanisms for various magnetoelectric materials is given in Ref. [3].
Strong magnetoelectric coupling is usually achieved through exchange striction which leads to ferroelectric polarization when the inversion symmetry is broken [4]. For two magnetic moments $\mathbf{S}_1$ and $\mathbf{S}_2$ with the unit vector $\mathbf{r}_{12}$ connecting them, the electric polarization $\mathbf{P}_{12}$ induced through magneto-striction can be described with

$$\mathbf{P}_{12} = P^{\mathrm{ms}}(\mathbf{S}_1 \cdot \mathbf{S}_2)\mathbf{r}_{12}\,, \tag{2.4}$$

where P^{ms} is the magneto-striction coupling constant [33,34]. Such a coupling mechanism is present in $GdMn_2O_5$ which is investigated in chapter 4.

A weaker magnetoelectric coupling mechanism based on the relativistic spin-orbit interaction is also possible. In centrosymmetric materials with a non-collinear ordering of spins, spin-orbit coupling can lead to a spin-current $\mathbf{j}_s \propto \mathbf{S}_1 \times \mathbf{S}_2$ which induces an electric polarization

$$\mathbf{P}_{12} = P^{\mathrm{sc}}\mathbf{r}_{12} \times \mathbf{j}_s = P^{\mathrm{sc}}\mathbf{r}_{12} \times (\mathbf{S}_1 \times \mathbf{S}_2) \tag{2.5}$$

with the spin-current coupling constant P^{sc} [33,35]. This mechanism is also referred to as the inverse Dzyaloshinskii-Moriya mechanism.

Metal-ligand hybridization mechanisms originating from spin-orbit coupling can also lead to a polarization

$$\mathbf{P}_{12} = P^{\mathrm{ml}}((\mathbf{r}_{12} \cdot \mathbf{S}_1)\mathbf{S}_1 - (\mathbf{r}_{12} \cdot \mathbf{S}_2)\mathbf{S}_2) \tag{2.6}$$

with the coupling constant P^{ml} [33,35]. Such a hybridization mechanism is claimed to be present in $SmFe_3(BO_3)_4$, where the electric polarization in the material is induced by two single-ion mechanisms: through displacement of oppositely charged ion sublattices (ionic contribution), and through effective magnetic and crystal fields which produce an electric dipole moment in the electronic $4f$ shell of the rare-earth ion (electronic contribution) [36].

The magnitude of the polarization based on relativistic spin-orbit coupling mechanisms is usually weaker than in the case of magneto-striction mechanisms.

3. Experimental setup

In this chapter the main experimental techniques that were used for this thesis are introduced. The quasi-optical measurements were performed using a Terahertz Time-Domain Spectrometer (section 3.1) and a Fourier-Transform Infrared Spectrometer (section 3.2). Measurements of the electric permittivity $\varepsilon(\omega)$ and electric polarization P at low temperatures and high magnetic fields were conducted in a physical property measurement system (section 3.3).

3.1 Terahertz Time-Domain Spectrometer

A Terahertz Time-Domain Spectrometer (THz-TDS) uses short electromagnetic pulses in the picosecond range which are transmitted through or reflected from a sample. The short pulse consists of a broad spectrum of frequencies from 100 GHz to approx. 4 THz. The amplitude and the phase of the signal are acquired simultaneously by doing a time-resolved measurement of the electromagnetic wave. With the information about the amplitude and phase various optical parameters can be calculated without the need of Kramers Kronig calculations. A typical signal is shown in figure 3.1a.

A THz-TDS consists of a THz part where the THz beam is used for the measurement and an optical part with a femto-second pulsed laser to trigger the start and the measurement of the THz pulse. The THz beam path is inside a chamber which can be purged with nitrogen or evacuated in order to reduce the noise coming from water absorption lines from water in the air.
The Terahertz setup is made out of two antennas which emit and measure the THz signal. The broad THz beam is focused by silicon lenses and guided through the sample using curved golden mirrors. A sketch of the THz TDS is shown in figure 3.2, pictures of the setup at the TU Wien are shown in figure 3.3.s At the TU Wien photoconductive antennas which behave as Hertzian dipoles are used to create and measure the broad-band THz

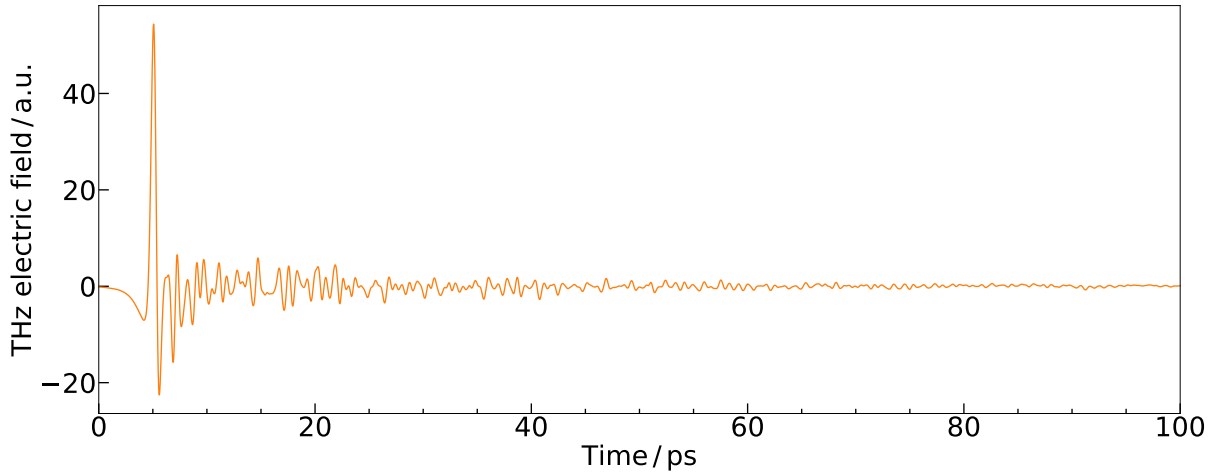

(a) Transmission of a Terahertz Time Domain Spectrometer without a sample in air.

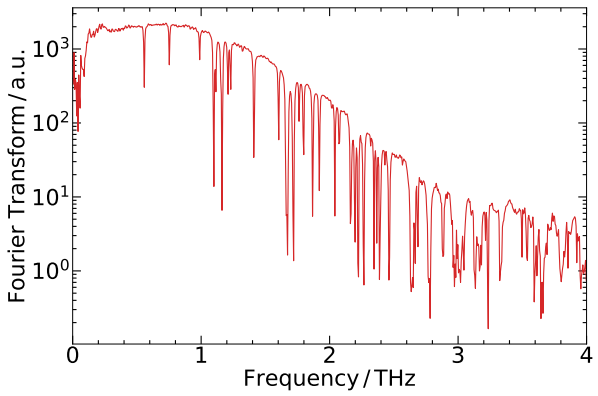

(b) Amplitude of the Fourier Transform of the transmission signal. The negative absorption peaks are excitations of water molecules in the air.

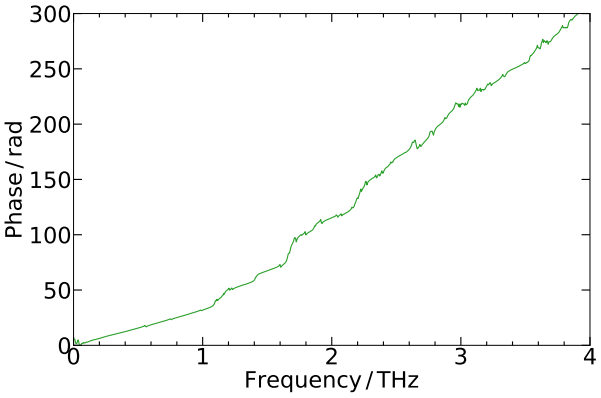

(c) Phase of the Fourier Transform of the transmission signal. Phase discontinuities are seen at resonance frequencies.

Figure 3.1: Measured signal of a THz-TDS in the time-domain (a) with the amplitude (b) and phase (c) of its Fourier transform.

beam. Different ways of creation and detection of a broad-band THz-beam like optical rectification (creation) and magneto-optical sampling (detection) are also possible [37]. A photoconductive antenna consists of a semiconducting surface with two conducting wires on it with a very small gap at one point (see Fig. 3.4). In the emitting antenna a voltage of 30 V is applied at the wires. When the laser pulse hits the semiconductor at the gap between the wires, free charge carriers are created and accelerated due to the applied electric field. This leads to a current between the wires for a short period of time. A change in current creates a varying magnetic field, which in return creates a changing electric field and so on. So the fast change in current leads to an electromagnetic wave

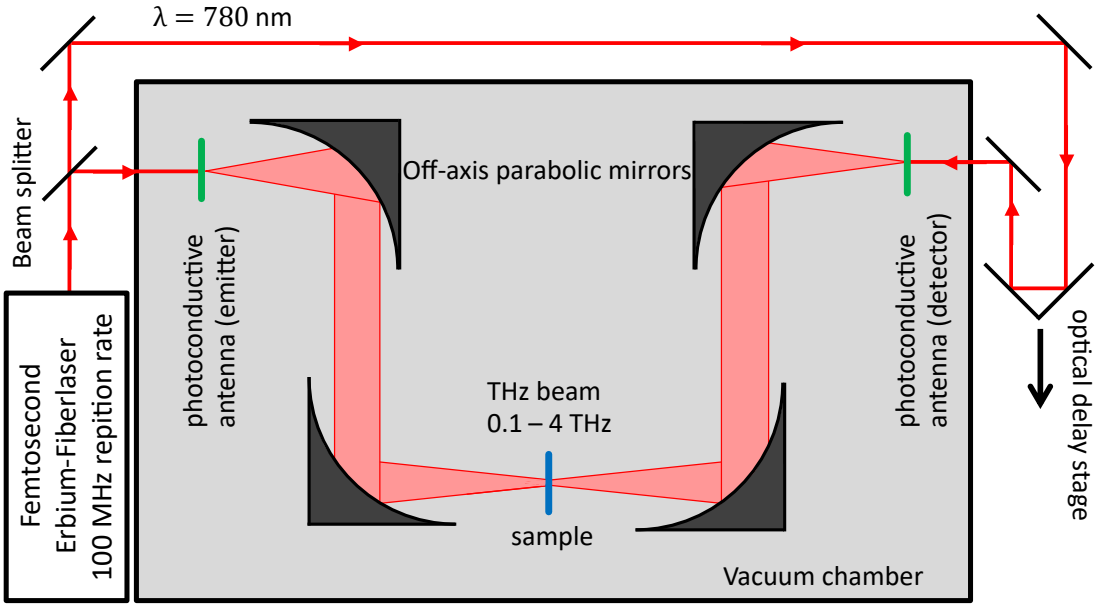

Figure 3.2: Sketch of the Terahertz time-domain spectrometer. The thin red line is the 780 nm pulsed laser. The broad beam is the THz beam. The shaded box can be evacuated or purged with nitrogen to remove the water absorption lines from the signal.

which is focussed and guided through lenses and mirrors. The semiconducting substrate of the photoconductive antenna is fabricated to have charge carriers with a short lifetime and high mobility which leads to a very short photocurrent on picosecond time scales. Changes in currents on this timescale create electromagnetic waves in the terahertz regime.

In our case the measurement antenna is the same as the emitting antenna and also works in a very similar way. Here the electric field of the terahertz beam provides the voltage between the wires of the antenna. When the laser beam hits the space between the wires, the charge carriers begin to flow and a current is measured which is directly proportional to the electric field of the THz beam. With this method it is possible to measure the electric field of the THz beam at one specific time namely at the time when the laser beam hits the measurement antenna. Using a delay stage in the optical setup we can change the time when the laser beam hits the measurement antenna. By scanning over the whole time span of the THz pulse we can measure a time resolved signal which contains amplitude and phase of the beam.
The laser used in the Time-Domain Spectrometer is an Erbium doped fiber laser with 780 nm wave length and a repetition rate of 100 MHz. Using a lock-in amplifier at this frequency drastically improves the signal-to-noise ratio of the measurement.
The frequency resolution of the measurement depends on the length of the time window of the measurement. The uncertainty principle for signal processing states $\Delta t \cdot \Delta f \geq 1$. So to increase the frequency resolution (smaller Δf) we have to increase length of the time

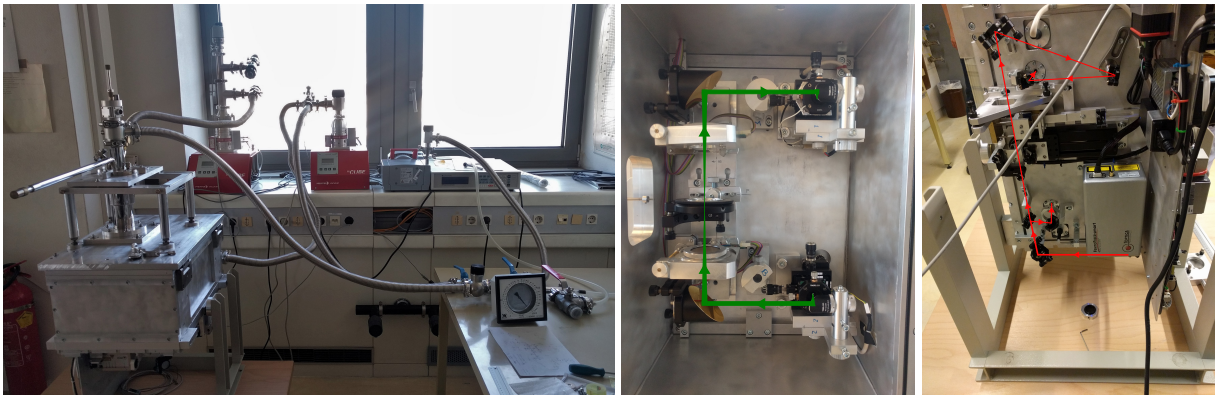

(a) (b) (c)

Figure 3.3: Pictures of the THz-TDS setup at the TU Wien. (a) shows the TDS setup with a Helium flow cryostat which is inserted into the evacuated THz chamber. The pump system contains two turbomolecular pumps, one for the insulating layer of the cryostat and one to pump the THz chamber. A rotary vane pump (not shown) is used to pump the Helium at the cryostat. (b) shows the inside of the THz chamber with the golden mirrors and two polarizers. the path of the THz beam is indicated by green lines. (c) shows the laser setup which is used to trigger the measurement. It is mounted on the bottom of the THz chamber.

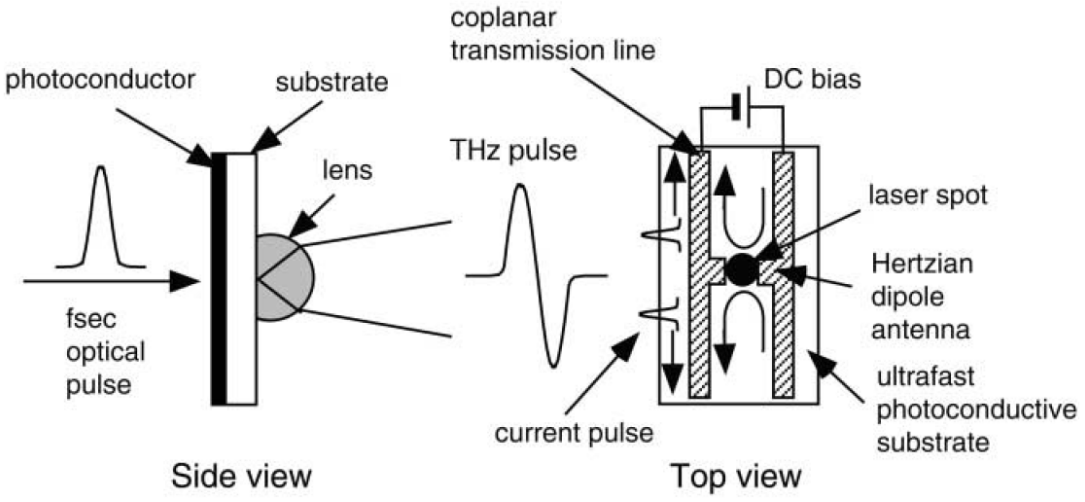

Figure 3.4: Side and top view of a photoconductive antenna used for the generation and detection of short THz-pulses. Taken from *Terahertz Optoelectronics* [37].

window. On the other hand the bandwidth of the spectrometer depends on the density of data points in the time domain.

3.1.1 Data analysis

The measured electric field can be transformed to frequency space via Fourier Transform as shown in figure 3.1. Typically the time signal is multiplied with a Gaussian window centered around the maximum of the THz signal in order to prevent broadening and ringing of the signal in frequency space due to time truncation [38].
By comparing the measured signal to a reference signal, resonances and other features of the material can be identified and it is possible to calculate optical parameters of the sample such as the dielectric permittivity $\varepsilon(\omega)$, magnetic permeability $\mu(\omega)$ and the refractive index $N(\omega) = \sqrt{\varepsilon\mu}$. The calculation of these parameters for a single layered sample where the main pulse can clearly be distinguished from the later reflections is described in the following section, which follows the calculations of Ref. [39]. The signal evaluation for samples on a substrate is discussed in Ref. [38].

When the electromagnetic wave transmits through the sample, a fraction of the wave is reflected and another part is transmitted at each interface layer. The complex transmission and reflection amplitude coefficients t_{01} and r_{01} at the interface of a medium with refractive index N_0 and a medium with N_1 for a normal incidence of light are described by

$$t_{01} = 2\frac{N_0}{N_0 + N_1} \quad \text{and} \tag{3.1}$$

$$r_{01} = \frac{N_0 - N_1}{N_0 + N_1}\,. \tag{3.2}$$

The absorption and phase shift of an electromagnetic wave inside a material with the frequency dependent refractive index N is described with

$$\exp(-\mathrm{i}N\frac{\omega d}{c})\,, \tag{3.3}$$

where $\omega = 2\pi f$ is the angular frequency of the light, d is the thickness of the material and c is the speed of light in vacuum.
Using equations (3.1-3.3) it is possible to describe the change of the electric field E of the electromagnetic wave, when transmitted through a sample, which is sketched in figure 3.5. At each interface of the material a fraction of the wave is reflected, which leads to additional but delayed light pulses at the detector. In many spectrometers, this Fabry-Pérot effect is part of the measured signal. Due to the time resolution of a THz-TDS, we can choose to separate the directly transmitted wave, also referred to as the main pulse, from the Fabry-Pérot interferences that arrive later at the detector. This only works, if the first pulse of the signal can clearly be distinguished from the later ones which requires a large enough optical path length within the sample Nd. The electric field of the measured main pulse E can then be described by

$$E = E_0 t_{01} t_{10} \exp(-\mathrm{i}N\frac{\omega d}{c}) \tag{3.4}$$

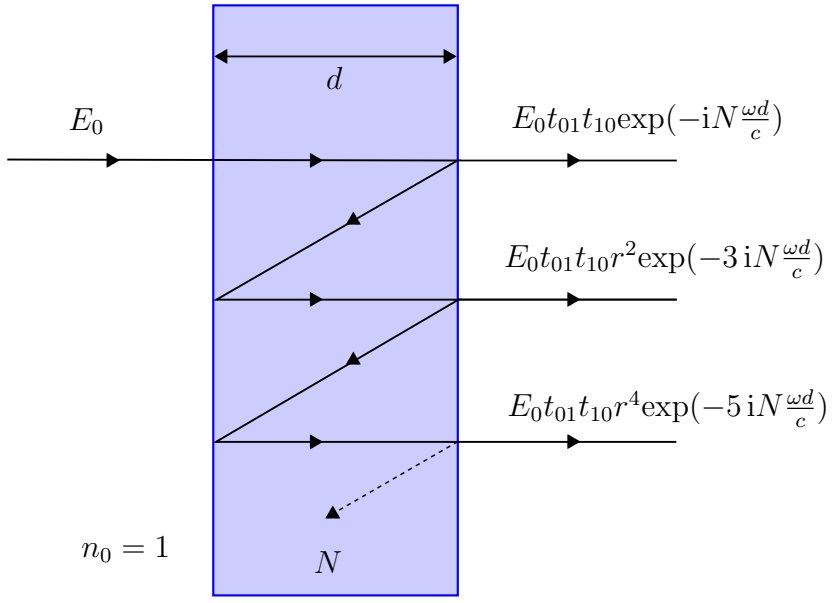

Figure 3.5: Transmission of an electromagnetic wave through a material with refractive index N and thickness d. At each interface a part of the wave is transmitted and a part is reflected which is described with t and r respectively. The electric field of the incident wave is described with E_0.

where E_0 is the incident electric field of the signal, and

$$t_{01} = 2\frac{n_0}{n_0 + N} \tag{3.5}$$

$$t_{10} = 2\frac{N}{n_0 + N} \tag{3.6}$$

are the amplitude transmission coefficients for the transition from vacuum to the sample and back to the vacuum. Here $n_0 = 1$ is the refractive index of vaccum and $N = n_\mathrm{S} - \mathrm{i}\kappa$ is the complex refractive index of the sample.
In order to calculate the transmission, a reference measurement without a sample is performed. This reference beam can be described with

$$E_\mathrm{ref} = E_0 \exp(-\mathrm{i}n_0\omega d/c)\,. \tag{3.7}$$

The transmission through the material is then given by

$$T(\omega) = \frac{E(\omega)}{E_\mathrm{ref}(\omega)} = t_{01}t_{10}\exp\left(-\mathrm{i}N\frac{\omega d}{c}\right)\exp\left(\mathrm{i}n_0\frac{\omega d}{c}\right) \tag{3.8}$$

$$= \frac{2n_0}{n_0 + N}\frac{2N}{N + n_0}\exp\left(-\mathrm{i}N\frac{\omega d}{c}\right)\exp\left(\mathrm{i}n_0\frac{\omega d}{c}\right) \tag{3.9}$$

$$\overset{n_0=1}{=} \frac{4N}{(N+1)^2}\exp\left(-\kappa\frac{\omega d}{c}\right)\exp\left(-\mathrm{i}\frac{(n_\mathrm{S}-1)\omega d}{c}\right) \tag{3.10}$$

where $E(\omega)$ and $E_{\mathrm{ref}}(\omega)$ are measured experimentally. This expression can often be simplified for weak absorptions $\kappa \ll 1$ to

$$T(\omega) = \underbrace{\frac{4n_{\mathrm{S}}}{(n_{\mathrm{S}}+1)^2}\exp\left(-\kappa\frac{\omega d}{c}\right)}_{\text{amplitude}} \exp\Bigg(-\mathrm{i}\underbrace{\frac{(n_{\mathrm{S}}-1)\omega d}{c}}_{\text{phase}}\Bigg). \tag{3.11}$$

The amplitude and phase of the transmission can easily be separated in this case and are used to calculate the refractive index of the material

$$n_{\mathrm{S}}(\omega) = -\frac{c}{\omega d}\arg(T(\omega)) + 1\,, \text{ and} \tag{3.12}$$

$$\kappa(\omega) = \frac{c}{\omega d}\ln\left(\frac{4n_{\mathrm{S}}(\omega)}{(n_{\mathrm{S}}(\omega)+1)^2|T(\omega)|}\right). \tag{3.13}$$

If the assumption of weak absorption doesn't apply, this procedure can still be used to find starting values for n_{S} and κ which can be optimized by fitting the theoretically calculated transmission (eq. (3.10)) to the experimentally obtained values.

3.1.2 Ringing time trace of the transmitted signal

The shape of the time trace changes when it is transmitted through a material. The shape of the first pulse is altered due to the (frequency-dependent) absorption in the sample. However, the time trace after the first pulse is not flat as in a reference measurement but also shows some oscillations. As an example the TDS measurement of a $SmFe_3(BO_3)_4$ single crystal is shown in figure 3.6. At 50 K this material doesn't show any resonances, at 2.8 K four resonances are observed in the measured frequency range. The origin of the resonances is not relevant in this case. When looking at the time trace after the main pulse (32 ps to 55 ps), a clear difference between the two measurements can be seen as shown in figure 3.6c. The time trace of the 50 K measurement (red) is nearly flat between the two main pulses while the 2.8 K measurement (blue) shows some oscillations. Performing a Fourier Transform of this time window reveals that the signal at 2.8 K mostly consists of the resonance frequencies of $SmFe_3(BO_3)_4$ as the peaks match the resonance frequencies of the main signal shown in figure 3.6b. The interpretation of the origin of this signal is a widely debated topic.

One possible interpretation is that after the absorption of light, the material emits the light again after a short period of time which can be observed as a free induction decay signal [40,41]. However, such an effect could only be observed for a strong direction-dependent radiation in the direction of the measurement antenna and would therefore be very hard to detect. Further, this effect is not unique to time-resolved measurements as it is also observed in measurements with a Fourier Transform infrared spectrometer based on the Michelson interferometer [42].

This makes it very likely that this signal originates from missing Fourier components in the measurement: The incident light consists of many frequencies and some of them are absorbed by the sample. Due to this absorption, the transmitted wave consists of all

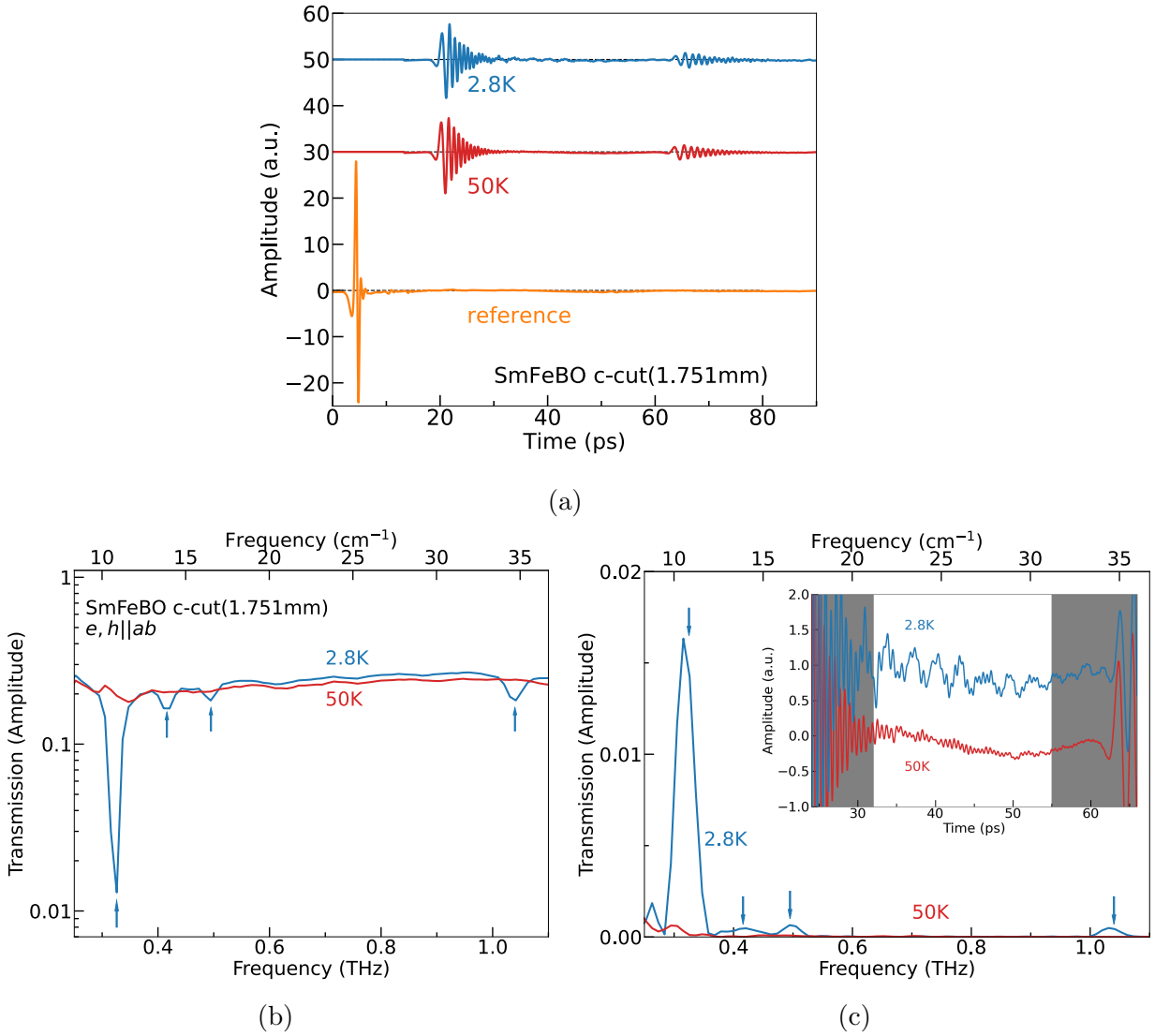

Figure 3.6: Comparison of the TDS main pulse and the "ringing" of the signal. As an example, a zero-field measurement of $SmFe_3(BO_3)_4$ c-cut at 50 K and 2.8 K is shown ($e \parallel ab$, $h \parallel ab$). (a) Time trace of the THz TDS measurement. The first pulse and the first Fabry-Pérot reflection can be seen. (b) Transmission spectra calculated from the Fourier Transform of the main peak of the time trace. The blue curve shows four excitations which are indicated by blue arrows. (c) Analysis of the time trace between the main peak and the first Fabry-Pérot reflection of the THz TDS measurement. The inset shows the time-trace of the two measurements. "Transmission" is the Fourier transform of this time trace from 32 ps to 55 ps divided by the Foruier transform of the reference measurement. The blue arrows are at the same positions as in (b) which show the energies of the excitations in the material.

frequencies except the resonance frequencies. These frequencies are also missing in the previously flat signal after the main pulse. When these frequencies are removed from a previously flat signal, the line shows oscillations at exactly these frequencies which are also seen in the absolute of the Fourier transform. So the Fourier Transform of such a ringing shows some features at exactly the resonance frequencies because the respective Fourier components are missing.

In order to further understand this effect, a simple model can be made. For the model, a reference measurement (see figure 3.7a) is taken and a Fourier Transform is performed (Fig. 3.7a, blue line). Using this reference Fourier transform E_0, we can calculate the signal of an artificial sample with a single resonance at 0.32 THz. This is done with the Lorentz oscillator model [43] where the permittivity of a sample with such a resonance can be described by

$$\varepsilon(\omega) = 1 + \frac{\Delta\varepsilon\omega_0^2}{\omega_0^2 - \omega^2 - \mathrm{i}\gamma\omega} \tag{3.14}$$

with the permittivity contribution $\Delta\varepsilon$, resonance frequency ω_0 and linewidth γ. For this example the parameters are chosen to be $\Delta\varepsilon = 0.02$, $\omega_0 = 0.32\,\mathrm{THz}$ and $\gamma = 0.04\,\mathrm{THz}$.

Using equation 3.4 and $n = \sqrt{\varepsilon}$, the signal E of such a resonance can then be calculated (figure 3.7b, orange line) and is then transformed back to time space using an inverse Fourier transform. This time trace which consists of the reference measurement and the 0.32 THz resonance is shown in figure 3.7c. In the time trace the ringing of the signal after the main peak is clearly visible. This ringing can now be analyzed with a Fourier Transform of the time window from 8 ps to 30 ps which is shown in figure 3.7d. As the Foruier transform of the ringing shows, this signal is mostly made up of a 0.32 THz component which appears because this Fourier component is missing due to the absorption at a resonance.

3.2 Fourier-Transform Infrared Spectrometer

A Fourier-Transform Infrared Spectrometer (FTIR) works in a similar way as a Michelson interferometer but it has a broadband light source. A light beam is split by a beamsplitter into two beams of equal intensity. One beam is reflected by a fixed mirror, the other one by a movable mirror. The movable mirror is moved back and forth to change the path difference between the two beams. The beams are recombined again at the beamsplitter and the inference spectrum is guided through the sample and then measured with a Bolometer. A sketch of this interferometer is shown in figure 3.8. This yields an intensity measurement with respect to the position of the movable mirror with a maximum at the position where both mirrors have the same distance to the beamsplitter (see Fig. 3.9a). This interferogram can then be transformed to a frequency spectrum doing a Fourier Transform as shown in figure 3.9.

For a monochromatic source with frequency ν (in wave numbers) and a path difference of the mirror x without sample, the measured intensity at the detector I_{det} is given by

$$I_{\mathrm{det}}(x,\nu) = \frac{1}{2} I_{\mathrm{source}}[1 + \cos(2\pi\nu x)]\,., \tag{3.15}$$

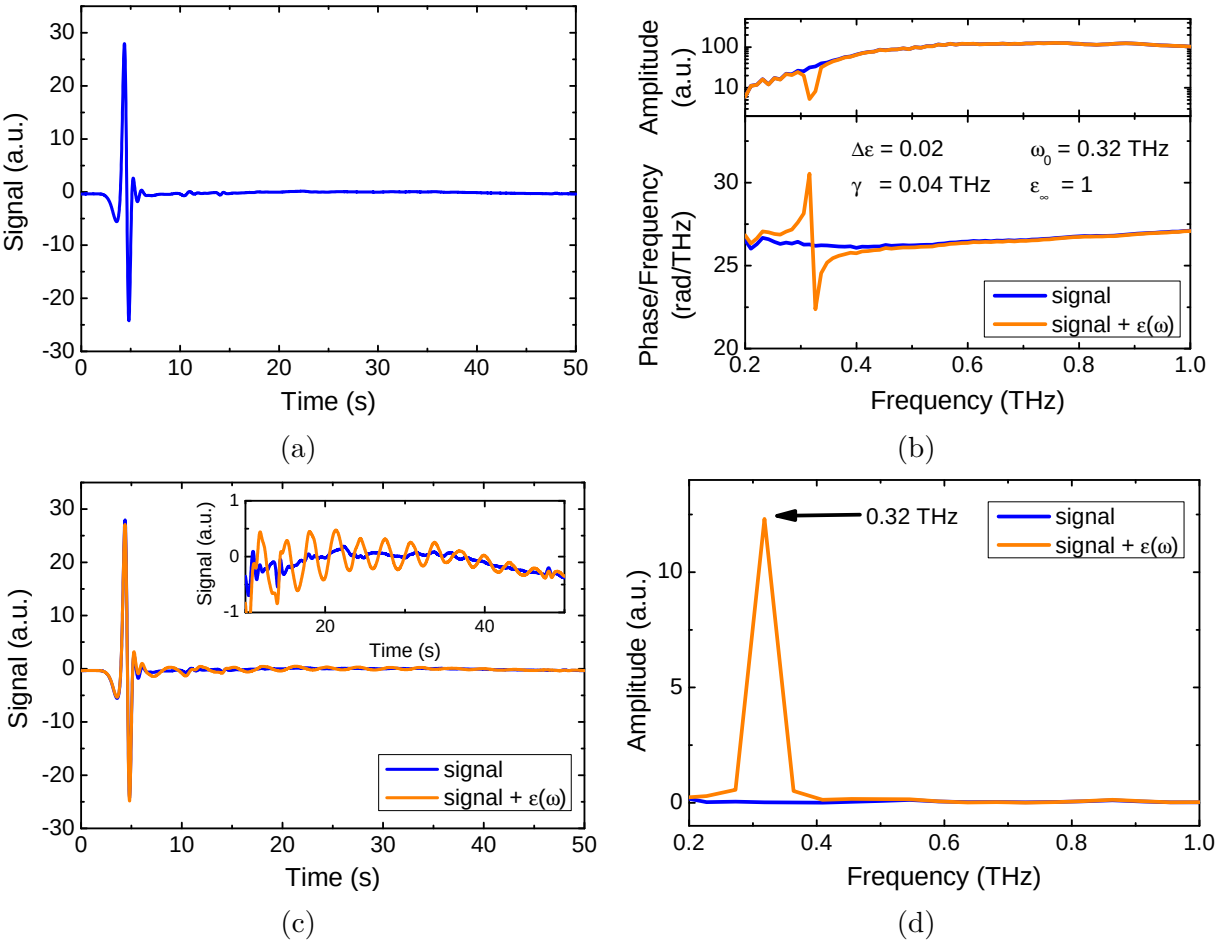

Figure 3.7: Simulation of the ringing after the main pulse in THz-TDS measurement. (a) shows the measured time trace of the empty spectrometer. (b) shows the Fourier transform of the measured signal (blue) and the Fourier transform of a simulated sample with a 0.32 THz resonance (orange). (c) shows the measured time trace of the empty spectrometer (a) and the inverse Fourier transform of the simulated sample of (b). The inset of (c) shows the time trace from 10 ps to 50 ps in more detail. (d) is the Fourier transform of the time trace shown in (c) from 8 ps to 30 ps.

where I_{source} is the intensity of the incident beam of the light source [44]. This function is maximal for $x = 0$ (zero path difference) and where the argument of the cosine is an integer multiple of 2π (constructive interference). The factor 1/2 is for the beamsplitter which in the ideal case transmits and reflects half of the incident light. When the two light beams interfere, half of the light intensity is directed back to the source. In reality a beamsplitter has unwanted absorption, and there are additional losses by the mirrors and the sample. These effects can be frequency dependent so the pre-factor in equation 3.15 is replaced by $K(\nu)$. The relevant information of the spectrum lies in the dynamics of the

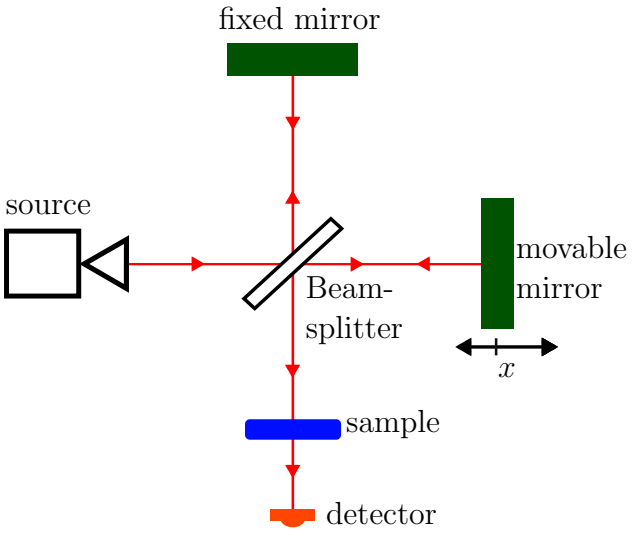

Figure 3.8: Sketch of a Michelson-Interferometer as basic element of a Fourier Transform Spectrometer.

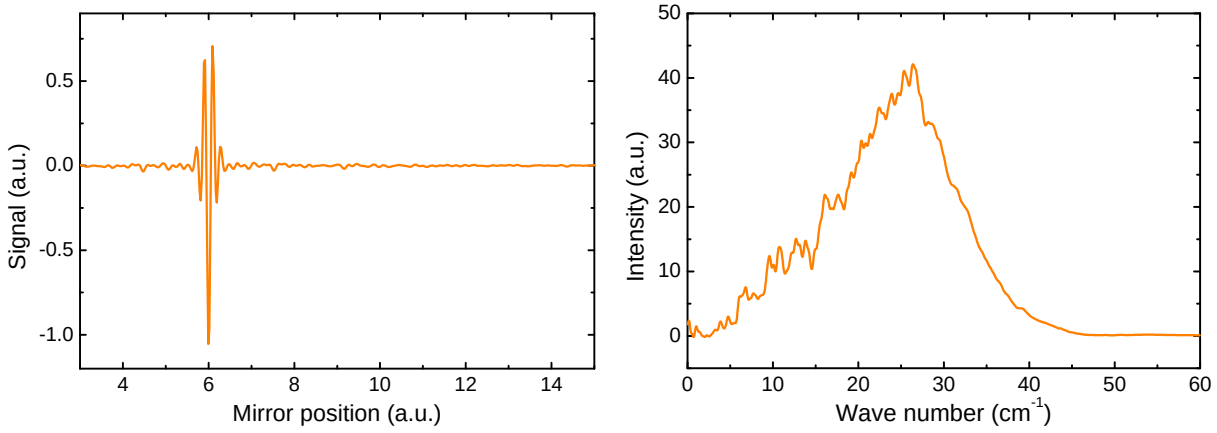

(a) (b)

Figure 3.9: Transmission intensity signal of a sample measured with a Fourier Transform spectrometer (a) and its Fourier Transform (b).

spectrometer so only the second term of equation 3.15 is considered. The relevant signal at the detector $S(x,\nu)$ then becomes

$$S(x,\nu) = K(\nu)\cos(2\pi\nu x)\,. \tag{3.16}$$

For a broadband light source this term is given by

$$S(x) = \int_0^\infty K(\nu)\cos(2\pi\nu x)\mathrm{d}\nu\,. \tag{3.17}$$

The frequency intensity spectrum $K(\nu)$ which contains all the information about the sample is then calculated with the inverse Fourier Transform

$$K(\nu) = \int_{-\infty}^{\infty} S(x)\cos(2\pi\nu x)\mathrm{d}x\,. \tag{3.18}$$

In reality it is not possible to move the mirror infinitely far away. The limits of integration become plus and minus the maximum mirror position $x_{\max}$. As the light travels to the mirror and back, the maximum optical path difference is $2x_{\max}$ which is inversely proportional to the frequency resolution $\Delta\nu = 1/2x_{\max}$.

Similar to the THz Time-Domain Spectrometer (TDS), the signal in the FTIR is measured in the length-space x and then transformed to the frequency space ν using a Fourier Transform. The frequency resolution of the spectrometer is increased by increasing the optical path difference $x_{\max}$ between the two beams. The bandwidth of the spectrometer depends on the density of data points Δx. The spectral range of a FTIR is approx. $4 - 14000\,\mathrm{cm}^{-1}$ [45].

In contrast to the TDS, it is only possible to get the amplitude of the signal with the FTIR. In order to get information about the phase of the the signal to calculate ε, a Kramers Kronig transformation is performed [46,47]. Due to the causality of complex response functions, the real and imaginary part of such a function can be connected using linear response theory. For this procedure, additional information and assumptions about the sample are necessary.

The FTIR measurements of up to 32 T shown in this thesis were performed at the High Field Magnet Laboratory of the Radboud University Nijmegen, Netherlands and the National Institute of Chemical Physics and Biophysics in Tallin, Estonia.

3.3 Physical Property Measurement System

A Physical Property Measurement System (PPMS) is used to measure electric, magnetic and thermal properties of a sample. It consists of a large superconducting magnet in which the sample can be cooled down to Helium temperatures (2-350 K). With the PPMS at the TU Vienna, magnetic fields of up to 14 T can be applied. Different measurement devices can then be connected to the sample in order to measure its physical properties in these conditions.
In this thesis capacitive measurements and charge measurements are performed to measure the dielectric permittivity $\varepsilon(\omega)$ and electric polarization P, respectively.

3.3.1 Electric polarization measurements

To measure the electric polarization P of the sample, it is connected to a Keithley electrometer using silver paste and a voltage of approx. 150 V is applied. The electrometer

measures tiny currents in the sample which are integrated over time in order to get the charge displacement Q along the sample. The polarization can then be calculated using $P = Q/A$, where A is the area of the contact. With this method, changes in the polarization due to temperature change or magnetic field sweep can be observed. In many cases, the polarization in the high-temperature non-magnetic phase can be considered zero, thus can be used as reference to obtain the absolute value of the polarization.

3.3.2 Dielectric Permittivity

The dielectric permittivity $\varepsilon(\omega)$ is measured using an "Alpha-A High Resolution Dielectric, Conductivity, Impedance and Gain Phase Modular Measurement System". A voltage $U(t)$ with $U_{\mathrm{RMS}} = 1\,\mathrm{V}$ and frequency $f = 2\pi\omega$ is applied to the sample capacitor which causes a current $I(t)$ at the same frequency. From the amplitude and phase shift of the current the impedance Z and capacity C can be calculated which is then used to calculate the dielectric permittivity

$$\varepsilon(\omega) = \varepsilon_1(\omega) + \mathrm{i}\varepsilon_2(\omega) = \frac{Cd}{\varepsilon_0 A} \tag{3.19}$$

and the conductivity

$$\sigma(\omega) = \sigma_1(\omega) + \mathrm{i}\sigma_2(\omega) = -\mathrm{i}\omega\varepsilon_0\varepsilon(\omega) \tag{3.20}$$

of the sample. Here A and d are the area of the contact and thickness of the sample respectively, and ε_0 is the vacuum permittivity. These formulas only work for the ideal infinite plate capacitor geometry, otherwise corrections for stray electric fields have to be considered.

4. Magnetoelectric crankshaft-like switching in $GdMn_2O_5$

In this chapter, an unusual magnetoelectric switching behavior in multiferroic $GdMn_2O_5$ is investigated. First, the properties of rare-earth manganites (section 4.1) and Gd manganite (section 4.2) are introduced, followed by the description of the polarization measurements (section 4.3). Section 4.4 covers the magneto-electric switching behavior, where the application and subsequent removal of a magnetic field reverses the electric polarization of the material and appears together with an unusual 4-state hysteresis cycle. These results were published in an article in Nature [13]. The follow-up measurements which contain the full control of the previously measured polarization hysteresis cycle are discussed in section 4.5 (manuscript in preparation).

4.1 Rare-earth manganites $R\mathbf{Mn_2O_5}$

The crystal structure of $R\mathrm{Mn_2O_5}$ is orthorhombic and belongs to the *Pbam* space-group at room-temperature [48,49]. The interaction of the $3d$ magnetic moments of Mn^{3+} and Mn^{4+} ions with the $4f$ magnetic moments of R^{3+} ions lead to complex and competing magnetic interactions. This makes the system highly frustrated and gives rise to complicated phase diagrams with various magnetically ordered phases [11,50–52].
The influence of an applied magnetic field on the electric polarization in the low-temperature magnetically ordered phases of $R\mathrm{Mn_2O_5}$ has been investigated in various cases: Electric polarization can be induced by an external magnetic field in $HoMn_2O_5$ [53] and $DyMn_2O_5$ [15,50,54], can be suppressed in $ErMn_2O_5$ [53], enhanced in $NdMn_2O_5$ [55], reversed in $TbMn_2O_5$ [14] and $GdMn_2O_5$ [12,13] or rotated in $TmMn_2O_5$ [56] and $YbMn_2O_5$ [57]. The dielectric response depends strongly on on the type and size of the rare-earth ion [55,58,59] and the direction of the applied magnetic field [12].

4.2 Properties of $GdMn_2O_5$

The magnetic structure of $GdMn_2O_5$ differs slightly from other RMn_2O_5: Below $T_{N1} \approx 40\,K$ $GdMn_2O_5$ orders in an incommensurate phase with a wave vector $\mathbf{q} = (0.486,0,0.18)$ followed by a commensurate state with $\mathbf{q} = (1/2,0,0)$ below $T_{N2} = 33\,K$. This state shows a huge magnetically induced electric polarization of $3600\,\mu Cm^{-2}$ with variations of up to $5000\,\mu Cm^{-2}$ in an external magnetic field [12]. The electric polarization is induced by symmetric exchange striction mechanisms on the Mn-Mn and Mn-Gd bonds [12] and has a large electronic component [60].
As in other RMn_2O_5, the crystal structure of $GdMn_2O_5$ is orthorhombic and belongs to the *Pbam* space-group at room-temperature [48,49]. Mn^{4+} and Mn^{3+} ions are ordered in zig zag chains along the $a-$axis alternating between $Mn^{4+}O_6$ octahedra and $Mn^{3+}O_5$ pyramids with AFM intrachain exchange interactions between neighboring spins. The Mn ions of neighboring chains form AFM pentagons with a Gd ion in the middle leading to relatively weak and geometrically frustrated interchain exchange interactions [61–63]. A picture of the lattice is shown in figure 4.1.

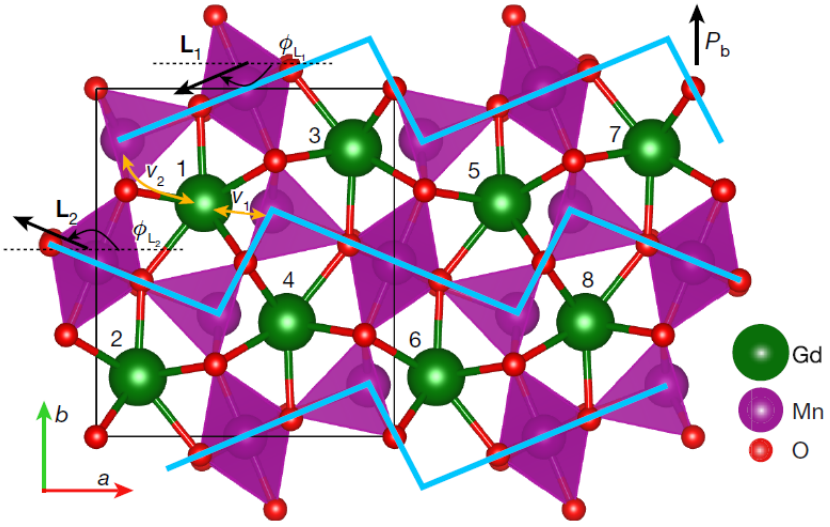

Figure 4.1: Magnetic unit cell of $GdMn_2O_5$. The structural unit cell is shown by the black box. Mn ions are shown as purple spheres. The zig zag chains with intrachain AFM interaction between Mn ions are shown by cyan lines. The Néel vectors $\mathbf{L}_1$ an $\mathbf{L}_2$ for the two distinct chains have the angles ϕ_{L_1} and ϕ_{L_2} with the a-axis. The Mn ions of two chains form pentagons with Gd ions (green spheres) inside. Superexchange interactions are mediated by O ions (red spheres) [13]. The exchange paths between Gd ions and the Mn chains are shown as yellow arrows with the Heisenberg exchange constants ν_1 and ν_2. Graphic taken from Ref. [13].

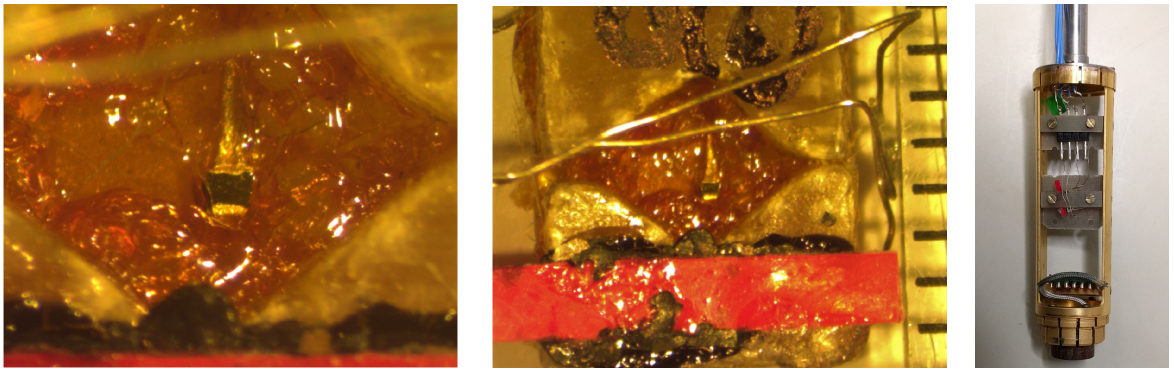

(a) (b) (c)

Figure 4.2: Pictures of the $GdMn_2O_5$ crystal (0.4 x 0.4 x 0.4 mm^3) embedded in GE Varnish (a and b). The red stripe is used to align the applied magnetic field along the a-axis. (c) shows the sample on the measurement rod.

4.3 Sample and experimental setup

The $GdMn_2O_5$ sample that was used for the measurements in this thesis and in Ref. [13] is a single crystal of approx. 0.4 x 0.4 x 0.4 mm^3 with electric contacts on the b-plane in order to apply electric fields and measure electric polarization along the b-axis. The sample is embedded in GE-Varnish as shown in figure 4.2. The red stripe that can be seen in the pictures is used to align the applied magnetic field along the a-axis.

The electric polarization is measured using a Physical Property Measurement System (PPMS) with temperatures down to 2 K and magnetic fields of up to 12 T. The procedure of such a measurement is explained in section 3.3.

4.4 Magnetoelectric crankshaft

4.4.1 Experimental observation

Polarization experiments of our $GdMn_2O_5$ sample were performed at approx. 2 K. At this temperature, the $GdMn_2O_5$ sample shows a huge electric polarization along the b-axis. When applying a magnetic field along the a-axis of $GdMn_2O_5$, the electric polarization P_b is reversed at around 5 T at low temperatures (see figure 4.3a). Reducing the external field again leads to a polarization reversal to positive polarization, so that at 0 T the initial polarization is restored. This process is reversible over multiple field sweeps showing a hysteresis at around 5 T [11,12].

Due to the complex magnetic structure of GdMn2O5, the system is very sensitive to the exact orientation of the external magnetic field [11]. This leads to interesting results when the applied magnetic field is tilted away from the a-axis in the a-b-plane. For temperatures below 5 K the hysteresis loop changes drastically depending on the magnetic field angle.

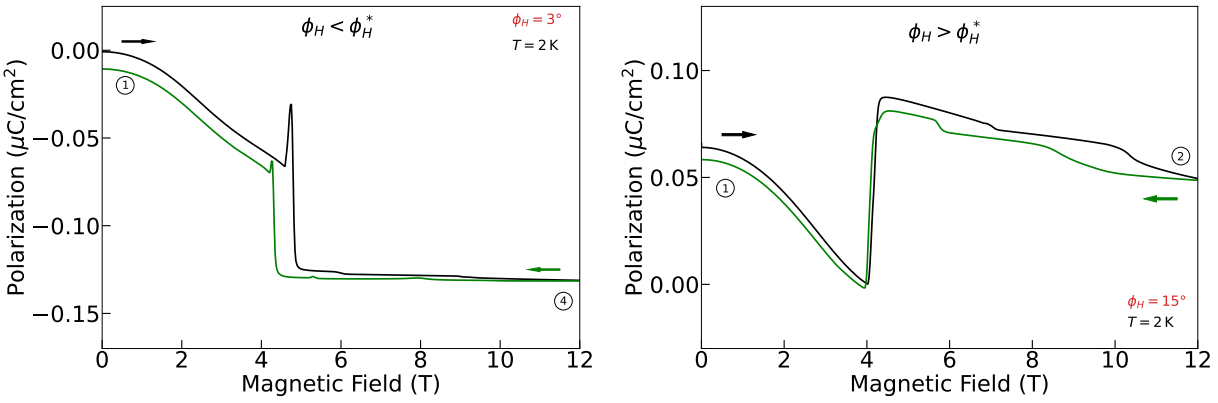

(a) $\phi_H < \phi_H^*$ (b) $\phi_H > \phi_H^*$

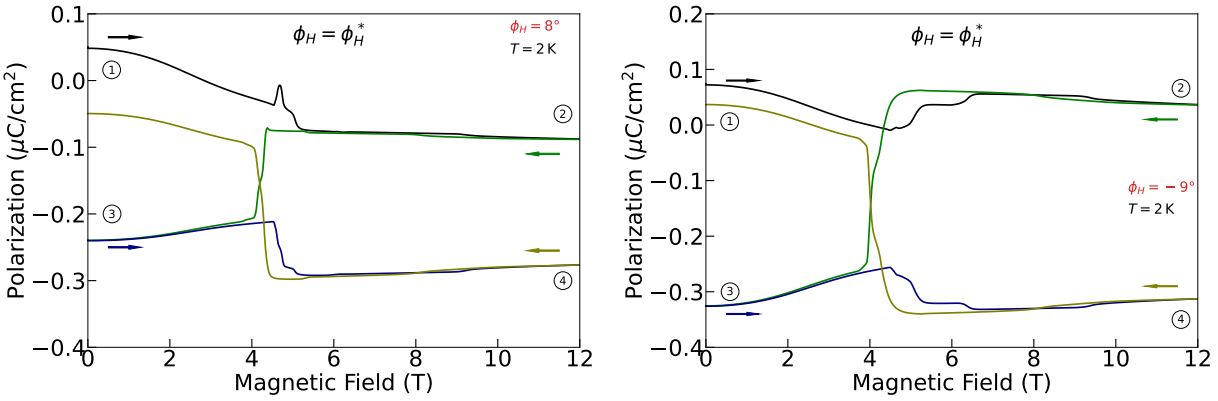

(c) $\phi_H = \phi_H^*$ (d) $\phi_H = \phi_H^*$

Figure 4.3: Electric polarization P_b of $GdMn_2O_5$ for different off-axis orientations of the applied magnetic field. For magnetic field angles close to the a-axis, the polarization is reversed upon changing the applied field and shows a hysteresis around 4.5 T (a). For magnetic field angles larger than 11° the polarization shows some features around 4.5 T but stays positive. An unusual four-state hysteresis loop is observed for magnetic field angles close to the magic angle $\phi_H^* \approx \pm 9°$ (c) and (d). The four polarization states are marked with 1-4. The direction of the magnetic field sweep is shown by arrows. The measurements were performed at 2 K. The polarization values have an arbitrary offset due to a drift in the measurement device.

For angles larger than 11°, no polarization reversal is observed. The polarization P_b stays positive at all fields but still shows a small hysteresis and some interesting features around 5 T (fig. 4.3b). So there might exist a border region between 0° and 11°, where some mixing of the two observed effects happens. This is the case for a small region around $\phi_H = \phi_H^* \approx \pm 9°$, the so-called "magic" angle region.
At this magic angle, an unusual hysteresis loop opens up which is characterized by a

four-state cycle with polarization reversals at every second field sweep (Figs. 4.3c and 4.3d). Increasing the magnetic field from the initial positive polarization at zero-field (state 1), doesn't lead to a polarization reversal. The electric polarization stays positive the whole time to a state with positive polarization at high field (state 2), as it was the case for $\phi_H > \phi_H^*$. When reducing the magnetic field again, the electric polarization is reversed at around 5 T reaching a state with negative polarization at zero-field (state 3). At the subsequent increase of magnetic field, the polarization remains negative which leads to a high-field state with negative polarization (state 4). During the next decrease of the field, the polarization is reversed again leading to a positive polarization at zero-field (state 1), the initial state of the experiment.
To summarize this, increasing the magnetic field (state 1 $\rightarrow$ state 2, state 3 $\rightarrow$ state 4) doesn't reverse the polarization while decreasing the applied field (state 2 $\rightarrow$ state 3, state 4 $\rightarrow$ state 1) results in a reversal of electric polarization. So in total two full up and down magnetic field sweeps are needed in order to get back to the initial state. This four-state loop is stable over multiple field sweeps.

4.4.2 Theoretical model

In order to understand this puzzling behavior, a classical spin model can be derived to simulate the electric and magnetic behavior during this process. The model described in this thesis gives an overview over the model discussed in our publication in Ref. [13] developed by L. Ponet, S. Artyukhin and M. Mostovoy.
The $GdMn_2O_5$ system can be described through two interacting Mn chains (cyan lines in Fig. 4.1) and eight Gd ions per unit cell that are coupled to an external electric and magnetic field. Neighboring Mn spins within each chain are assumed to be mostly anti-parallel even in magnetic fields due to the strong AFM intrachain exchange interaction in RMn_2O_5 systems [63]. So the two chains of Mn spins can be described with the two Néel vectors $\mathbf{L}_\alpha$ ($\alpha = 1,2$) which interact with the spins of the 8 Gd ions $\mathbf{S}_i$ ($i = 1,...,8$) (see Fig. 4.1). Through the Heisenberg exchange striction, an electric polarization along the b-axis is induced that is proportional to $\mathbf{L}_1 \cdot \mathbf{L}_2$ in addition to a similar contribution originating from the Gd-Mn bonds.

The energy per magnetic unit cell can then be described with the Hamiltonian

$$\begin{aligned}\mathcal{H} = &\gamma(\mathbf{L}_1 \cdot \mathbf{L}_2)^2 + \sum_\alpha \chi((\mathbf{H} \cdot \mathbf{L}_\alpha)^2 - H^2) \\ &- K_\mathrm{L} \sum_\alpha (\mathbf{L}_\alpha \cdot \mathbf{n}_\alpha)^2 - \sum_i (K_\mathrm{S}(\mathbf{N}_i \cdot \mathbf{S}_i)^2 + g\mu_\mathrm{B}\mathbf{H} \cdot \mathbf{S}_i) \\ &+ \frac{1}{2}(g\mu_\mathrm{B})^2 \sum_{i \neq j} \left(\frac{\mathbf{S}_i \cdot \mathbf{S}_j}{r_{ij}^3} - 3\frac{(\mathbf{S}_i \cdot \mathbf{r}_{ij})(\mathbf{S}_j \cdot \mathbf{r}_{ij})}{r_{ij}^5} \right) \\ &+ \sum_{i,\alpha} V_{i\alpha} \mathbf{S}_i \cdot \mathbf{L}_\alpha \\ &- P_b[8\beta_1(\mathbf{L}_1 \cdot \mathbf{L}_2) + (\mathbf{S}_1 - \mathbf{S}_5)(\beta_2 \mathbf{L}_2 + \beta_3 \mathbf{L}_1) \\ &+ (\mathbf{S}_2 - \mathbf{S}_6)(\beta_2 \mathbf{L}_1 + \beta_3 \mathbf{L}_2) + (\mathbf{S}_3 - \mathbf{S}_7)(\beta_2 \mathbf{L}_2 - \beta_3 \mathbf{L}_1) \\ &+ (\mathbf{S}_4 - \mathbf{S}_8)(\beta_2 \mathbf{L}_1 - \beta_3 \mathbf{L}_2)] + P_b^2/2\,.\end{aligned} \tag{4.1}$$

The first term describes the competition between the interchain exchange $J_\perp$ and the intrachain AFM exchange $J_\parallel$, where $\gamma \approx J_\perp^2/J_\parallel > 0$. It leads to a lowering of the energy when $\mathbf{L}_1$ and $\mathbf{L}_2$ are non-collinear. The second term originates from the Zeeman energy of the antiferromagnetically ordered Mn spins which are canted by the magnetic field, where χ is the magnetic susceptibility perpendicular to $\mathbf{L}$. The easy-axis anisotropy of the system is represented by the constants K_L and K_S and the unit vectors along the easy axes $\mathbf{n}_\alpha$ and $\mathbf{N}_i$ of Mn and Gd spins, respectively. The third line accounts for the dipole-dipole interactions of Gd spins, which was restricted to five nearest neighbours with the Landé factor g and the Bohr magneton μ_B. The fourth line describes the interaction between Mn and Gd ions with the Heisenberg exchange constants $V_{i\alpha} = \nu_1, \nu_2$, where ν_1 describes the coupling between the Gd ion and nearest pentahedrally coordinated Mn ion and ν_2 the coupling between the Gd ion and the other Mn chain (see figure 4.1). The last three lines describe the magnetoelectric interactions between the electric polarization P_b and $\mathbf{L}_\alpha$ and $\mathbf{S}_i$ with the exchange striction parameters $\beta_{1,2,3}$, followed by the dielectric energy $P_b^2/2$.

At zero-field the commensurate multiferroic state of $GdMn_2O_5$ is four-fold degenerate as it breaks both time-reversal symmetry and inversion symmetry. States related to time-reversal symmetry $(\mathbf{L}_1, \mathbf{L}_2) \rightarrow (-\mathbf{L}_1, -\mathbf{L}_2)$ have the same electric polarization whereas states related to inversion symmetry $(\mathbf{L}_1, \mathbf{L}_2) \rightarrow (-\mathbf{L}_1, +\mathbf{L}_2)$ have the opposite polarization.

Using the spin model, the local energy minimum can be tracked when increasing and decreasing the magnetic field. The model parameters of the simulations were chosen to reproduce the experimentally obtained data. Good results are obtained for $\gamma = 0.05\,\mathrm{meV}$, $\chi = 0.01\,\mathrm{meV}^{-1}$, $K_\mathrm{L} = 1.1\,\mathrm{meV}$, $K_\mathrm{S} = 0.09\,\mathrm{meV}$, $\nu_1 = 7.9\,\mathrm{meV}$, $\nu_2 = 0.15\,\mathrm{meV}$, $\beta_1 = 0.06\,\mu\mathrm{C\,cm^{-2}}$, $\beta_2 = 0.06\,\mu\mathrm{C/cm^2}$ and $\beta_3 = 0.04\,\mu\mathrm{C/cm^2}$. The easy-axes $\mathbf{n}_\alpha$ follow the long segments of the zigzag Mn chains shown in figure 4.1 with $\pm 23.4°$ to the a-axis, $\mathbf{N}_i$ are at $\pm 12°$ to the a-axis, which is remarkably close to the magic angle. The simulated polarization curves are shown in figure 4.4.
For magnetic field angles around $\phi_H = 10°$, a narrow but robust magic-angle region is

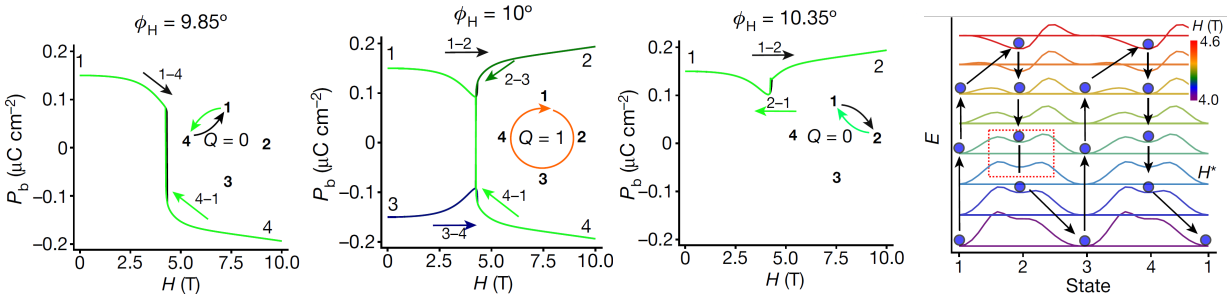

(a) (b) (c) (d)

Figure 4.4: Model for the evolution of the electric polarization during magnetic field sweeps for different field angles (a-c). The insets indicate the switching paths and and topological winding numbers. At the magic angle, the four-state switching is observed (b). (d) shows the evolution of the energy minimum between the four states at the magic angle ϕ_H^* in the hysteresis region between 4 and 5 T. The energy barriers were calculated using elastic string calculations. The blue dots show the position of the minimum and the arrows denote the its trajectory. The plots are shifted vertically to distinguish the magnetic field strengths. For illustrative purpose the model parameters where slightly changed. The pictures are taken from Ref. [13].

found in which the extremely flat energy landscape evolves asymmetrically in external magnetic fields which leads to a unidirectional spin rotation of half of the Gd spins of approx. 90° (see Fig. 4.4d).

Further, it is found that the two regions for $\phi_H < \phi_H^*$ and $\phi_H > \phi_H^*$ are topologically trivial but distinct from each other with the magic angle region being a novel topological boundary regime interpolating between these two regimes. It is possible to define a winding number Q of a path in the two-dimensional (ϕ_{L_1},ϕ_{L_1}) space with torus topology which is zero in the two-state switching regimes and becomes $Q = 1$ in the four-state switching regime. This shows that as long as there are two extremal regions in the material there exists a boundary region near the magic angle that leads to a circular four-state hysteresis. A more in-depth discussion of the model can be found in Ref. [13].

4.5 Controlled magnetoelectric switching

For the observed magnetoelectric switching to be more applicable for memory storage devices, it is desirable to lower the switching costs by controlling the switching through electric fields and by reducing the applied magnetic fields. These parameters were investigated in detail and are discussed in the following section: The influence of an external electric field during the magnetic field ramping is discussed in section 4.5.1 and the influence of the magnetic field range in section 4.5.2.

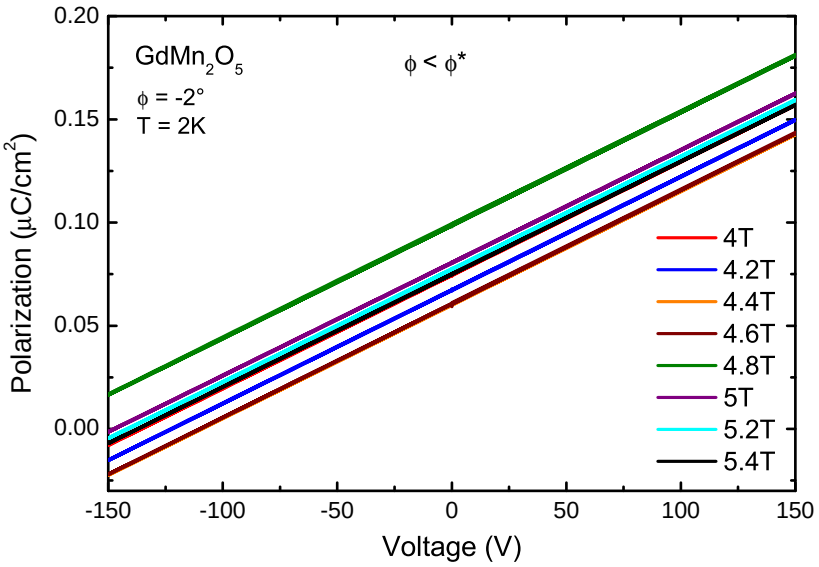

Figure 4.5: Electric field sweeps for constant magnetic fields $H_0 \parallel a$ at 2 K. The measured polarization is linear and can be explained with equation 4.2, so no E-field switching is observed. The highest voltage of 150 V corresponds to an electric field of 3750 Vcm^{-1} ($d \approx 0.4$ mm).

4.5.1 Controlling the magnetoelectric switching through electric fields

When applying an electric field along the b-axis of the crystal, a polarization

$$P_{\mathrm{b,ind}} = \varepsilon_0 \chi_{\mathrm{e}} E \tag{4.2}$$

is induced which depends on the permittivity of vacuum ε_0, the electric susceptibility $\chi_{\mathrm{e}} = 17 \pm 2$ of the material [11] and the applied electric field $E = U/d$, with the voltage U and the sample thickness $d \approx 0.4$ mm. In the absence of phase switching, a linear dependence between polarization and applied electric field is expected. In the experiment shown in figure 4.5, electric field sweeps were measured at various constant magnetic fields from $4 - 5.4$ T for $\phi_H \approx 0°$. The observed polarization response is purely linear. That means we can't achieve magnetoelectric switching in $GdMn_2O_5$ with constant magnetic field purely through electric field.
The electrically induced linear polarization $P_{\mathrm{b,ind}}$ is subtracted in the following measurements in this chapter in order to better compare the measurements with different applied electric fields.

When a constant electric field is applied during magnetic field sweeps $\phi_H < \phi_H^*$, very interesting behavior of the electric polarization can be observed. When a voltage of +150 V is applied during the field sweep, the electric polarization stays positive the whole time (see figure 4.6a, red curve). Without electric field the polarization would be reversed at this angle as shown previously in figure 4.3a. If a voltage of −150 V is applied during the field

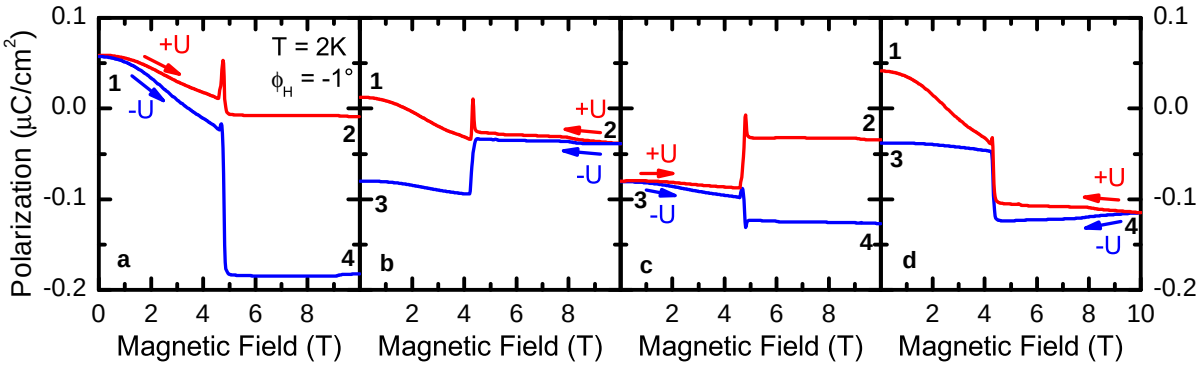

Figure 4.6: Magnetoelectric switching with an applied constant positive or negative electric field during the magnetic field sweep. Depending on the direction of the electric field, the resulting polarization can be controlled. The measurements were performed at 2 K with the magnetic field angle $\phi_H = -1°$. The constant electric field applied during the sweeps is $E_b = \pm 150\,\mathrm{V}/0.4\,\mathrm{mm} = \pm 3750\,\mathrm{V/cm}$. The direction of the magnetic field sweep is indicated by arrows. The induced electric polarization $P_{\mathrm{b,ind}} = \varepsilon_0 \chi E$ is subtracted from the data. Without electric field the polarization would switch between states 1 and 4.

sweep, the polarization is reversed leading to a negative polarization at high field (state 4, figure 4.6a, blue curve). As mentioned before, the induced electric polarization $P_{\mathrm{b,ind}}$ (equation 4.2) is subtracted from the data, as it just vertically shifts the whole dataset by a constant value. The result in figure 4.6a shows that depending on the direction of electric field during the magnetic field sweep, it is possible to control the polarization switching of the sample. If a positive electric field is applied, the polarization is positive after the field sweep, if the electric field is negative, the polarization also gets negative. The same effect happens when the magnetic field is reduced to zero: Depending on the direction of electric field during the field-sweep, the polarization is positive or negative at zero-field (see figure 4.6b, d). All the possible switchings are shown in figure 4.6.

This effect enables the control over the direction of electric polarization each time the magnetic field is changed. By chaining together different electric field-sequences it is for example possible to recreate the four-state switching that was observed previously at the magic field angle (shown in figure 4.7). It is even possible to reverse the direction of the four-state switching .

Due to the frustrated ground state with competing magnetic orders, the phase diagram of $GdMn_2O_5$ is quite complicated [11,13]. The additional contribution of the electric field to the energy balance of the system seems to be sufficient to switch to a different magnetolectric regime when magnetic field is ramped. This seems to be especially relevant for magnetic tilting angles smaller than the “magic” angle of approx. 9°.

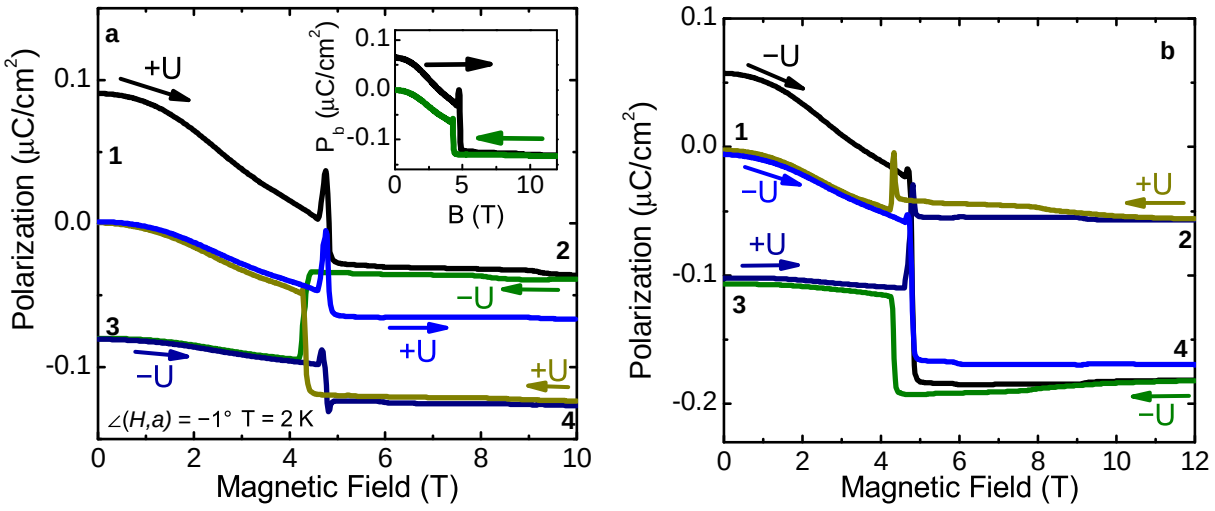

(a) $1 \to 2 \to 3 \to 4$ (b) $1 \to 4 \to 3 \to 2$

Figure 4.7: Controlled magnetoelectric switching between the four polarization states for magnetic field angles close to the a-axis. Applying an electric field sequence (black, green, dark blue, dark yellow, blue) along the b-axis during a magnetic field sweep enables the controlled four-state switching $1 \to 2 \to 3 \to 4$ (a) and $1 \to 4 \to 3 \to 2$ (b). The constant electric field applied during the sweeps is $E_b = \pm 150\,\mathrm{V}/0.4\,\mathrm{mm} = \pm 3750\,\mathrm{V/cm}$. The measurements were performed at 2 K with $\phi_H = -2°$. The direction of the magnetic field sweep is indicated by arrows. The induced electric polarization $P_{\mathrm{b,ind}} = \varepsilon_0 \chi E$ is subtracted from the data. The inset in (a) shows the switching process without any applied electric field.

4.5.2 Influence of the magnetic field strength

In order to reduce the switching costs of the controlled four-state switching, the amplitude of the applied magnetic field has to be reduced. The transition of the magnetoelectric switching happens at approx. 4.5 T. For this reason, the lower boundary $B_{\mathrm{min}} = 4\,\mathrm{T}$ was chosen, as it is far enough away from the switching field. The upper magnetic field B_{max} was reduced gradually from 12 T to 4.5 T to find the field where no switching is happening any more. This experiment was performed for the switching between states 1 and 4 (figure 4.8a-e), states 2 and 3 (figure 4.8f-j), and for the four-state switching (figure 4.8k-n). For B_{max} between 7 T and 12 T no major difference was observed, so they're not shown here. When ramping the magnetic field between 4 T and 4.5 T, the polarization doesn't change much and is reversible when changing the ramping direction (see figure 4.8a,f,k). For $B_{\mathrm{max}} = 5\,\mathrm{T}$, a clear hysteresis opens up and the different polarization states become distinguishable. Increasing the maximum magnetic field further, slightly increases the total amplitude of the polarization, but for $B_{\mathrm{max}} \geq 6\,\mathrm{T}$, the polarization doesn't change much any more. So switching the magnetic field from 4 T to 6 T and back seems to be sufficient in order to create distinguishable polarization states.

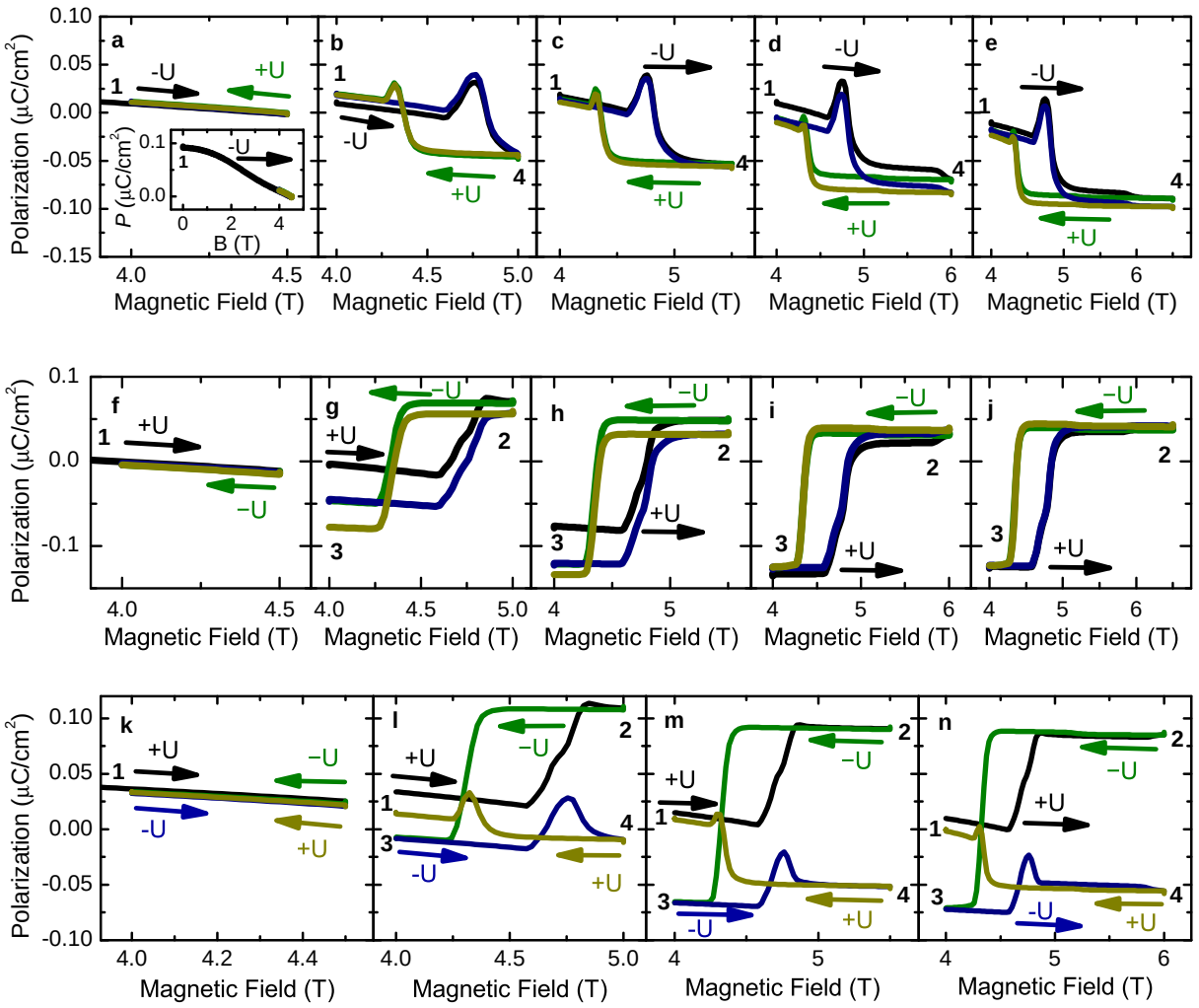

Figure 4.8: Magnetoelectric switching with varying minimum and maximum magnetic field. The lower B-field is set to 4 T, the high field is gradually reduced from 6.5 T to 4.5 T. (a)-(e) show the switching between states 1 and 4, (f)-(j) show the switching between states 2 and 3, and (k)-(n) show the four-state switching.

In order to find the onset of the hysteresis curve, this measurement was repeated with maximum magnetic fields between 4.5 T and 5 T. Figure 4.9 shows these measurements for $B_{\max} = 4.6 - 4.8$ T in 0.05 T steps. Alternating voltages of -150 V and $+150$ V where applied which resembles the sequence for the switching between states 1 and 4 and each loop was measured two times. Already at $B_{\max} = 4.6$ T a hysteresis curve opens up, which gets larger for increasing magnetic fields.

4.5.2.1 "Drift" of electric polarization

Interestingly, a change in polarization is observed while staying at the maximum magnetic field in all of the measurements shown in figure 4.9 despite any parameter is changed.

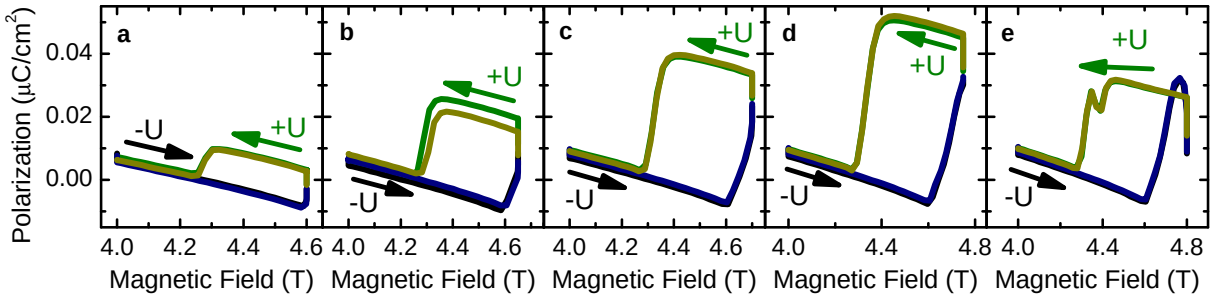

Figure 4.9: Magnetoelectric switching close to the switching field. The lower B-field is set to 4 T, the high field is changed from 4.5 T to 4.8 T in steps of 0.05 T.

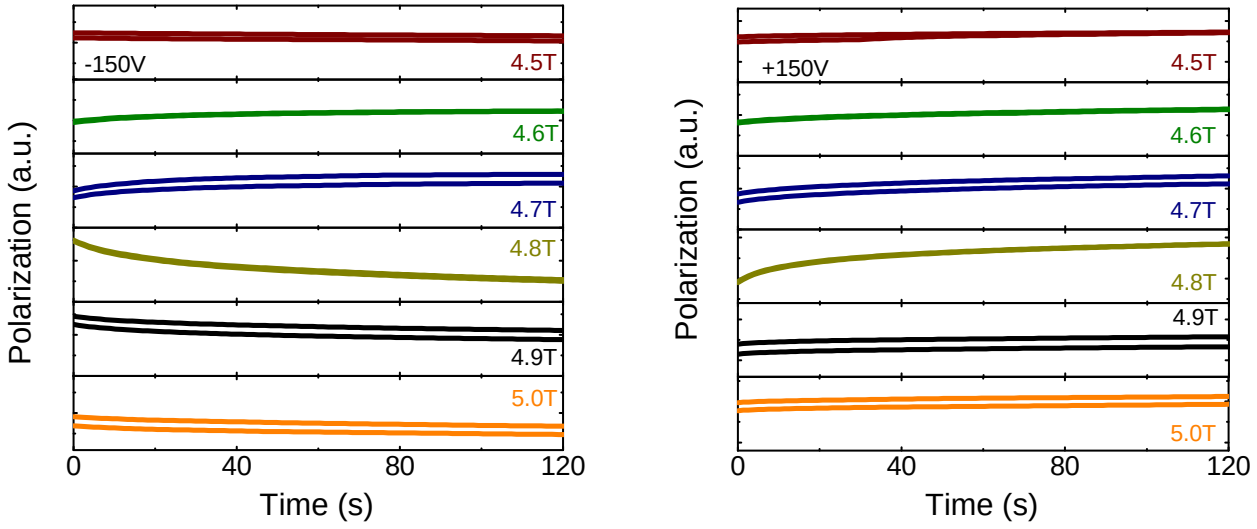

(a) (b)

Figure 4.10: Drift of the electric polarization over time at different $B_{\max}$ before (a) and after (b) changing the applied electric field from $-150\,\mathrm{V}$ to $+150\,\mathrm{V}$. The scaling of each plot is chosen to be $0.018\,\mu\mathrm{C/cm^2}$, for a better comparison.

During the measurements, the magnetic field stays at $B_{\max}$ for approx. 3 minutes, before it is reduced again. So the system shows a measurably strong change in electric polarization just by waiting 3 minutes, which is not observed in the experiments with magnetic fields above 6 T.

To understand this puzzling behavior, this drift was measured in more detail before and after changing the electric field at $B_{\max}$. So the measurement from before is repeated: The magnetic field is increased from $B_{\min}$ to $B_{\max}$ with negative voltage applied and then the drift is measured at $B_{\max}$ without changing any parameter. Then the voltage is changed from $-150\,\mathrm{V}$ to $+150\,\mathrm{V}$ and the drift is measured again afterwards. The magnetic field is reduced again to $B_{\min}$ where the voltage is reversed again and the cycle is repeated. The drift measurements over time are shown in figure 4.10 for different $B_{\max}$. Each cycle was measured two times.

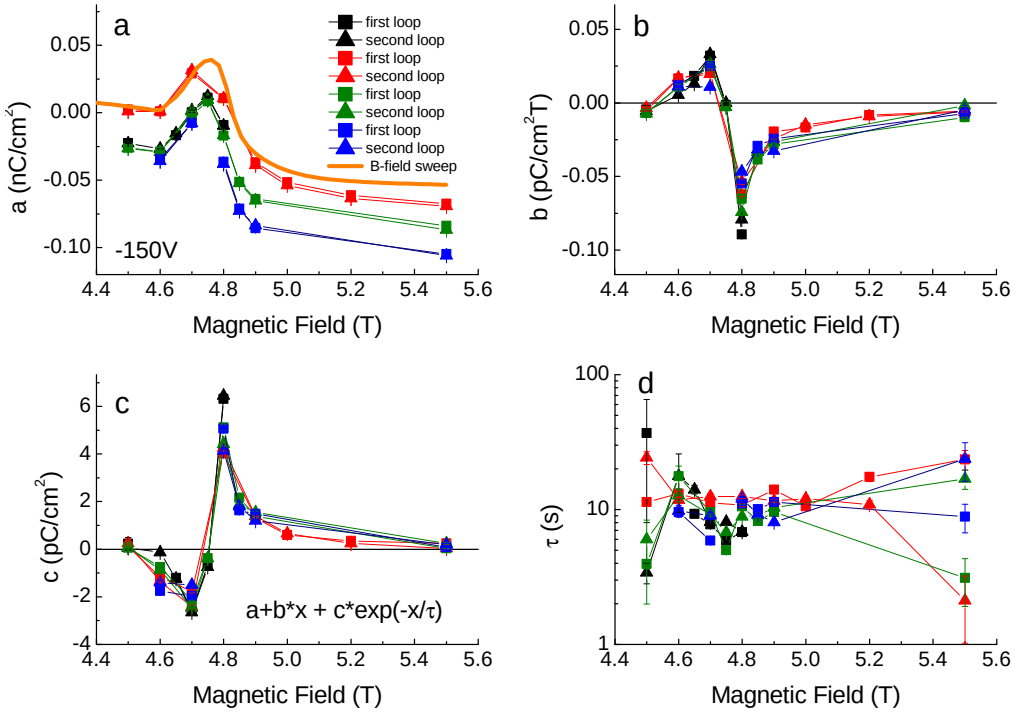

Figure 4.11: Fit results of the measured drift in polarization over time at different magnetic fields before changing the electric field. The fit function is described by equation (4.3). The previously measured behavior of electric polarization when changing the magnetic field is shown in (a) (orange curve) for comparison.

Interestingly, the drift is quite different for different maximum magnetic fields. In most measurements the drift resembles an exponential relaxation of polarization followed by a linear drift over time. Remarkably, this drift even changes its sign at $B_{\mathrm{max}} = 4.8\,\mathrm{T}$ at $-150\,\mathrm{V}$ (figure 4.10a). So just by applying a constant negative electric field and increasing the magnetic field to a certain value, a relaxation process is observed.
Due to its shape, the relaxation in polarization P over time t can be described with an exponential relaxation term followed by a straight line

$$P(t) = a + b \cdot t + c \cdot \mathrm{e}^{-t/\tau}\,, \tag{4.3}$$

where a and b are the y-intercept and slope of the straight line, c and τ are the amplitude and relaxation time of the exponential relaxation, respectively. Fitting this expression to the experimentally obtained drift data reveals further information about the nature of this process. The fit results to different drift measurements are shown in figures 4.11 and 4.12 for the drifts before and after switching the electric field.

Remarkably, the fit results are very similar for all eight drift measurements. The y-intercept of the curve in equation (4.3) (fit parameter a) follows the previously measured behavior

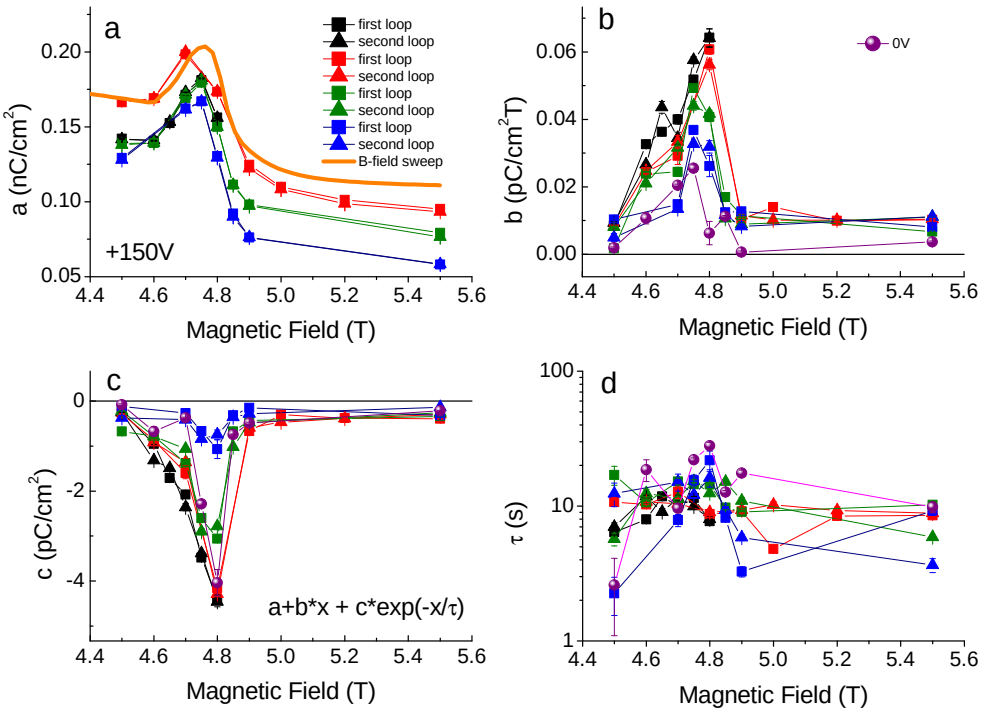

Figure 4.12: Fit results of the measured drift in polarization over time at different magnetic fields after changing the electric field to +150 V. The fit results for the drift measurements after changing the electric field to 0 V are depicted by purple spheres. The fit function is described by equation (4.3). The previously measured behavior of electric polarization when changing the magnetic field is shown in (a) (orange curve) for comparison.

of the electric polarization in an external magnetic field (orange curve in figures 4.11a and 4.12a). This seems reasonable, as the drift in polarization is very small compared to the polarization induced by magnetic fields.
The previously observed direction change of the drift at 4.75 T before switching the electric field (at -150 V) implies a sign change of the fit parameter c (amplitude of exponential decay) from negative to positive values, which could be reproduced in all the measurements (see figure 4.11c).
At the same magnetic field the constant drift (parameter b) also changes sign from positive to negative values (figure 4.11b). This shows that there is something interesting happening in the sample at 4.75 T.

After changing the electric field from -150 V to $+150$ V, this sign change in the parameters b and c is not observed any more (figure 4.12b and c). That means, we can achieve some form of switching in the material only by changing the electric field. However, the mechanisms of this switching remain unclear.

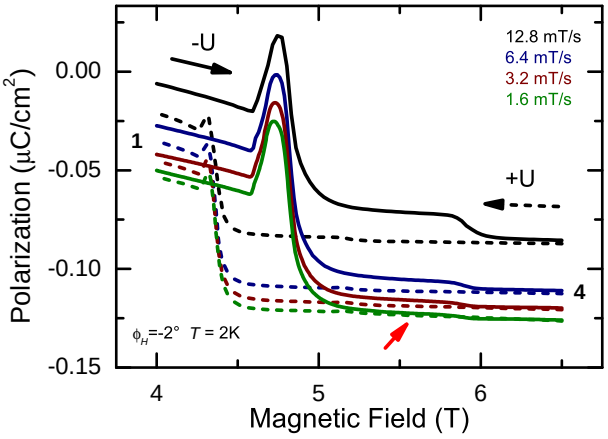

Figure 4.13: Hysteresis loop for different magnetic field sweep rates. The step at 6 T changes drastically depending on the sweep rate. This is indicated by a red arrow.

The relaxation times τ of the exponential decay of the drift over time all lie in the region of 10 s at +150 V and -150 V (figures 4.11d and 4.12d) which gives a reasonable timescale for future experiments.
In some of the drift measurements, the exponential drift could not be observed as the drift was mostly linear. An exponential fit is not very reasonable in these cases which resulted in a relaxation amplitude c close to zero and large error bars on the relaxation time τ (especially at 4.5 T and 5.5 T).

The change of the drift in polarization after the switching of electric field could be reproduced even when switching from -150 V to 0 V. The results at 0 V are also shown in figure 4.12 as purple spheres. It seems sufficient to change the electric voltage from -150 V to 0 V in order to achieve some switching in the material.

4.5.2.2 Different magnetic sweeping rates

As the system shows a drift in polarization over time, this might affect the previously measured two-state loops when the magnetic field is ramped back and forth at very slow rates. For this reason one of the previous measurements was repeated but with varying magnetic field sweep rates. Figure 4.13 shows a measurement where the magnetic field was swept between 4 T and 6.5 T while alternating between positive and negative electric fields in order to switch between states 1 and 2. After each loop, the sweep rate is halved. In all the previous measurements, a magnetic field rate of 12.8 mT/s was used. Reducing this value leads to slightly altered hysteresis curves (figure 4.13). Especially the polarization step at 6 T gets smaller with decreasing field rate. The reason might be the change in polarization over time that was measured previously. This shows that the timescale of the external parameters has a measurable influence on the experiment.

4.6 Summary

Polarization measurements on a single crystal $GdMn_2O_5$ were performed in magnetic fields with varying magnetic field tilt with respect to the crystallographic a-axis. This revealed an angle region, where the electric polarization is reversed when applying a magnetic field ($\phi_H < 8°$) and a region where the polarization stays positive ($\phi_H > 10°$) at all magnetic fields. At the boundary region ($8° < \phi_H^* < 10°$) an unusual four-state hysteresis cycle was observed. This magnetoelectric four-state switching of the electric polarization could be reproduced using a minimal classical spin model. According to this model half of the spins undergo a rotation of about 90° each time the magnetic field is ramped leading to a full-circle rotation when applying and removing a magnetic field two times in a row. This happens due to the asymmetrical evolution of the ground state of the system. The model also shows that the magic-angle region emerges as a topologically protected boundary region between the topologically trivial two-state switching regimes. So the topologically protected four-state switching resembles a mechanical crankshaft that transforms the back and forth motion of magnetic fields to a circular motion of spins. The model also suggests that similar systems with two distinct neighbouring switching regimes might have a novel topological boundary regime with interesting switching properties.
Further it was found, that the application of a constant positive or negative electric voltage during the ramping of magnetic field for $\phi_H < 8°$ influences the polarization reversal process in a way that makes us control the outcome of the switching. We attribute this effect to an additional contribution of the electric field to the energy balance of the system, which seems to be sufficient to overcome certain energy barriers. This makes the observed switching process way more useful for applications, as it can be controlled at each magnetic field sweep. Furthermore, it opens up a new controlled magnetoelectric switching regime where it is possible to recreate the previously observed four-state switching and even modify it in the way we want.
Changing the minimum and maximum magnetic field of the ramping process showed that sweeping the field between 4 T and 6 T is sufficient to clearly observe the switching process and there is no need for magnetic fields up to 12 T.
For maximum magnetic fields close to 4.8 T, an unusual drift in polarization over time consisting of an exponential and a linear term was observed, which was studied in detail. It was found that for different constant magnetic fields, the strength and even the direction of the drift changed drastically. Changing the constant applied voltage from -150 V to +150 V while leaving all others parameters constant lead to a completely different behavior of this drift. For this reason we believe that an external electric field is sufficient to achieve some switching process in the sample. However, the full mechanism of this process is not clear yet and requires further investigations.

5. Superradiance in magnetic resonances of $SmFe_3(BO_3)_4$

In this chapter we show how the theory of quantum optics can be used to describe many-body phenomena in solid state systems. In the first section (section 5.1), the theory of superradiance in quantum optics is introduced. In sections 5.2 and 5.3 the general properties of $SmFe_3(BO_3)_4$ are discussed and the observed excitation conditions of the Sm resonances as well as their directional dichroism are presented, respectively. Finally, in section 5.5, the theory of superradiance is applied to describe the interaction of the Sm resonance with the Fe magnon mode.

5.1 Superradiance

The phenomenon of superradiance was first theoretically introduced by Robert H. Dicke in 1954 [64]. It describes the behavior of an ensemble of N independent two-level systems (for example atoms) coupled to a single bosonic mode (light) with the coupling strength λ. If the atoms radiate incoherently, the intensity of spontaneous emission is proportional to the number of radiators N. For a large density of radiators the system can undergo a superradiant phase transition which leads to a macroscopically excited and highly collective state in which the two-level systems start to radiate coherently with an intensity proportional to N^2.
A recent example for superradiance is the cyclotron resonance in two-dimensional gases which is coupled to the electric field of light. Due to high electron density and narrow resonance conditions, the regime of superradiance in these systems can dominate over the intrinsic damping. The oscillator density can be varied via the gate voltage, which makes it possible to control the coherent radiation [65].
Another way to achieve superradiance is the confinement of cold atoms inside an optical cavity [66–72]. Further, superradiance has been observed in various gaseous and solid-state

samples [73–81]. In all the mentioned cases, the oscillators are coupled to the electric field of light.
In the case of magnetic oscillators it is more difficult to achieve superradiance as the coupling to the magnetic component of light wave is much weaker and the oscillator density is limited due to material parameters. However, recently the the magnetic equivalent of superradiance was observed in yttrium-iron-garnet films where the intrinsic damping of the ferrimagnetic resonance could be separated from the contribution of superradiance in transmission spectra [82].
Another promising way of investigating magnetic superradiance is presented in Ref. [83], where the interaction of spinwaves with the rare-earth crystal-field transitions is studied. Here the spinwaves play the role of the bosonic field and the rear-earth ions are the two-level oscillators.
Based on Refs. [16,84,85], we briefly introduce the mathematical description of the superradiant phase transition in the following section 5.1.1.

5.1.1 Dicke Hamiltonian

The mathematical description of superradiance in this section follows the work of Emary and Brandes [85]. The interaction of N two-level atoms coupled to a single bosonic mode with the coupling strength λ can be written as

$$H = \hbar\omega_0 J_z + \hbar\omega a^\dagger a + \frac{\lambda}{\sqrt{N}}(a^\dagger + a)(J_+ + J_-)\,, \tag{5.1}$$

where $a^\dagger$ and a are the bosonic creation and annihilation operators for a bosonic mode of the frequency ω and J_z and $J_\pm$ describe the angular momentum operators of a fermionic two-level system with a level-splitting of ω_0. $\hbar$ is the reduced Planck constant. In quantum optics this Hamiltonian is often simplified by the rotating wave approximation leading to the Jaynes-Cummings Hamiltonian, which is valid for a weak coupling strength. However, coherent behavior like superradiance only occurs for a sufficiently strong coupling strength, so in our case the Hamiltonian in equation 5.1 has to be diagonalized. In the thermodynamic limit ($N \to \infty$) the diagonalization of the Hamiltonian leads to two independent oscillator modes with the frequencies

$$\omega_\pm^2 = \frac{\omega^2 + \omega_0^2}{2} \pm \sqrt{\left(\frac{\omega^2 - \omega_0^2}{2}\right)^2 + 4\lambda^2\omega\omega_0} \tag{5.2}$$

for the normal phase. So it is possible to describe and observe collective effects in such a system already in the non-superradiant phase. Equation 5.2 also shows that ω_- is only real for $\lambda < \sqrt{\omega\omega_0}/2 = \lambda_c$. Thus, there is a critical coupling strength λ_c at which the system undergoes a quantum phase transition into the superradiant state.

5.1.2 Superradiance in magnetic systems

In this work the knowledge about coherent behavior of resonances is used to search for a possible superradiant phase transition in magnetic materials and describe the collective behavior of resonances for different temperatures and magnetic fields in the ferroborate $Sm_xLa_{1-x}Fe_3(BO_3)_4$, although no phase transition is observed.
The basic idea for superradiance describing an ensemble of two-level systems (fermions) which are coupled to a single light mode (boson) could be transferred to solid-state systems where an ensemble of independent spins interacts with the effective field of a collective magnon mode of other spins. Such a Dicke cooperativity in magnetic excitations was observed recently in erbium orthoferrtite ($ErFeO_3$) [83], where the interaction between the iron magnon mode and the Er spins could be described using the theory of superradiance. However, a superradiant phase transition in this system although theoretically predicted [86] has not been experimentally confirmed yet.

The approach in this thesis is similar to the one described by Li et. al [83]. In order to observe the coherent behavior of superradiance in a solid-state system there need to be a fermionic resonance and a bononic mode which are coupled to each other. In magnetic materials the bosonic mode can be a ferromagnetic or antiferromagnetic magnon mode which is provided by the antiferromagnetically ordered Fe sublattice in $ErFeO_3$ in Ref. [83] and is in our case also present in $Sm_xLa_{1-x}Fe_3(BO_3)_4$. The fermionic oscillators are Er spin resonances and Sm spin resonances which are localized excitations of the rare-earth atom.

5.2 Rare-earth ferroborates

Rare-earth ferroborates $RFe_3(BO_3)_4$ (R = rare-earth) show interesting magnetic phenomena as both the rare-earth and the iron contribute to the magnetic properties. They crystallize in the rhombohedral huntite structure and belong to the space group $R32$ [87]. An example of this structure is shown in figure 5.1 for $SmFe_3(BO_3)_4$. The rare-earth ions (R^{3+}) are surrounded by six oxygen atoms forming a trigonal prism. Each of these oxygen atoms belongs to a different borate group where the B^{3+} ion is in the center of an oxygen triangle. Neighboring rare-earth ions do not share common oxygen atoms, so there is no direct R-O-R interaction. The lattice structure consists of alternating BO_3 and RFe layers within the basal *ab*-plane [88]. Fe^{3+} ions are surrounded by six oxygen atoms forming octahedra [88] which form helicoidal chains of Fe^{3+} ions along the *c*-axis [87]. The iron ions are well separated from each other in the *ab*-plane (4.4 Å) in contrast to the intrachain distances of about 3.2 Å [89].

The rare-earth iron borates undergo a magnetic phase transition between 22 K (La) and 40 K (Ho,Tb, Er) depending on the size of the rare-earth ion [88] where both the iron and rare-earth sublattices order antiferromagnetically. With increasing rare-earth ionic radius the lattice parameters along the *a* and *c* axis increase and the Néel temperature decreases [88].

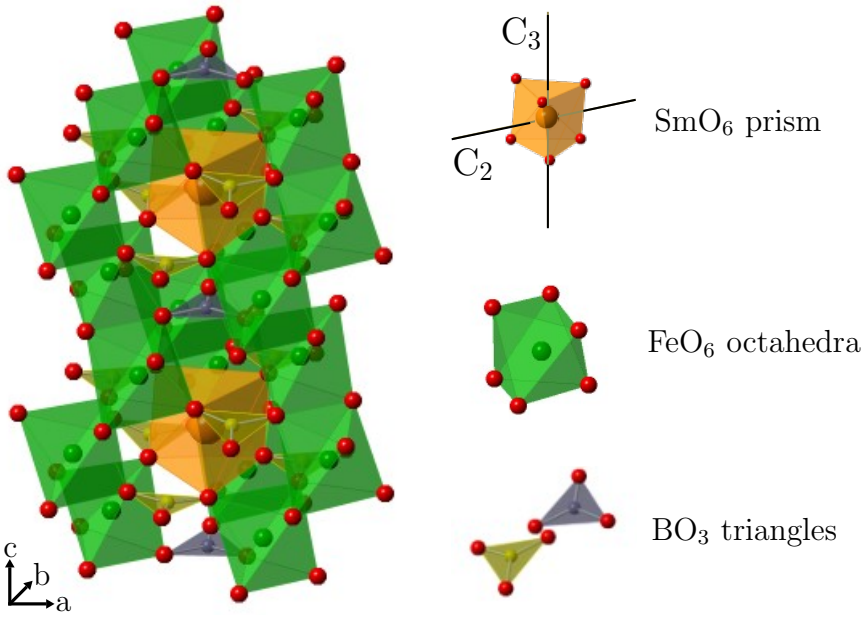

Figure 5.1: Crystal lattice of $SmFe_3(BO_3)_4$. The graphic was made by Dávid Szaller [90].

Due to antiferromagnetic ordering of the Fe and rare-earth ions, there are in total four coupled sublattices which lead to interesting magnetic exchange interactions. In the case of $SmFe_3(BO_3)_4$ the rare-earth sublattice shows a strong polarization. Due to the absence of direct R-R interactions it is believed that the rare-earth sublattice is polarized through the iron sublattice which indicates a strong R-Fe exchange interaction [91]. This can be seen in neutron scattering experiments which show a non-Brillouin type behavior of the Fe-magnetization [89,92,93] and in spectroscopic experiments measuring the ground doublet splitting of the rare-earth ion [94,95]. It will also be demonstrated in the data below.
Additionally, the recent discovery of multiferroic properties in several rare-earth iron borates lead to great interest in this topic [96–101].

5.3 Properties of $SmFe_3(BO_3)_4$

Samarium iron borate $SmFe_3(BO_3)_4$ is of high interest because of its static and dynamic magnetoelectric properties like a colossal magnetodielectric effect and directional dichroism [27,101,102]. It orders antiferromagnetically at 34 K with the magnetic propagation vector $\kappa = [0\ 0\ 3/2]$ [88,89] which is typical for $RFe_3(BO_3)_4$ (R = Pr, Nd) with the $R32$ structure [93,103]. Optical [104] and neutron-scattering experiments [89] showed that $SmFe_3(BO_3)_4$ is an easy-plane antiferromagnet.

5.3.1 Samples

In this work three different samples of $Sm_xLa_{1-x}Fe_3(BO_3)_4$ (x = 0.25, 0.5, 1) are investigated. Their dimensions are shown in table 5.1. The samples were grown by crystallization

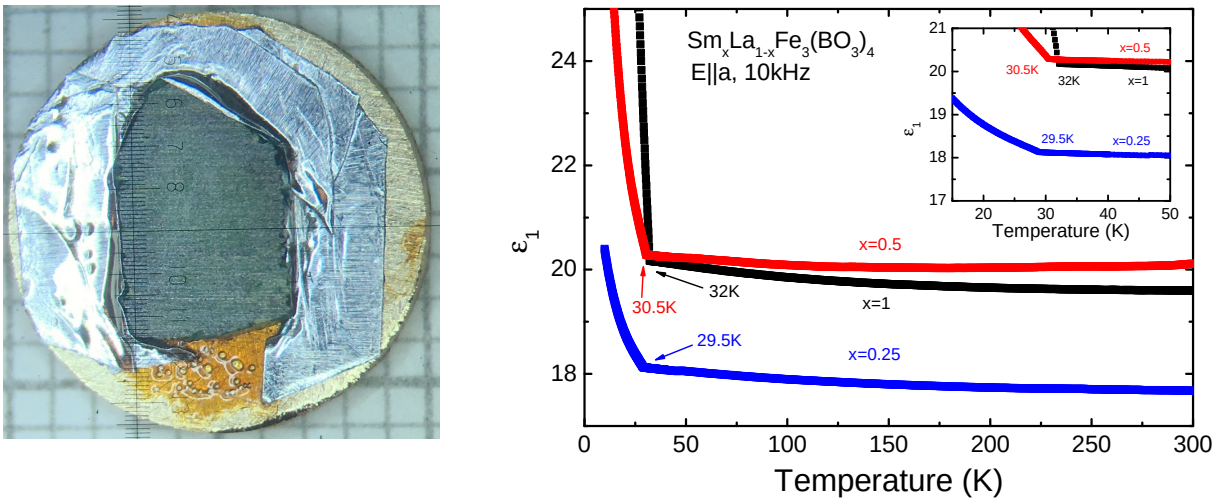

(a) (b)

Figure 5.2: (a) Picture of the $Sm_{0.25}La_{0.75}Fe_3(BO_3)_4$ sample. (b) Capacitive measurements of $SmFe_3(BO_3)_4$ (black), $Sm_{0.5}La_{0.5}Fe_3(BO_3)_4$ (red) and $Sm_{0.25}La_{0.75}Fe_3(BO_3)_4$ (blue) for $E \parallel a$ at 10 kHz. The AFM phase transition can be seen for all three samples at around 30 K.

Table 5.1: Dimensions and Néel temperatures of the three samples that were measured for this thesis.

Sample	Dimensions	Néel temperature
$SmFe_3(BO_3)_4$	5 x 5 x 2 mm^3	32 K
$Sm_{0.5}La_{0.5}Fe_3(BO_3)_4$	2.5 x 2 x 0.4 mm^3	30.5 K
$Sm_{0.25}La_{0.75}Fe_3(BO_3)_4$	4 x 4 x 1 mm^3	29.5 K

from the melt on seed crystals as described in Ref. [105].
To obtain information about the resonances in the material, the three samples were glued on a copper aperture and measured optically in the THz regime in transmission geometry. A picture of the $Sm_{0.25}La_{0.75}Fe_3(BO_3)_4$ sample is shown in figure 5.2a.
The Néel temperature of the samples is expected to decrease with decreasing Sm concentration. To get the exact temperature of the AFM phase transition, capacitive measurements in a PPMS (see section 3.3.2) were performed on all three samples. The results are shown in figure 5.2b. The electric permittivity is nearly constant from 300 K down to 30 K. At approximately 30 K, the material undergoes an antiferromagnetic phase transition which can be seen seen as a kink in the electric permittivity. The Néel temperatures T_N extracted from this measurement are shown in table 5.1.

5.4 Resonances of $SmFe_3(BO_3)_4$

The different $Sm_xLa_{1-x}Fe_3(BO_3)_4$ samples have been investigated using a Time-Domain Terahertz Spectrometer (zero-field) and a Fourier-Transform Infrared Spectrometer to measure terahertz spectra in magnetic fields of up to 32 T. Both setups are explained in more detail in chapter 3.1 and 3.2, respectively.

A zero-field TDS-measurement at 2.8 K and 50 K is shown in figure 5.3a. The transmission spectra in figure 5.3a show a clear difference for the measurements above and below the Néel temperature. At 50 K no resonances are observed in the THz region. Below T_N the AFM ordering of the Fe and Sm sublattice gives rise to multiple resonances of coupled Fe and Sm spins. These excitations strongly depend on the temperature, magnetic field and polarization of the magnetic and electric component of light.
At 3 K these excitations have energies of 0.32 THz, 0.42 THz, 0.49 THz, 1.04 THz (see figure 5.3a) and 0 THz in zero-field. The 0 THz mode increases with magnetic field which can be seen in figures 5.7 and 5.8a.
Figure 5.3 shows the temperature dependence of the modes in zero-field: The excitation frequencies of 0.32 THz, 0.42 THz and 0.49 THz (at 2.8 K) decrease with increasing temperature and vanish close to T_N. The 1.04 THz resonance at 2.8K is less temperature dependent and gets weaker with increasing temperature. The reason for this temperature dependence is discussed in the next section. The excitation conditions of each mode are discussed in section 5.4.2.
Above the Néel temperature there is no ordering in the Fe- and Sm-sublattice, so there are no gapped excitations to observe. Only the paramagnetic Fe mode exists and can be seen in magnetic field measurements where its frequency increases linearly with the external B-field (see figure 5.4).

5.4.1 Ground state splitting of the $SmFe_3(BO_3)_4$ Kramers doublet - Temperature dependence of the resonances

The resonances in $SmFe_3(BO_3)_4$ emerge, when the temperature goes below T_N. The reason is that the degeneracy of the ground state of the Sm-ion is lifted by the local field of the antiferromagnetically ordered Fe spins. In a free Sm^{3+} ion, the $^6H_{5/2}$ ground state is six-fold degenerate. Due to crystal field-splitting, this degeneracy is partly lifted into three two-fold degenerated states (see figure 5.5a). The Stark splitting of the ground multiplet is 0 cm^{-1} (Λ_4), 135 cm^{-1} (Λ_{56}) and 220 cm^{-1} (Λ_4) [104,106]. The Sm^{3+} ion has an odd number of electrons which means it has a half-integer total spin making it a so-called Kramers-ion. According to the Kramers' degeneracy theorem, the ground state is always two-fold degenerate in a time-reversal symmetric system. This symmetry is broken when a magnetic field is present, which happens at the AFM phase transition of the Fe ions and leads to a splitting of the ground state. The energies of the ground state splitting Δ_0 lie in the THz-regime, so the corresponding excitations can be seen in the measurements in this thesis (figure 5.3).

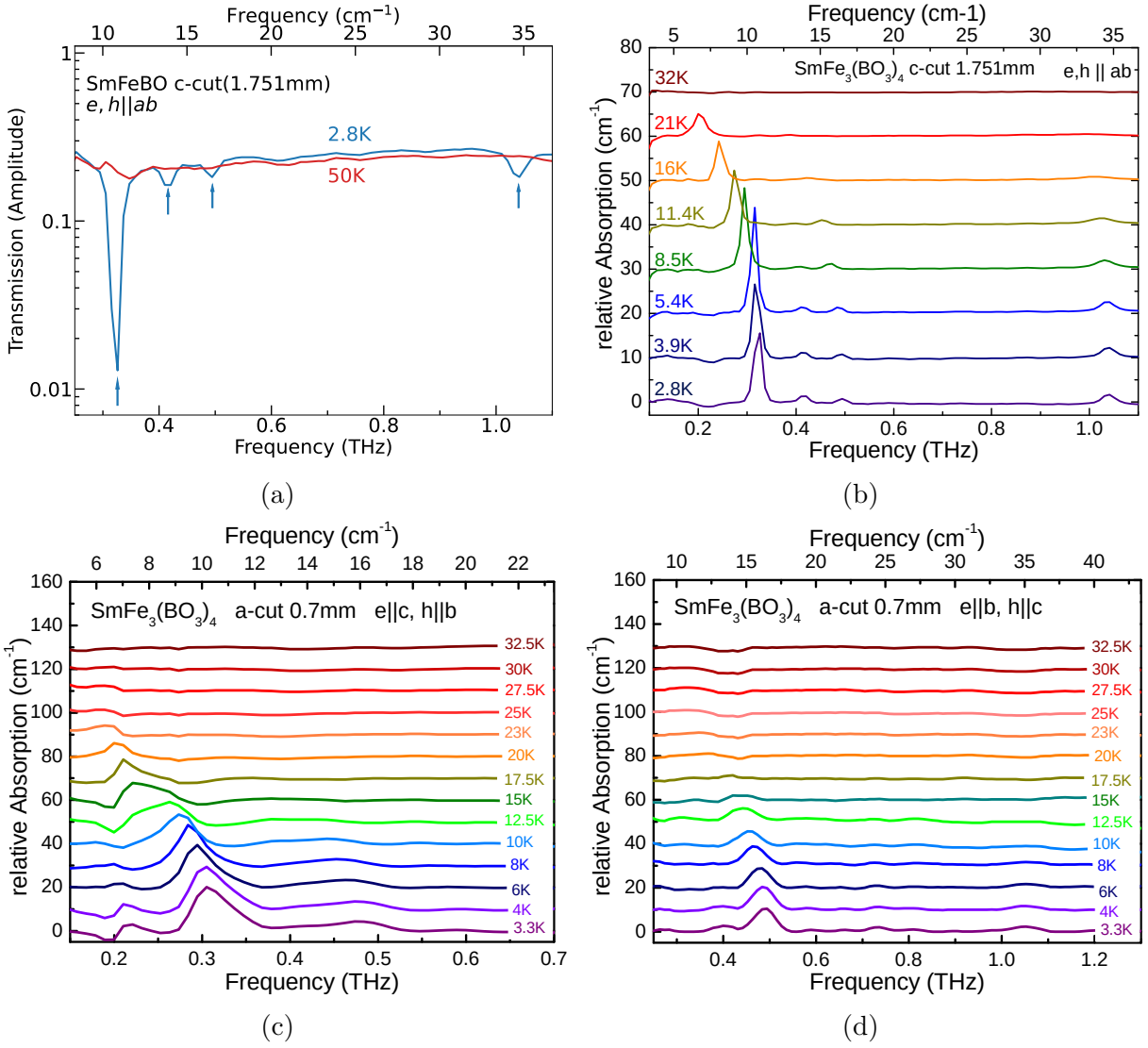

Figure 5.3: Zero-field transmission measurements of $SmFe_3(BO_3)_4$ with a Terahertz Time-Domain Spectrometer at different temperatures. (a) Transmission spectra of a c-cut sample at 2.8 K (blue) and 50 K (red). The spectra are obtained by doing a Fourier Transform of the main peak of the time trace of the TDS measurement. The blue curve shows four excitations at approx. 0.325 THz (10.87 cm^{-1}), 0.415 THz (13.88 cm^{-1}), 0.495 THz (16.51 cm^{-1}) and 1.04 THz (34.69 cm^{-1}) which is indicated by blue arrows. (b)-(d) Absorption plots of a c-cut and a-cut $SmFe_3(BO_3)_4$ sample for different polarizations of light. The median of the measured spectra is used as baseline.

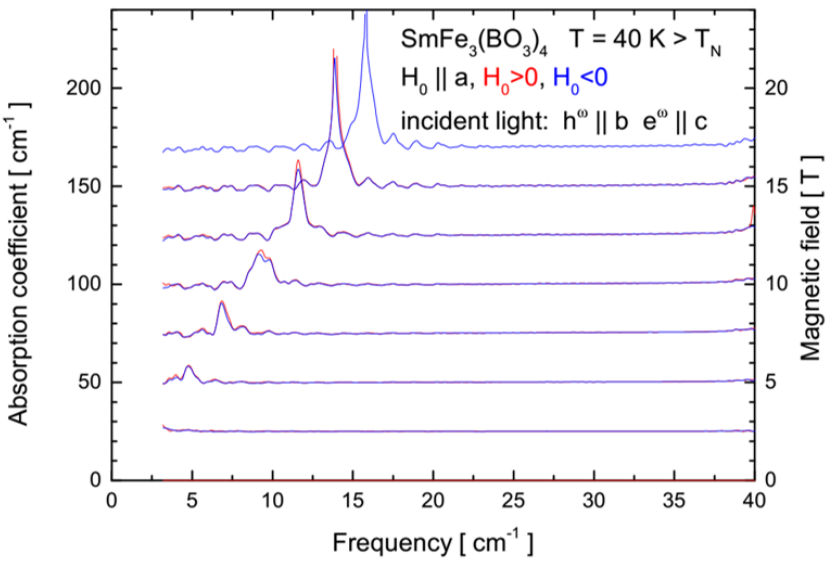

Figure 5.4: Resonance in $SmFe_3(BO_3)_4$ for $T > T_N$. At this temperature only the magnetic resonance of the iron ion is present in this frequency region. The resonance frequency increases linearly with external magnetic field.

The energy splitting of the ground state strongly depends on the strength of the local magnetic field and on the temperature. Without the presence of a magnetic rare-earth ion, in the case of $YFe_3(BO_3)_4$, the magnetic moment of the Fe ions has a typical Brillouin-type temperature dependence of a spin 5/2 ion which means that it increases with decreasing temperature. The ground state energy splitting Δ_0 of the Sm ion follows this behavior which shows that strongly depends on the local magnetic field [104,107]. The Brillouin-type temperature dependence of the Fe magnetic moment and the Sm resonance Δ_0 are shown in figure 5.5b and are also observed in the THz spectra in this thesis (figure 5.10a).

Interestingly, the magnetic moments of the iron ions perfectly follow the Brillouin function in $YFe_3(BO_3)_4$ but slightly deviate from it in $SmFe_3(BO_3)_4$. The reason is that in contrast to the non-magnetic Y-ion, the Sm-ion interacts with the surrounding Fe spins which leads to the observed deviation of the Fe magnetic moments from the Brillouin function [89,108]. This indicates a strong Fe-Sm exchange interaction.
Surprisingly, the Sm resonances can nicely be resolved in the measurements despite its small g-factor of 2/7 which would lead to weak absorption. It is likely that the electronic transition in Sm^{3+} ion is excited through the Fe-sublattice due to their strong exchange interaction [109].

Temperature dependence of the resonances
Because of this strong exchange interaction, all the resonances that are linked to transitions in the Sm^{3+} Kramers doublet, show the typical Brillouin type temperature dependence. That means that with increasing temperature they decrease in frequency and they vanish close to the Néel temperature. In our case this happens for the resonances at $11\,cm^{-1}$,

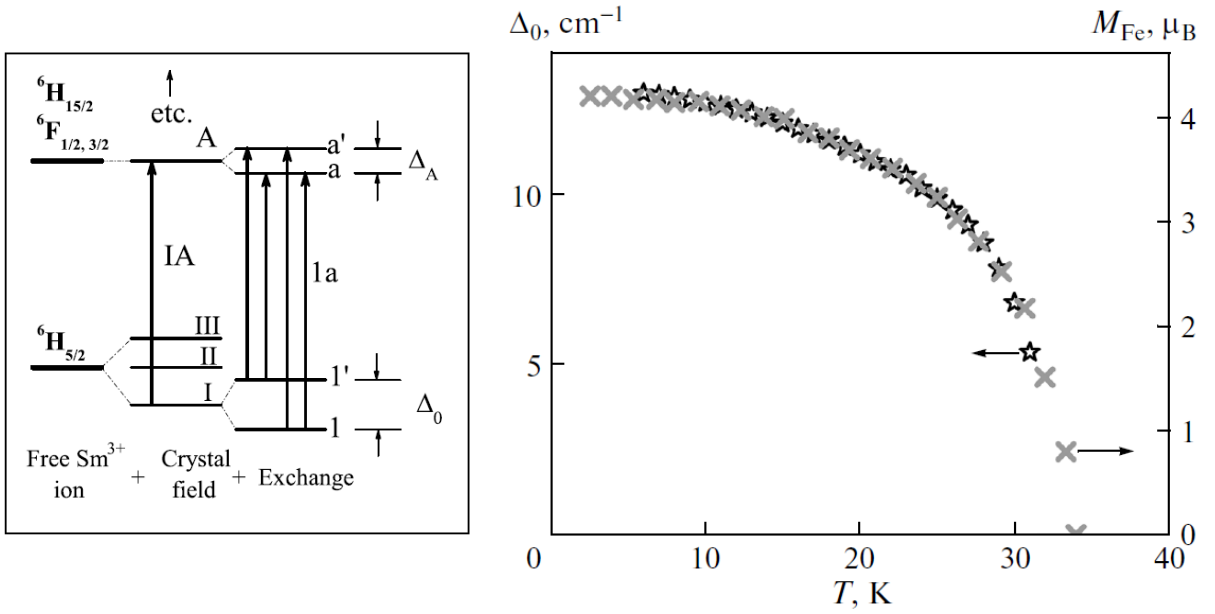

(a) (b)

Figure 5.5: (a) Scheme of the crystal-field levels of the Sm^{3+} ion. The crystal-field levels and their symmetries of the ground multiplet $^6H_{5/2}$ are $0\,cm^{-1}$ (Λ_4), $135\,cm^{-1}$ (Λ_{56}), and $220\,cm^{-1}$ (Λ_4), the ground-state exchange splitting Δ_0 at 1.7 K is $13.2\,cm^{-1}$ when measured indirectly [104]. Graphic taken from Ref. [104]. (b) Temperature dependence of the Sm ground state splitting Δ_0 and the magnetic moment of the iron ion M_{Fe}. Both show a Brillouin type behavior. Graphic taken from Ref. [107].

$14\,cm^{-1}$ and $16.3\,cm^{-1}$ (at 3.5 K) which are coupled Fe-Sm excitations (see figures 5.3 and 5.10a). The $35\,cm^{-1}$ mode does not follow this behavior, thus it might have a different origin. One possibility is a Brillouin-zone edge mode (counter-phase oscillations of spins belonging to neighbouring unit cells), visible in the optical spectra due to the magnetoelectric coupling, as in the case of other multiferroics [110].

Dependency on the Sm-concentration

When the Sm ions are exchanged for other ions, the lattice constant of the unit cell changes, depending on the radius of the ion. In our case, Sm ions are exchanged for larger, non-magnetic La ions, which increases the lattice constant and in return weakens the AFM interactions of the iron ions [88]. Because of the weaker magnetic interactions, the Néel temperature decreases (figure 5.2b) and also the frequency of the Sm excitations decreases (figures 5.7 and 5.11a).

The influence of these dependencies on the Sm-Fe coupling is discussed in section 5.5.1.

5.4.2 Excitation conditions and magnetic field dependence of the resonances in $SmFe_3(BO_3)_4$

Transmission measurements were performed on an a-cut and on a c-cut $SmFe_3(BO_3)_4$ sample for different temperatures and magnetic fields in order to find out the excitation conditions of the resonances. The absorption of $SmFe_3(BO_3)_4$ at 3.5 K in zero-field for different orientations of the electric and magnetic component of the light is shown in Fig. 5.6a, the temperature dependence is shown in figure 5.3 and the behavior in an external magnetic field along the a-axis is shown in figure 5.7. Each mode is discussed in the following. The resonances are labelled by their zero-field frequencies at 3.5 K.

0 cm^{-1} mode
The mode at 0 cm^{-1} is a Fe resonance that can only be seen in the measurements performed in higher magnetic fields as its frequency increases with magnetic field. Above T_N the resonance increases linearly with external magnetic field (figure 5.4), below T_N this mode shows an avoided crossing with the high-frequency 16.3 cm^{-1} Sm resonance (figure 5.8). This avoided crossing is discussed in detail in terms of Dicke cooperativity in section 5.5. Interestingly, this mode is a magnetic excitation that interacts with the electric component of electromagnetic radiation, a so-called electromagnon [20,26]. This mode shows a giant optical activity and a large directional optical anisotropy under certain geometries of the external magnetic field [27]. These conditions are not met in the measurements in this thesis, so this anisotropy is not observed here.

11 cm^{-1} mode
According to Kuzmenko et al. [111] the mode at about 11 cm^{-1} is a coupled Fe-Sm antiferromagnetic mode of purely magnetic character which can be excited with light where the magnetic component is perpendicular to the antiferromagnetic **L** vector. Without any external magnetic fields, the Fe spins lie homogeneously distributed in the $ab-$plane due to different domains (shown in Fig. 5.6b) and can be excited with the magnetic component of light in the ab-plane [111] which is clearly seen in Fig. 5.6a.
If an external magnetic field is applied along the a-axis, the homogeneous distribution of spins is destroyed which is sketched in figure 5.6b. This changes the excitation condition for this mode to $h \parallel a$ [111]. For this reason the mode vanishes in the measurements shown in figure 5.7b as soon as a magnetic field is applied along the a-axis. The magnetic field dependence of this resonance is investigated in detail in Ref. [111].

14 cm^{-1} mode
The resonance at 14 cm^{-1} has not been investigated in such detail yet as it is quite weak. According to our experiments it follows the same excitation conditions as the 11 cm^{-1} mode.

16.3 cm^{-1} mode
The high frequency mode of Sm at 16.3 cm^{-1} is very strong for $e \parallel b$, $h \parallel c$ and weak for $e \parallel c$, $h \parallel b$ and e,$h \parallel ab$ (see Fig. 5.6a). That is a strong evidence for the excitation of

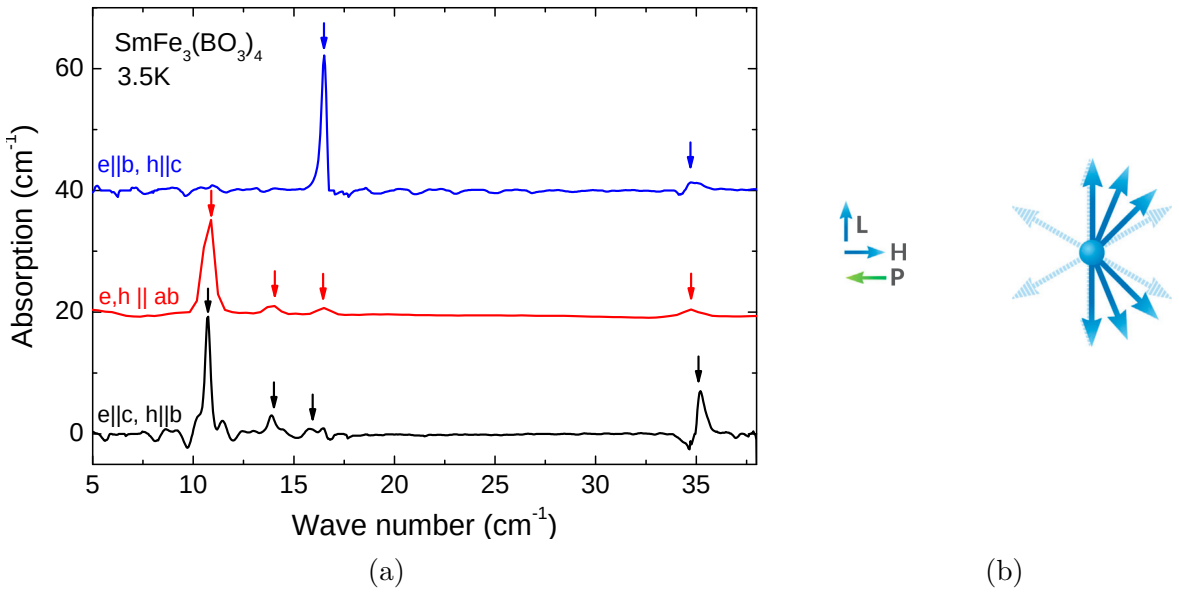

(a) (b)

Figure 5.6: (a) Absorption Spectra of $SmFe_3(BO_3)_4$ for different polarizations of the electric and magnetic component light. The measurements were performed on an a-cut (0.7 mm) and a c-cut (1.751 mm) sample. (b) Homogeneous distribution of Fe spins (light blue arrows) in the ab-plane. When a magnetic field is applied in the ab-plane, the spin-configurations changes (dark blue arrows). Taken from Ref. [111].

this mode through the magnetic component of light for $h \parallel c$ which is in agreement with Ref. [111]. However, this resonance is also visible for $h \nparallel c$, which is either due to a weak excitation through the electric component of light or due to a slight misalignment of the sample which leads to a small contribution of $h \parallel c$.
When applying a static magnetic field along the $a-$axis, the Fe spins change their orientation in the $ab-$plane (see figure 5.6b) which also influences the orientation of Sm spins. They are influenced in such a way that the Sm mode can be partly excited through light with $h \parallel b$ which is shown in figure 5.7b. The excitation is weaker than for $h \parallel c$ because only some the Sm spins are excited. Another explanation of this observation could be Faraday rotation in the sample which leads to a rotation of the polarization plane of the terahertz beam and therefore fulfils the excitation conditions. This could be investigated magnetic field measurements using crossed polarizers .
The strength of the resonance for $h \parallel b$ in an external magnetic field $H \parallel a$ depends on the direction of the constant magnetic field. For $H \uparrow\uparrow a$, the resonance is quite strong, while for $H \downarrow\uparrow a$, the resonance is barely visible between 0 T and 7.5 T and increases in strength for higher magnetic fields (figure 5.7b). So the sample is opaque for light with 17 cm^{-1} in the case of $H \uparrow\uparrow a$ and translucent for $H \downarrow\uparrow a$. This effect is called directional anisotropy, or directional dichroism, and it results in an asymmetry of the absorption

coefficient for the forward and backward direction of propagation of light. In this sample this is equivalent to switching the external magnetic field from +H to −H.

35 cm^{-1} mode
It is likely that this resonance is a zone-edge magnon mode, which can also be observed in $TbFe_3(BO_3)_4$ [112]. It is visible for all measured polarizations and only shows a weak magnetic field dependence.

5.5 Signs of superradiance in $SmFe_3(BO_3)_4$

The magnetic field dependent measurements of the resonances in $SmFe_3(BO_3)_4$ are shown in figure 5.8a. The high frequency Sm-resonance interacts with the Fe magnon which results in an anti-crossing of the two modes. The positions of the resonance frequencies of the two modes are shown in figure 5.8b.
Without interaction, the resonance frequency of the Sm ion would be constant and the frequency of the Fe magnon would increase linearly in an external magnetic field which is indicated by dashed black lines in figure 5.8b. The linear increase of the Fe resonance frequency in a magnetic field B can be seen in the measurements above the Néel temperature where no other resonance is present in the THz region (see figure 5.4). The linear increase of the iron resonance ω_{Fe} follows the linear dependence

$$\omega_{\mathrm{Fe}} = \frac{g\mu_{\mathrm{B}}}{h} B\,, \tag{5.3}$$

where $g \approx 2$ is the Landé factor, μ_{B} is the Bohr magneton and h is the Planck constant. Even though the Sm ion has a g-factor of 2/7, its resonance frequency is expected to be constant in external magnetic fields. The applied magnetic field is way smaller than the local AFM field of the iron ions [101,113,114] and the magnetic moments of the Sm ions are oriented perpendicular to the external magnetic field.

In order to understand the impact of the coupling of the two modes, we can use the theory of superradiance which describes the interaction of independent fermionic two-level systems (Sm resonance) with a single bosonic mode (Fe magnon) for strong coupling strengths λ.

Diagonalizing the Dicke Hamiltonian of the superradiant theory (equation 5.1) leads to equation 5.2 which can be used to describe the upper and lower branch of the observed anti-crossing of the Sm and Fe modes in figure 5.8. The blue and red dashed lines are a fit of equation 5.2 to the measured resonances. For the fits it was assumed that $\omega = \omega_{\mathrm{Fe}} \propto B$ (equation 5.3) increases linearly with external field and that $\omega_0 = \omega_{\mathrm{Sm}}$ is constant with external field. The best fit results were obtained for a coupling strength $\lambda \propto \sqrt{B}$.
In order to verify the assumptions, we use equations 5.2 and 5.3 which leads to

$$\begin{aligned} \omega_+^2 + \omega_-^2 &= \omega_{\mathrm{Sm}}^2 + \omega_{\mathrm{Fe}}^2 \\ \omega_{\mathrm{Sm}} &= \sqrt{\omega_+^2 + \omega_-^2 - \omega_{\mathrm{Fe}}^2} \\ &= \sqrt{\omega_+^2 + \omega_-^2 - \left(\frac{g\mu_{\mathrm{B}}B}{h}\right)^2} \end{aligned} \tag{5.4}$$

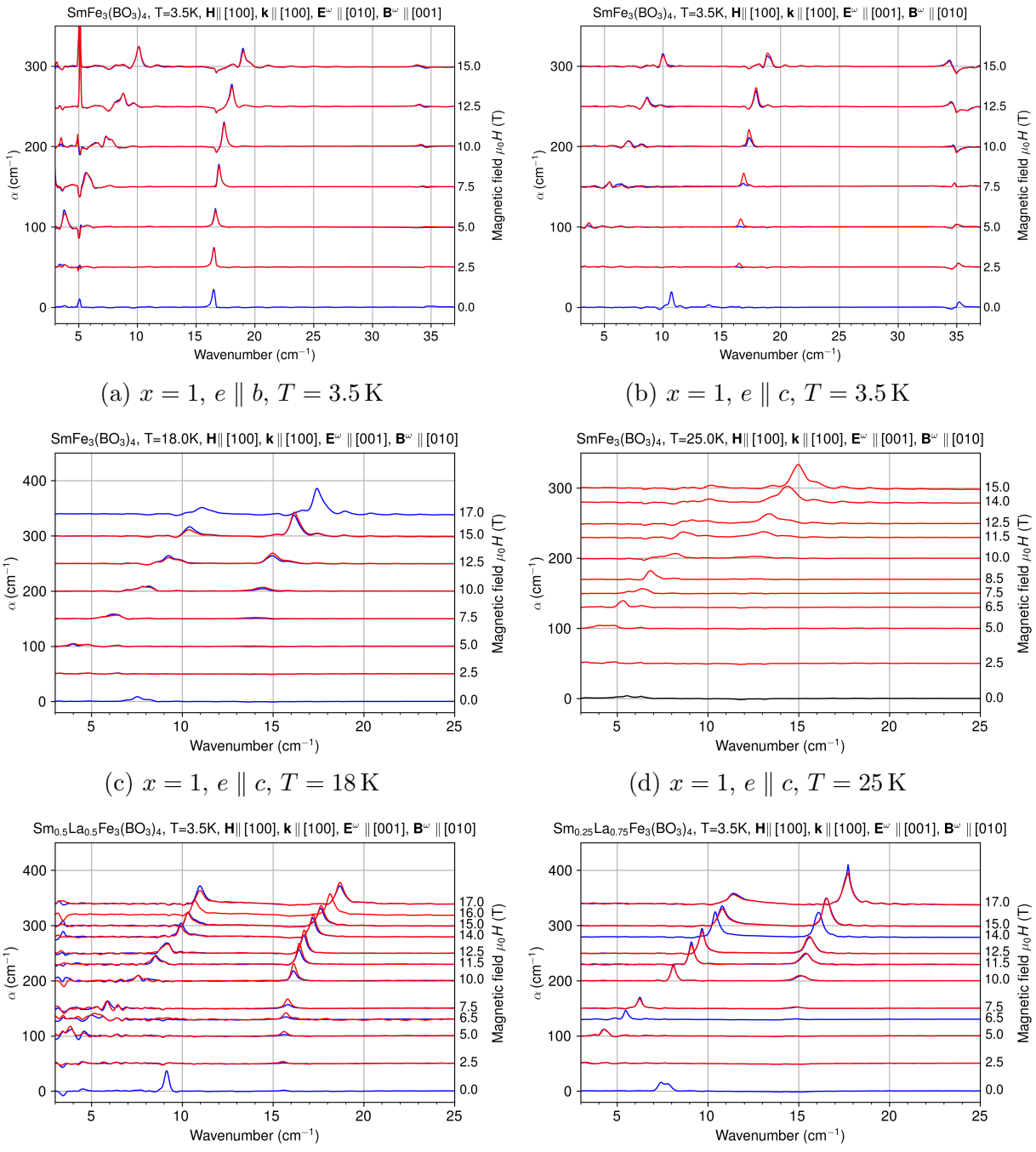

(a) $x = 1$, $e \parallel b$, $T = 3.5\,\mathrm{K}$

(b) $x = 1$, $e \parallel c$, $T = 3.5\,\mathrm{K}$

(c) $x = 1$, $e \parallel c$, $T = 18\,\mathrm{K}$

(d) $x = 1$, $e \parallel c$, $T = 25\,\mathrm{K}$

(e) $x = 0.5$, $e \parallel c$, $T = 3.5\,\mathrm{K}$

(f) $x = 0.25$, $e \parallel c$, $T = 3.5\,\mathrm{K}$

Figure 5.7: Absorption spectra of $Sm_xLa_{1-x}Fe_3(BO_3)_4$ a-cut in magnetic fields $H \parallel k \parallel a$ for different temperatures and polarizations. The measurements at different external magnetic fields are shifted vertically. The dependence of the resonance frequencies on magnetic field is shown in figure 5.8b.

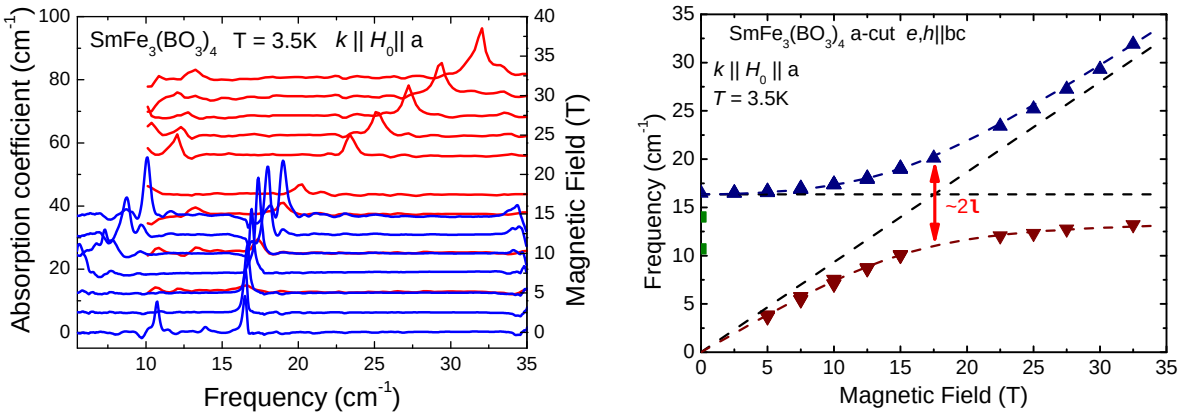

(a) (b)

Figure 5.8: Anti-crossing of the Fe magnon and the Sm spin resonance frequencies of $SmFe_3(BO_3)_4$ in external magnetic field. (a) Absorption spectra of $SmFe_3(BO_3)_4$ a-cut in magnetic fields ($H_0 \parallel k \parallel a$) at 3.5 K . The spectra are vertically shifted to distinguish the different spectra. The blue curves are an average of both polarizations $e \parallel b$ and $e \parallel c$. The red curves were measured without a polarizer (e,$h \perp a$). (b) Positions of the resonance frequencies in $SmFe_3(BO_3)_4$ for different external magnetic fields. The blue and red triangles show the upper and lower branch of the coupled Fe-Sm mode. The anti-crossing can be described with the theory of superradiance. The red and blue dashed line are a fit to the measured data using equation 5.2. The behavior of the Fe and Sm modes without interaction is indicated by the black dashed lines. For the fit it was assumed that $\omega_{\mathrm{Fe}} \propto B$ (equation 5.3), $\omega_{\mathrm{Sm}} = \text{const.}$ and $\lambda \propto \sqrt{B}$. The red arrow is an estimation of the coupling strength of the two modes.

and

$$\begin{aligned} \omega_+^2 - \omega_-^2 &= 2\sqrt{\left(\frac{\omega_{\mathrm{Sm}}^2 - \omega_{\mathrm{Fe}}^2}{2}\right)^2 + 4\lambda^2\omega_{\mathrm{Sm}}\omega_{\mathrm{Fe}}} \\ \lambda^2 &= \frac{1}{4\omega_{\mathrm{Sm}}\omega_{\mathrm{Fe}}}\left[\left(\frac{\omega_+^2 - \omega_-^2}{2}\right)^2 - \left(\frac{\omega_{\mathrm{Sm}}^2 - \omega_{\mathrm{Fe}}^2}{2}\right)^2\right], \end{aligned} \tag{5.5}$$

where ω_+ and ω_- are the experimentally obtained resonance frequencies. The equations are used to calculate ω_{Sm} and λ^2 at each magnetic field which is shown in figure 5.9. The plots seem to verify the assumptions of $\omega_{\mathrm{Fe}} \propto B$ and experimentally confirm that $\omega_{\mathrm{Sm}}(B) = \text{const.}$ and $\lambda \propto \sqrt{B}$ in the studied magnetic field range.

As the coupling strength λ increases with $\sqrt{B}$, it is difficult to compare its value to other experiments. In order to get a comparable constant value for λ, the coupling strength can be estimated by the frequency splitting of the hybridized resonance branches at H_0 [83]. The field H_0 is the magnetic field at which the uncoupled branches would cross, so

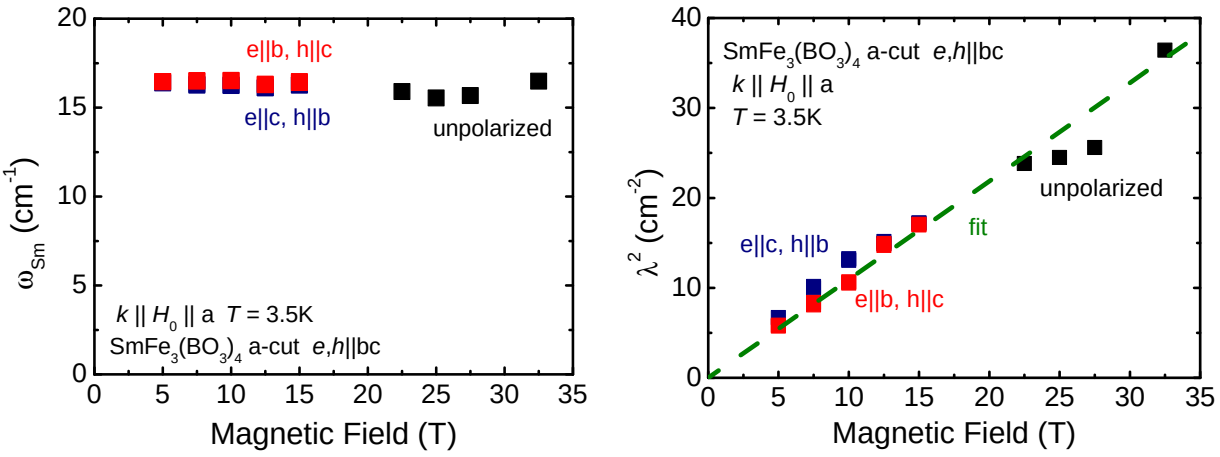

(a) (b)

Figure 5.9: (a) Spin resonance frequency of Sm^{3+} at different magnetic fields calculated with equation 5.4. The frequency of the Sm resonance frequency is expected to stay constant in magnetic fields. (b) Coupling strength λ at different magnetic fields calculated with equation 5.5. It is found that $\lambda \propto \sqrt{B}$.

where $\omega_{\mathrm{Sm}} = \omega_{\mathrm{Fe}}(H_0)$. In our case the coupling strength is estimated to be $\lambda \approx 4.5\,\mathrm{cm}^{-1}$ at $H_0 = 17.5$ and $\omega_{\mathrm{Sm}} = \omega_{\mathrm{Fe}}(H_0) \approx 16.36\,\mathrm{cm}^{-1}$ which is indicated by a red arrow in figure 5.8b. The interaction energy is a comparable fraction of the frequencies of the uncoupled system ($\lambda/\omega \approx 0.28$) which is in the so-called ultrastrong coupling regime ($\lambda/\omega > 0.1$) of quantum optics [115].
With the fit results for λ we can estimate how close we are to the critical coupling strength $\lambda_c = \sqrt{\omega_{\mathrm{Sm}}\omega_{\mathrm{Fe}}}/2$, at which the superradiant phase transition happens. The coupling strength of the Sm spin resonance and the Fe magnon in $SmFe_3(BO_3)_4$ at 3.5 K is found to be approx. 55% of the critical coupling strength ($\lambda/\lambda_c \approx 0.55$). As both λ and λ_c grow with $\sqrt{B}$, their ratio is independent of the magnetic field.

5.5.1 Dependency on temperature and spin density

The values for the coupling strength and the Sm spin resonance change, when the temperature T or the density of Sm spins x is changed which can already be seen when looking at the measurements in figure 5.7. For this reason the same fitting procedure as explained above was realized for several measurements of the three different $Sm_xLa_{1-x}Fe_3(BO_3)_4$ ($x = 1, 0.5, 0.25$) samples at various temperatures.

5.5.1.1 Temperature

The Néel temperatures and the zero-field resonances are different for the three samples. A higher La concentration leads to a larger lattice constant which decreases the AFM

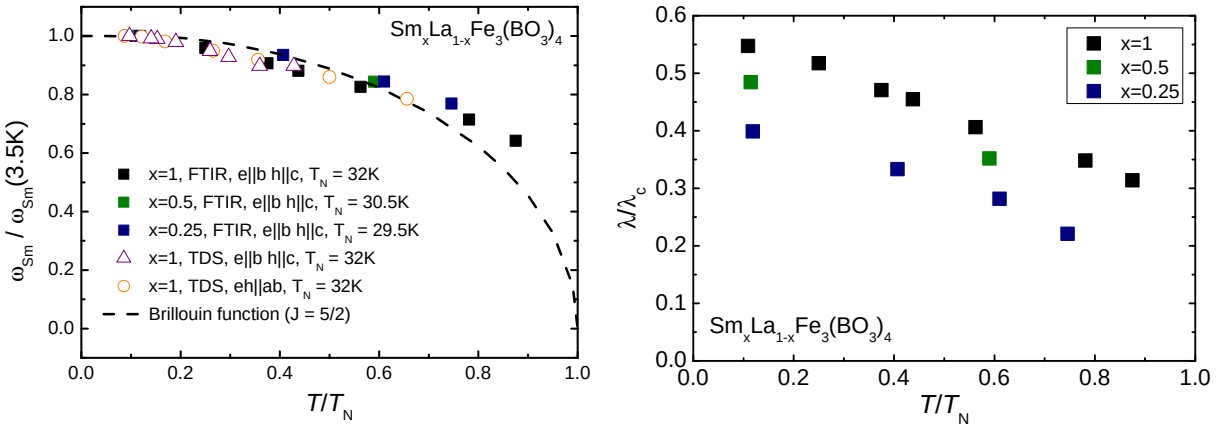

(a) (b)

Figure 5.10: (a) Dependency of the Sm^{3+} spin resonance frequency on the temperature. For better comparison of different samples and measurements, the frequency is normalized to the frequency at the lowest measured temperature $\omega_{\mathrm{Sm}} = 16.35\,\mathrm{cm}^{-1}$, $15.15\,\mathrm{cm}^{-1}$, $14.35\,\mathrm{cm}^{-1}$ for $x = 1, 0.5, 0.25$, respectively. The temperature is normalized to the Néel temperature of each sample. The squares are from fits to the measured anti-crossing in magnetic field with a FTIR. The triangles and circles are TDS measurements at zero-field of an a-cut and c-cut sample. A Brillouin function of a $J = 5/2$ spin is shown for comparison. (b) Dependency of the ratio between coupling strength and critical coupling strength on the temperature. The temperature is normalized to the Néel temperature of each sample.

coupling of Fe spins. This decrease results in a lower Néel temperature and a smaller Sm resonance frequency. See section 5.4.1 for further discussion.
In order to reasonably compare the measurements of the three samples, the temperature is normalized with respect to T_{N} and Sm spin resonance frequency is normalized to frequency measured at the lowest temperature $\omega_{\mathrm{Sm}}(3.5\,\mathrm{K})$ (which is different for all three samples). The values of $\omega_{\mathrm{Sm}}(3.5\,\mathrm{K})$ for the three samples are shown in figure 5.11a.

The dependency of the Sm spin resonance frequency and of the coupling strength on temperature is presented in figure 5.10. As shown in figure 5.10a, the frequency of the Sm spin resonance decreases with increasing temperature and vanishes close to T_{N}. This behavior is also observed for other resonance modes in the material (section 5.4.1). The reason is that with increasing temperature the local magnetic field of the antiferromagnetically ordered Fe spins decreases which reduces the energy splitting of the Kramers doublet of the ground state. This phenomenon is discussed in further detail in section 5.4.1.
The deviation of the measured data from the Brillouin function in figure 5.10a is caused by strong Sm-Fe interaction which was also observed in neutron-scattering and IR experiments [89,108] (see section 5.4.1). Also it is likely that some of the assumptions made for the

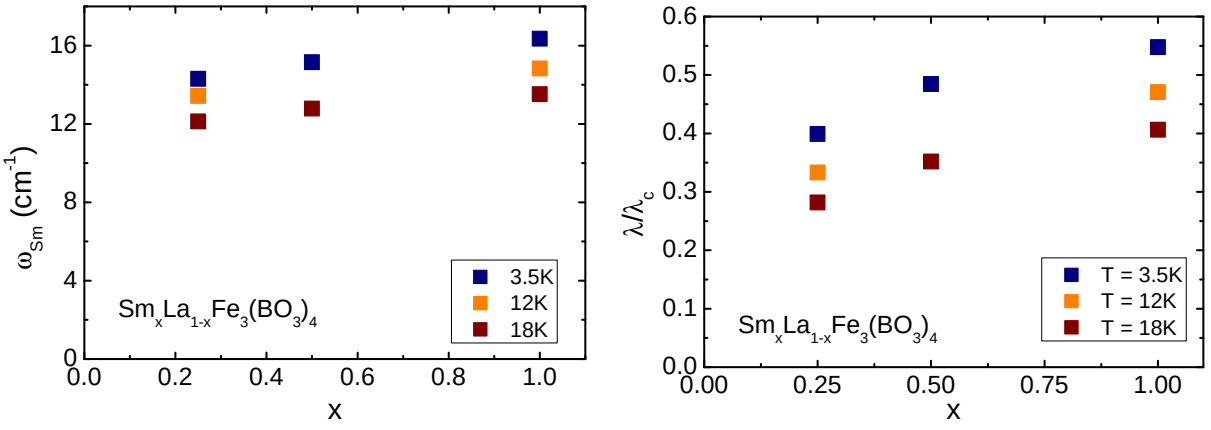

(a) (b)

Figure 5.11: Dependency of the Sm^{3+} spin resonance (a) and of the normalized coupling strength (b) on the Sm spin density in $Sm_xLa_{1-x}Fe_3(BO_3)_4$. The values are obtained from fits to the measured anti-crossing in magnetic field with a FTIR.

model in this chapter are not true anymore when the system comes close to the Néel temperature and the mean-field approximation breaks down.

The coupling strength λ decreases with increasing temperature (figure 5.10b). The interaction strength is directly linked to the local magnetic field of the Fe sublattice which decreases with increasing temperature. Therefore λ decreases with increasing temperature (see figure 5.10b).
The coupling strength is zero above T_N, as the Sm spin resonance only exists for $T < T_N$. As the coupling strength increases with $\sqrt{B}$, it is divided by the critical coupling strength λ_c, which is also proportional to $\sqrt{B}$, in order to compare it to other measurements. The highest coupling strength of $\lambda/\lambda_c \approx 0.55$ is found for $x = 1$ at $T = 3.5\,\mathrm{K}$ (lowest measured temperature).

5.5.1.2 La doping

The behavior of ω_{Sm} and λ/λ_c for different amounts of La and Sm ions in the material is shown in figure 5.11. The spin resonance as well as the coupling strength decrease with decreasing Sm concentration. As explained above, this happens due to the larger La ion radius, which increases the lattice constant and decreases the AFM coupling strength reducing λ. Due to the weaker local AFM field, the splitting of the Sm Kramers doublet is reduced which results in a smaller spin resonance frequency (see section 5.4.1).

5.5.2 Effective spin density

In order to better understand the influence of Sm spins on the scaling of the system, we can calculate the effective Sm spin density n_{spin} that contribute to the Sm-Fe interaction.

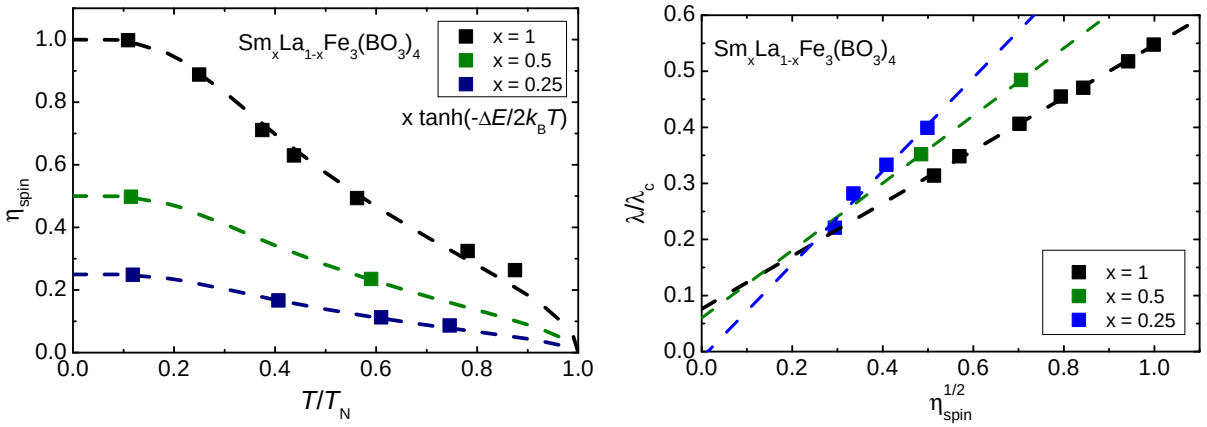

(a) (b)

Figure 5.12: (a) Dependency of the part of contributing Sm^{3+} spins that can interact with the Fe magnon on the temperature. The temperature is scaled with T_N. The colored squares are experimentally obtained data using equation 5.7, the dashed lines are calculated using $\Delta E = \omega_{Sm}(3.5\,K) \cdot B_{5/2}$. (b) Scaling behavior of the coupling strength with the number of contributing Sm spins.

At low temperatures the Sm^{3+} ground state can be approximated to be a two-level system that obeys the Boltzmann statistics as the Stark splitting of the Sm^{3+} ion ($135\,cm^{-1}$) is way larger than the Sm spin resonance at $16\,cm^{-1}$ [104,106]. The population of the quasi spin-up $|\uparrow\rangle$ and spin-down $|\downarrow\rangle$ state of the Sm ion at temperature T can then be described with the Curie law

$$\langle \mu_{Sm} \rangle / \mu_{sat} = \tanh\left(\frac{-\Delta E}{2k_B T}\right) \tag{5.6}$$

where $\langle \mu_{Sm} \rangle$ is the average Sm^{3+} magnetic moment per spin, μ_{sat} is the saturation moment per spin at 0 K, ΔE is the splitting of the Sm^{3+} ion ground state between $|\uparrow\rangle$ and $|\downarrow\rangle$, and k_B is the Boltzmann constant. The ground state splitting ΔE is experimentally measured as $\hbar\omega_{Sm}$, where $\hbar$ is the reduced Planck constant and ω_{Sm} is the measured frequency of the Sm spin resonance. This energy splitting follows the Brouillon $B_{5/2}$ function of a $J = 5/2$ spin (see figures 5.10a and 5.5b), so it can be theoretically modelled with $\Delta E = \omega_{Sm}(0\,K) \cdot B_{5/2}$.
Exchanging Sm ions for La ions in the La doped samples, reduces the spin density by the factor x. The Sm^{3+} spin density n_{spin} is then given by

$$n_{spin} = n^0_{spin}\eta_{spin} = n^0_{spin} x \tanh\left(\frac{-\Delta E}{2k_B T}\right) \tag{5.7}$$

where $n^0_{spin} = 1/V_c$ is the total Sm^{3+} spin density per unit-cell volume V_c and η_{spin} is the fraction of contributing Sm spins.
The dependency of η_{spin} on temperature is shown in figure 5.12a. As one would expect it has its maximum at 0 K and decreases with increasing temperature. It becomes zero at T_N,

as ΔE is zero above T_N. For the samples with different La dopings ($Sm_xLa_{1-x}Fe_3(BO_3)_4$), the total number and therefore the number of contributing spins is scaled with the factor x.

The most interesting observation is the scaling behavior of the coupling strength with the number of contributing spins. Figure 5.12b shows that the normalized coupling strength λ/λ_c increases linearly with $\sqrt{\eta_{\text{spin}}}$. The cooperative enhancement of the coupling strength with $\sqrt{n_{\text{spin}}}$ is a characteristic behavior of superradiant systems.
Moreover, as $\lambda_c = \sqrt{\omega_{\text{Fe}}\omega_{\text{Sm}}}/2$, the coupling strength λ scales with $\sqrt{n_{\text{spin}}\omega_{\text{Fe}}\omega_{\text{Sm}}}$ which means that the Sm^{3+} spins are cooperatively coupled to the Fe magnon field. A similar scaling behavior was also observed in $ErFeO_3$ [83].

5.5.3 Summary

The temperature dependence, magnetic field dependence and excitation conditions of the optically active THz resonances in $SmFe_3(BO_3)_4$ were measured and presented in this chapter. We discussed the interaction of Sm^{3+} spins with the Fe magnon field in terms of Dicke cooperativity in order to explain the observed anti-crossing of the coupled Fe-Sm mode and its behavior with temperature T and external magnetic field H_0. The behavior of ω_{Sm} and ω_{Fe} for different temperatures, different external magnetic fields H_0 and different La dopings x was discussed and the implications on the number of interacting spins and the coupling strength was shown. We found that the cooperative enhancement of the coupling strength λ scales with $\sqrt{n_{\text{spin}}\omega_{\text{Fe}}\omega_{\text{Sm}}}$. The strongest coupling of $\lambda \approx 0.55\lambda_c$ was found for $SmFe_3(BO_3)_4$ at the lowest measured temperature of 3.5 K. When increasing the temperature or exchanging Sm ions for La ions, the coupling strength as well as ω_{Sm} decrease which could be explained with the temperature-dependent splitting of the Sm^{3+} ground state. We don't expect to see a superradiant phase transition in $SmFe_3(BO_3)_4$ at lower temperatures, as the ground state is mostly saturated at 3.5 K and isn't expected to change much with further cooling. However, the application of hydrostatic pressure could enhance the Sm-Fe coupling, and drive the system into the superradiant phase at low temperature.
Besides the avoided crossing in the magnetic field dependence of two resonance modes, the observed directional dichroism also indicates the coupling of magnetic and electric excitations. However, uncovering the exact mechanism connecting the ultrastrong coupling and the directional dichroism exceeds the scope of the present work.

6. Conclusion and Outlook

In this thesis different phenomena in multiferroic materials where investigated by static and dynamic experimental techniques and simulated using theoretical models. As a result, we could extend our knowledge of magnetoelectric switching and of quantum phase transitions like the superradiant phase transition.
The behavior of the ferroelectric polarization of $GdMn_2O_5$ was investigated for different orientations of an external magnetic field of up to 12 T using a Keithley electrometer and a physical property measurement system. When a magnetic field is applied along the a-axis, the electric polarization is reversed at around 5 T. Rotating the magnetic field in the ab-plane by angles larger than 12° leads to a suppression of this process and the electric polarization stays positive. For magnetic field angles of about 9° an unusual four-state hysteresis loop is observed, where the magnetic field needs to be swept by two full cycles in order to reach the initial electric polarization state. This behavior could be understood using a classical spin model, which finds a narrow but robust topologically protected "magic" angle region in which the energy landscape evolves asymmetrically in external magnetic fields. This behavior leads to a unidirectional spin rotation of half of the Gd spins of approx. 90° each time the magnetic field is swept. It was also found that during magnetic field sweeps along the a-axis, the behavior of electric polarization can be controlled through the application of constant electric voltages along the b-axis. The application of a positive (negative) electric field during the field sweep led to positive (negative) electric polarization. So even outside of this "magic" angle region a four-state hysteresis loop of electric polarization can be achieved and it can even be controlled. Further, the range of the magnetic field ramping was reduced and a magnetoelectric switching was still achieved by changing the magnetic field between 4 T and 6 T. An unusual drift of the electric polarization was observed which was different for different external magnetic or electric fields. A transition in the drift behavior was found at around 4.7 T. The reason for this behavior requires further research.
The ability to control the switching of robust polarization states is a promising step

towards the ultimate goal of permanent information storage technologies [116–118]. For this reason we performed additional experiments on $GdMn_2O_5$ in order to better understand and improve the switching process. Further research can be done in similar materials such as $TbMn_2O_5$ or $DyMn_2O_5$. Similar to $GdMn_2O_5$, $TbMn_2O_5$ exhibits an electric polarization along the crystallographic b-axis, which is reversed in magnetic fields along the a-axis [14]. Due to close similarity to $GdMn_2O_5$, this raises hopes of similar multiple magnetoelectric states in this compound in different magnetic field angle. The material $DyMn_2O_5$ also demonstrates a series of magnetic orders and the switching of electric polarization in magnetic fields [15,50,54]. Opposite to $GdMn_2O_5$ and $TbMn_2O_5$, giant dynamic magnetodielectric effects can be expected in this sample in addition to static electric polarization. This offers the possibility to look for new magnetoelectric phases in tilted magnetic fields. In general, the theory derived in Ref. [13] for $GdMn_2O_5$ is not necessarily limited to this material. Materials with two dissimilar neighbouring switching regimes promise the existence of a novel topological boundary regime with exotic properties.

The resonance modes of multiferroic $SmFe_3(BO_3)_4$ were investigated in the THz regime using a THz Time-Domain Spectrometer and a Fourier Transform Infrared Spectrometer. The excitation conditions of each mode were discussed and their temperature and magnetic field dependence was investigated. The frequencies of most of the Sm spin resonances show a Brillouin type temperature dependence below T_N as the splitting of the Kramers doublet of the Sm^{3+} ion is proportional to the local AFM field and therefore dependent on the magnetic moments of the Fe ions. The frequency of the magnetic Fe resonance increases in magnetic fields and shows an anti-crossing with the high-frequency Sm spin excitation. This interaction was measured in detail for different temperatures and $Sm_xLa_{1-x}Fe_3(BO_3)_4$ samples ($x = 1, 0.5, 0.25$) and investigated in terms of Dicke cooperativity. Using the Dicke model, it was possible to fit the upper and lower branch of the anti-crossing and extract the coupling strength of the two interacting resonances. It was found that the coupling strength is in the so-called ultrastrong coupling regime of quantum optics ($\lambda/\omega \approx 0.28$). The strongest coupling strength of approx. 55% of the critical one was achieved for $x = 1$ and at the lowest measured temperature $T = 3.5\,\mathrm{K}$. Reaching the critical coupling strength would result in a superradiant phase transition, where the Sm spins would radiate coherently due to their coupling through the iron magnon field. Increasing the temperature or exchanging Sm ions for non-magnetic La ions resulted in a weaker coupling strength. The coupling strength is not expected to increase further when lowering the temperature due to Brillouin type temperature dependence of the ground state splitting of the Sm ion which is mostly saturated at 3.5 K. So, in $SmFe_3(BO_3)_4$ it is not possible to reach a superradiant phase transition under these conditions. However, even above this phase transition it is possible to measure the effects of this close-lying superradiant phase.
The results of this thesis suggest that it might be possible to achieve superradiance in magnetic materials. Further it is possible to investigate this phenomenon even above the phase transition due to cooperative coupling of fermions and magnons in solid states. It might be interesting to research similar materials like other crystals of the family of rare-earth iron borates or rare-earth orthoferrites. Further, magnetic field measurements

of $SmFe_3(BO_3)_4$ under pressure might reveal exotic phenomena in this material as the decrease of the lattice constant might enhance the cooperative coupling of the resonances.

Bibliography

[1] Bibes, M. & Barthélémy, A. "Towards a magnetoelectric memory". *Nature materials* **7,** 425–426 (2008).

[2] Spaldin, N. A. & Ramesh, R. "Advances in magnetoelectric multiferroics". *Nature materials* **18,** 203–212 (2019).

[3] Khomskii, D. "Classifying multiferroics: Mechanisms and effects". *Physics* **2,** 20 (2009).

[4] Fiebig, M. "Revival of the magnetoelectric effect". *Journal of physics D: applied physics* **38,** R123 (2005).

[5] Fiebig, M., Lottermoser, T., Meier, D. & Trassin, M. "The evolution of multiferroics". *Nature Reviews Materials* **1,** 1–14 (2016).

[6] Cheong, S.-W. & Mostovoy, M. "Multiferroics: a magnetic twist for ferroelectricity". *Nature materials* **6,** 13–20 (2007).

[7] Kleemann, W. "Magnetoelectric spintronics". *Journal of Applied Physics* **114,** 027013 (2013).

[8] Heron, J. *et al.* "Deterministic switching of ferromagnetism at room temperature using an electric field". *Nature* **516,** 370–373 (2014).

[9] Matsukura, F., Tokura, Y. & Ohno, H. "Control of magnetism by electric fields". *Nature nanotechnology* **10,** 209–220 (2015).

[10] Manipatruni, S., Nikonov, D. E. & Young, I. A. "Beyond CMOS computing with spin and polarization". *Nature Physics* **14,** 338–343 (2018).

[11] Bukhari, S. *et al.* "Magnetoelectric phase diagrams of multiferroic $GdMn_2O_5$". *Physical Review B* **94,** 174446 (2016).

[12] Lee, N., Vecchini, C., Choi, Y., Chapon, L., Bombardi, A., Radaelli, P. & Cheong, S. "Giant tunability of ferroelectric polarization in $GdMn_2O_5$". *Physical review letters* **110,** 137203 (2013).

[13] Ponet, L. *et al.* "Topologically protected magnetoelectric switching in a multiferroic". *Nature* **607,** 81–85 (2022).

[14] Hur, N., Park, S., Sharma, P., Ahn, J., Guha, S. & Cheong, S. "Electric polarization reversal and memory in a multiferroic material induced by magnetic fields". *Nature* **429,** 392–395 (2004).

[15] Hur, N., Park, S., Sharma, P., Guha, S. & Cheong, S. "Colossal Magnetodielectric Effects in $DyMn_2O_5$". *Physical review letters* **93,** 107207 (2004).

[16] Hepp, K. & Lieb, E. H. "Equilibrium statistical mechanics of matter interacting with the quantized radiation field". *Physical Review A* **8,** 2517 (1973).

[17] Schmid, H. "Multi-ferroic magnetoelectrics". *Ferroelectrics* **162,** 317–338 (1994).

[18] Chu, Y.-H. *et al.* "Electric-field control of local ferromagnetism using a magnetoelectric multiferroic". *Nature materials* **7,** 478–482 (2008).

[19] Gajek, M., Bibes, M., Fusil, S., Bouzehouane, K., Fontcuberta, J., Barthelemy, A. & Fert, A. "Tunnel junctions with multiferroic barriers". *Nature materials* **6,** 296–302 (2007).

[20] Pimenov, A., Mukhin, A., Ivanov, V. Y., Travkin, V., Balbashov, A. & Loidl, A. "Possible evidence for electromagnons in multiferroic manganites". *Nature physics* **2,** 97–100 (2006).

[21] Szaller, D., Shuvaev, A., Mukhin, A., Kuzmenko, A. & Pimenov, A. "Controlling of light with electromagnons". *Physical Sciences Reviews* **5,** 20190055 (2019).

[22] Saito, M., Taniguchi, K. & Arima, T.-h. "Gigantic optical magnetoelectric effect in CuB_2O_4". *journal of the physical society of japan* **77,** 013705 (2008).

[23] Saito, M., Ishikawa, K., Taniguchi, K. & Arima, T. "Magnetic Control of Crystal Chirality and the Existence of a Large Magneto-Optical Dichroism Effect in CuB_2O_4". *Phys. Rev. Lett.* **101,** 117402 (2008).

[24] Kézsmárki, I., Kida, N., Murakawa, H., Bordács, S., Onose, Y. & Tokura, Y. "Enhanced Directional Dichroism of Terahertz Light in Resonance with Magnetic Excitations of the Multiferroic $Ba_2CoGe_2O_7$ Oxide Compound". *Phys. Rev. Lett.* **106,** 057403 (2011).

[25] Bordács, S. *et al.* "Chirality of matter shows up via spin excitations". *Nature Physics* **8,** 734–738 (2012).

[26] Kuzmenko, A. M. *et al.* "Giant gigahertz optical activity in multiferroic ferroborate". *Phys. Rev. B* **89,** 174407 (2014).

[27] Kuzmenko, A. M. *et al.* "Large directional optical anisotropy in multiferroic ferroborate". *Phys. Rev. B* **92,** 184409 (2015).

[28] Curie, P. "Sur la symétrie dans les phénomènes physiques, symétrie d'un champ électrique et d'un champ magnétique". *Journal de physique théorique et appliquée* **3,** 393–415 (1894).

[29] Landau, L. D. & Lifshitzaad, E. M. "Electrodynamics of continuous media". in (1959).

[30] Dzyaloshinskii, I. E. "On the magneto-electrical effects in antiferromagnets". *Soviet Physics JETP* **10,** 628–629 (1960).

[31] Astrov, D. "The magnetoelectric effect in antiferromagnetics". *Sov. Phys. JETP* **11,** 708–709 (1960).

[32] Neumann, F. & Meyer, O. *Vorlesungen über die Theorie der Elasticität der festen Körper und des Lichtäthers: gehalten an der Universität Königsberg. Vorlesungen über die Theorie der Elasticität der festen Körper und des Lichtäthers: gehalten an der Universität Königsberg* **Bd. 5** (B.G. Teubner, 1885).

[33] Jia, C., Onoda, S., Nagaosa, N. & Han, J. H. "Microscopic theory of spin-polarization coupling in multiferroic transition metal oxides". *Phys. Rev. B* **76,** 144424 (2007).

[34] Sergienko, I. A., Şen, C. & Dagotto, E. "Ferroelectricity in the Magnetic E-Phase of Orthorhombic Perovskites". *Phys. Rev. Lett.* **97,** 227204 (2006).

[35] Katsura, H., Nagaosa, N. & Balatsky, A. V. "Spin Current and Magnetoelectric Effect in Noncollinear Magnets". *Phys. Rev. Lett.* **95,** 057205 (2005).

[36] Popov, A. I., Plokhov, D. I. & Zvezdin, A. K. "Quantum theory of magnetoelectricity in rare-earth multiferroics: Nd, Sm, and Eu ferroborates". *Phys. Rev. B* **87,** 024413 (2013).

[37] Sakai, K. *et al. Terahertz optoelectronics* (Springer, 2005).

[38] Neu, J. & Schmuttenmaer, C. A. "Tutorial: An introduction to terahertz time domain spectroscopy (THz-TDS)". *Journal of Applied Physics* **124,** 231101 (2018).

[39] Withayachumnankul, W. & Naftaly, M. "Fundamentals of measurement in terahertz time-domain spectroscopy". *Journal of Infrared, Millimeter, and Terahertz Waves* **35,** 610–637 (2014).

[40] Fischer, B., Hoffmann, M., Helm, H., Modjesch, G. & Jepsen, P. U. "Chemical recognition in terahertz time-domain spectroscopy and imaging". *Semiconductor Science and Technology* **20,** S246 (2005).

[41] Yamaguchi, K., Kurihara, T., Minami, Y., Nakajima, M. & Suemoto, T. "Terahertz Time-Domain Observation of Spin Reorientation in Orthoferrite $ErFeO_3$ through Magnetic Free Induction Decay". *Phys. Rev. Lett.* **110,** 137204 (2013).

[42] Constable, E. *et al.* "Complementary terahertz absorption and inelastic neutron study of the dynamic anisotropy contribution to zone-center spin waves in a canted antiferromagnet $NdFeO_3$". *Physical Review B* **90,** 054413 (2014).

[43] Gross, R. & Marx, A. *Festkörperphysik* (Walter de Gruyter GmbH & Co KG, 2018).

[44] Möller, K. D. & Rothschild, W. G. "Far-infrared spectroscopy". *New York: Wiley* (1971).

[45] Bergen, L. Far infrared spectroscopy of lattice dynamics in oxides with magnetically frustrated geometry. PhD thesis (Wien, 2022).

[46] Kronig, R. d. L. "On the theory of dispersion of x-rays". *Josa* **12,** 547–557 (1926).

[47] Kramers, H. A. "La diffusion de la lumiere par les atomes". in *Atti Cong. Intern. Fisica (Transactions of Volta Centenary Congress) Como* **2** (1927), 545–557.

[48] Abrahams, S. & Bernstein, J. "Crystal structure of paramagnetic $DyMn_2O_5$ at 298 K". *The Journal of Chemical Physics* **46,** 3776–3782 (1967).

[49] Alonso, J., Casais, M., Martinez-Lope, M., Martinez, J. & Fernandez-Diaz, M. "A structural study from neutron diffraction data and magnetic properties of (R= La, rare earth)". *Journal of Physics: Condensed Matter* **9,** 8515 (1997).

[50] W Ratcliff, I. *et al.* "Magnetic phase diagram of the colossal magnetoelectric $DyMn_2O_5$". *Physical Review B* **72,** 060407 (2005).

[51] Dela Cruz, C. R. *et al.* "Pressure-induced enhancement of ferroelectricity in multiferroic RMn_2O_5 (R= Tb, Dy, Ho)". *Physical Review B* **76,** 174106 (2007).

[52] Noda, Y., Kimura, H., Fukunaga, M., Kobayashi, S., Kagomiya, I. & Kohn, K. "Magnetic and ferroelectric properties of multiferroic RMn_2O_5". *Journal of Physics: Condensed Matter* **20,** 434206 (2008).

[53] Higashiyama, D., Miyasaka, S. & Tokura, Y. "Magnetic-field-induced polarization and depolarization in $HoMn_2O_5$ and $ErMn_2O_5$". *Phys. Rev. B* **72,** 064421 (2005).

[54] Higashiyama, D., Miyasaka, S., Kida, N., Arima, T. & Tokura, Y. "Control of the ferroelectric properties of $DyMn_2O_5$ by magnetic fields". *Physical Review B* **70,** 174405 (2004).

[55] Chattopadhyay, S. *et al.* "Evidence of multiferroicity in $NdMn_2O_5$". *Physical review B* **93,** 104406 (2016).

[56] Fukunaga, M. *et al.* "Magnetic-field-induced polarization flop in multiferroic $TmMn_2O_5$". *Physical review letters* **103,** 077204 (2009).

[57] Fukunaga, M., Sakamoto, Y., Kimura, H. & Noda, Y. "Magnetic phase transitions and magnetic-field-induced polarization flops in multiferroic $YbMn_2O_5$". *journal of the physical society of japan* **80,** 014705 (2010).

[58] Doubrovsky, C. *et al.* "Magnetic phase transitions in $PrMn_2O_5$: Importance of ion-size threshold size effects in RMn_2O_5 compounds (R= rare earth)". *Physical Review B* **86,** 174417 (2012).

[59] Ma, C., Yan, J.-Q., Dennis, K., McCallum, R. & Tan, X. "Synthesis, thermal stability and magnetic properties of the $Lu_{1-x}La_xMn_2O_5$ solid solution". *Journal of Solid State Chemistry* **182,** 3013–3020 (2009).

[60] Giovannetti, G. & van den Brink, J. "Electronic correlations decimate the ferroelectric polarization of multiferroic $HoMn_2O_5$". *Physical review letters* **100,** 227603 (2008).

[61] Chapon, L., Blake, G., Gutmann, M., Park, S., Hur, N., Radaelli, P. & Cheong, S. "Structural Anomalies and Multiferroic Behavior in Magnetically Frustrated $TbMn_2O_5$". *Physical review letters* **93,** 177402 (2004).

[62] Chapon, L., Radaelli, P., Blake, a. G., Park, S. & Cheong, S.-W. "Ferroelectricity induced by acentric spin-density waves in YMn_2O_5". *Physical review letters* **96,** 097601 (2006).

[63] Kim, J.-H. *et al.* "Magnetic Excitations in the Low-Temperature Ferroelectric Phase of Multiferroic YMn_2O_5 Using Inelastic Neutron Scattering". *Physical review letters* **107,** 097401 (2011).

[64] Dicke, R. H. "Coherence in spontaneous radiation processes". *Physical review* **93,** 99 (1954).

[65] Gospodarič, J., Dziom, V., Shuvaev, A., Dobretsova, A., Mikhailov, N., Kvon, Z. & Pimenov, A. "Superradiant and transport lifetimes of the cyclotron resonance in the topological insulator HgTe". *Physical Review B* **99,** 115130 (2019).

[66] Norcia, M. A., Winchester, M. N., Cline, J. R. & Thompson, J. K. "Superradiance on the millihertz linewidth strontium clock transition". *Science advances* **2,** e1601231 (2016).

[67] Norcia, M. A. *et al.* "Frequency measurements of superradiance from the strontium clock transition". *Physical Review X* **8,** 021036 (2018).

[68] Chou, C. W., Polyakov, S. V., Kuzmich, A. & Kimble, H. J. "Single-Photon Generation from Stored Excitation in an Atomic Ensemble". *Phys. Rev. Lett.* **92,** 213601 (2004).

[69] Reimann, R. *et al.* "Cavity-Modified Collective Rayleigh Scattering of Two Atoms". *Phys. Rev. Lett.* **114,** 023601 (2015).

[70] Black, A. T., Thompson, J. K. & Vuleti ć, V. "On-Demand Superradiant Conversion of Atomic Spin Gratings into Single Photons with High Efficiency". *Phys. Rev. Lett.* **95,** 133601 (2005).

[71] Chan, H. W., Black, A. T. & Vuleti ć, V. "Observation of Collective-Emission-Induced Cooling of Atoms in an Optical Cavity". *Phys. Rev. Lett.* **90,** 063003 (2003).

[72] Wolke, M., Klinner, J., Keßler, H. & Hemmerich, A. "Cavity cooling below the recoil limit". *Science* **337,** 75–78 (2012).

[73] DeVoe, R. G. & Brewer, R. G. "Observation of Superradiant and Subradiant Spontaneous Emission of Two Trapped Ions". *Phys. Rev. Lett.* **76,** 2049–2052 (1996).

[74] Scheibner, M., Schmidt, T., Worschech, L., Forchel, A., Bacher, G., Passow, T. & Hommel, D. "Superradiance of quantum dots". *Nature Physics* **3,** 106–110 (2007).

[75] Laurent, T., Todorov, Y., Vasanelli, A., Delteil, A., Sirtori, C., Sagnes, I. & Beaudoin, G. "Superradiant Emission from a Collective Excitation in a Semiconductor". *Phys. Rev. Lett.* **115,** 187402 (2015).

[76] Peyrot, T. *et al.* "Collective Lamb Shift of a Nanoscale Atomic Vapor Layer within a Sapphire Cavity". *Phys. Rev. Lett.* **120,** 243401 (2018).

[77] Mlynek, J. A., Abdumalikov, A. A., Eichler, C. & Wallraff, A. "Observation of Dicke superradiance for two artificial atoms in a cavity with high decay rate". *Nature communications* **5,** 5186 (2014).

[78] Skribanowitz, N., Herman, I. P., MacGillivray, J. C. & Feld, M. S. "Observation of Dicke Superradiance in Optically Pumped HF Gas". *Phys. Rev. Lett.* **30,** 309–312 (1973).

[79] Inouye, S., Chikkatur, A. P., Stamper-Kurn, D. M., Stenger, J., Pritchard, D. E. & Ketterle, W. "Superradiant Rayleigh Scattering from a Bose-Einstein Condensate". *Science* **285,** 571–574 (1999).

[80] Araújo, M. O., Kre ši ć, I., Kaiser, R. & Guerin, W. "Superradiance in a Large and Dilute Cloud of Cold Atoms in the Linear-Optics Regime". *Phys. Rev. Lett.* **117,** 073002 (2016).

[81] Goban, A., Hung, C.-L., Hood, J. D., Yu, S.-P., Muniz, J. A., Painter, O. & Kimble, H. J. "Superradiance for Atoms Trapped along a Photonic Crystal Waveguide". *Phys. Rev. Lett.* **115,** 063601 (2015).

[82] Weymann, L., Shuvaev, A., Pimenov, A., Mukhin, A. A. & Szaller, D. "Magnetic equivalent of electric superradiance in yttrium-iron-garnet films". *Communications Physics* **4,** 1–7 (2021).

[83] Li, X. *et al.* "Observation of Dicke cooperativity in magnetic interactions". *Science* **361,** 794–797 (2018).

[84] Wang, Y. K. & Hioe, F. "Phase transition in the Dicke model of superradiance". *Physical Review A* **7,** 831 (1973).

[85] Emary, C. & Brandes, T. "Chaos and the quantum phase transition in the Dicke model". *Physical Review E* **67,** 066203 (2003).

[86] Bamba, M., Li, X., Marquez Peraca, N. & Kono, J. "Magnonic superradiant phase transition". *Communications Physics* **5,** 3 (2022).

[87] Campá, J. A., Cascales, C., Gutiérrez-Puebla, E., Monge, M. A., Rasines, I. & Ruíz-Valero, C. "Crystal Structure, Magnetic Order, and Vibrational Behavior in Iron Rare-Earth Borates". *Chemistry of Materials* **9,** 237–240 (1997).

[88] Hinatsu, Y., Doi, Y., Ito, K., Wakeshima, M. & Alemi, A. "Magnetic and calorimetric studies on rare-earth iron borates $LnFe_3(BO_3)_4$ (Ln= Y, La–Nd, Sm–Ho)". *Journal of Solid State Chemistry* **172,** 438–445 (2003).

[89] Ritter, C., Pankrats, A., Gudim, I. & Vorotynov, A. "Determination of the magnetic structure of $SmFe_3(BO_3)_4$ by neutron diffraction: comparison with other $RFe_3(BO_3)_4$ iron borates". *Journal of Physics: Condensed Matter* **24,** 386002 (2012).

[90] Szaller, D. Optical study of spin excitations in multiferroic crystals. PhD thesis (Budapest University of Technology and Economics, 2017).

[91] Pankrats, A., Petrakovskii, G., Bezmaternykh, L. & Bayukov, O. "Antiferromagnetic resonance and phase diagrams of gadolinium ferroborate $GdFe_3(BO_3)_4$". *Journal of Experimental and Theoretical Physics* **99,** 766–775 (2004).

[92] Ritter, C., Balaev, A., Vorotynov, A., Petrakovskii, G., Velikanov, D., Temerov, V. & Gudim, I. "Magnetic structure, magnetic interactions and metamagnetism in terbium iron borate $TbFe_3(BO_3)_4$: a neutron diffraction and magnetization study". *Journal of Physics: Condensed Matter* **19,** 196227 (2007).

[93] Ritter, C., Vorotynov, A., Pankrats, A., Petrakovskii, G., Temerov, V., Gudim, I. & Szymczak, R. "Magnetic structure in iron borates $RFe_3(BO_3)_4$ (R = Er, Pr): a neutron diffraction and magnetization study". *Journal of Physics: Condensed Matter* **22,** 206002 (2010).

[94] Chukalina, E., Kuritsin, D., Popova, M., Bezmaternykh, L., Kharlamova, S. & Temerov, V. "Magnetic ordering of $NdFe_3(BO_3)4$ studied by infrared absorption spectroscopy". *Physics Letters A* **322,** 239–243 (2004).

[95] Popova, M., Stanislavchuk, T., Malkin, B. & Bezmaternykh, L. "Phase transitions and crystal-field and exchange interactions in $TbFe_3(BO_3)_4$ as seen via optical spectroscopy". *Journal of Physics: Condensed Matter* **24,** 196002 (2012).

[96] Zvezdin, A. K. *et al.* "Magnetoelectric effects in gadolinium iron borate $GdFe_3(BO_3)_4$". *Journal of Experimental and Theoretical Physics Letters* **81,** 272–276 (2005).

[97] Zvezdin, A. K. *et al.* "Magnetoelectric and magnetoelastic interactions in $NdFe_3(BO_3)_4$ multiferroics". *JETP letters* **83,** 509–514 (2006).

[98] Vasiliev, A. & Popova, E. "Rare-earth ferroborates $RFe_3(BO_3)_4$". *Low Temperature Physics* **32,** 735–747 (2006).

[99] Chaudhury, R. P., Yen, F., Lorenz, B., Sun, Y. Y., Bezmaternykh, L. N., Temerov, V. L. & Chu, C. W. "Magnetoelectric effect and spontaneous polarization in $HoFe_3(BO_3)_4$ and $Ho_{0.5}Nd_{0.5}Fe_3(BO_3)_4$". *Phys. Rev. B* **80,** 104424 (2009).

[100] Kadomtseva, A. *et al.* "Magnetoelectric and magnetoelastic properties of rare-earth ferroborates". *Low Temperature Physics* **36,** 511–521 (2010).

[101] Popov, Y. F. *et al.* "Peculiarities in the magnetic, magnetoelectric, and magnetoelastic properties of $SmFe_3(BO_3)_4$ multiferroic". *Journal of Experimental and Theoretical Physics* **111,** 199–203 (2010).

[102] Mukhin, A. A. *et al.* "Colossal magnetodielectric effect in $SmFe_3(BO_3)_4$ multiferroic". *JETP Letters* **93,** 275–281 (2011).

[103] Fischer, P. *et al.* "Simultaneous antiferromagnetic Fe^{3+} and Nd^{3+} ordering in $NdFe_3(^{11}BO_3)_4$". *Journal of Physics: Condensed Matter* **18,** 7975–7989 (2006).

[104] Chukalina, E., Popova, M., Bezmaternykh, L. & Gudim, I. "Spectroscopic study of the magnetic ordering in $SmFe_3(BO_3)_4$". *Physics Letters A* **374,** 1790–1792 (2010).

[105] Gudim, I., Pankrats, A., Durnaikin, E., Petrakovskii, G., Bezmaternykh, L., Szymczak, R. & Baran, M. "Single-crystal growth of trigonal $DyFe_3(BO_3)_4$ and study of magnetic properties". *Crystallography Reports* **53,** 1140–1143 (2008).

[106] Peschanskii, A., Fomin, V. & Gudim, I. "Raman scattering in multiferroic $SmFe_3(BO_3)_4$". *Low Temperature Physics* **42,** 475–483 (2016).

[107] Popova, M., Chukalina, E., Malkin, B., Erofeev, D., Bezmaternykh, L. & Gudim, I. "Crystal field and exchange interactions in the $SmFe_3(BO_3)_4$ multiferroic". *Journal of Experimental and Theoretical Physics* **118,** 111–123 (2014).

[108] Ritter, C., Vorotynov, A., Pankrats, A., Petrakovskii, G., Temerov, V., Gudim, I. & Szymczak, R. "Magnetic structure in iron borates $RFe_3(BO_3)_4$ (R= Y, Ho): a neutron diffraction and magnetization study". *Journal of Physics: Condensed Matter* **20,** 365209 (2008).

[109] Kuz'menko, A., Mukhin, A. A., Ivanov, V. Y., Kadomtseva, A. M. & Bezmaternykh, L. N. "Effects of the interaction between R and Fe modes of the magnetic resonance in $RFe_3(BO_3)_4$ rare-earth iron borates". *JETP letters* **94,** 294–300 (2011).

[110] Szaller, D. *et al.* "Magnetic anisotropy and exchange paths for octahedrally and tetrahedrally coordinated Mn^{2+} ions in the honeycomb multiferroic $Mn_2Mo_3O_8$". *Phys. Rev. B* **102,** 144410 (2020).

[111] Kuzmenko, A. M. *et al.* "Switching of Magnons by Electric and Magnetic Fields in Multiferroic Borates". *Phys. Rev. Lett.* **120,** 027203 (2018).

[112] Szaller, D. *et al.* "Magnetic resonances of multiferroic $TbFe_3(BO_3)_4$". *Phys. Rev. B* **95,** 024427 (2017).

[113] Eremin, E., Volkov, N., Temerov, V., Gudim, I. & Bovina, A. "Specific features of magnetic properties of rare-earth ferroborates $Sm_{1-x}La_xFe_3(BO_3)_4$". *Physics of the Solid State* **57,** 569–575 (2015).

[114] Weymann, L. "Novel Static and Dynamic Phenomena in Magnetoelectric Materials". *PhD thesis, TU Wien* (2020).

[115] Forn-Díaz, P., Lamata, L., Rico, E., Kono, J. & Solano, E. "Ultrastrong coupling regimes of light-matter interaction". *Rev. Mod. Phys.* **91,** 025005 (2019).

[116] Bhatti, S., Sbiaa, R., Hirohata, A., Ohno, H., Fukami, S. & Piramanayagam, S. "Spintronics based random access memory: a review". *Materials Today* **20,** 530–548 (2017).

[117] Khan, A. I., Keshavarzi, A. & Datta, S. "The future of ferroelectric field-effect transistor technology". *Nature Electronics* **3,** 588–597 (2020).

[118] Zhang, Z. *et al.* "Memory materials and devices: From concept to application". *InfoMat* **2,** 261–290 (2020).

List of Figures

List of Tables

List of Abbreviations

AFM	antiferromagnetic
DC	direct current
FTIR	Fourier Transform Infrared Spectrometer
ME	magnetoelectric
MHz	megahertz
PPMS	Physical Property Measurement System
TDS	Time-Domain Spectrometer
THz	terahertz

List of Symbols

A	area
$a^\dagger$, a	bosonic creation and annihilation operators
B, $\mathbf{B}$	magnetic flux density
$B_{5/2}$	Brillouin function for a spin 5/2 ion
c	vacuum velocity of light
C	capacity
d	sample thickness
E, $\mathbf{E}$	electric field
ΔE	energy of the ground state splitting
f	frequency
F	free energy
g	Landé factor/g-factor
h	Planck constant
$\hbar$	reduced Planck constant
H, $\mathbf{H}$	magnetic field strength
I	intensity of light, current
J_z, $J_\pm$	angular momentum operators for fermions
K	frequency dependent losses at a FTIR
K_L, K_S	easy axis anisotropy constant
k	wave vector
k_B	Boltzmann constant
$\mathbf{L}$	antiferromagnetic Néel vector
M, $\mathbf{M}$	magnetic moment, magnetization
$N = n - \mathrm{i}\kappa$	complex refractive index, number of radiators
n	real part of refractive index
$\mathbf{N}$, $\mathbf{n}$	easy axis vector

P	electric polarization
Q	charge, winding number
$\mathbf{q}$	wave vector
r_{ij}	reflection amplitude coefficient
r, $\mathbf{r}$	distance
S	relevant signal at the detector of a FTIR
$\mathbf{S}$	spin
t	time
t_{ij}	transmission amplitude coefficient
U	voltage
V	volume
T	transmission through a material, temperature
x	mirror position, amount of Sm in $Sm_xLa_{1-x}Fe_3(BO_3)_4$
Z	impedance
$\varepsilon = \varepsilon_1 + \mathrm{i}\varepsilon_2$	dielectric function
β	exchange striction parameters
ε_0	vacuum permittivity
$\Delta\varepsilon$	contribution to dielectric permittivity
μ	magnetic permeability, magnetic moment per spin
μ_B	Bohr magneton
κ	absorption, complex part of refractive index
λ	wavelength, coupling strength
ν	frequency in wave numbers, Heisenberg exchange constant
ϕ	angle
ω	angular frequency, frequency splitting
ω_0	resonance frequency, frequency splitting
γ	damping, linewidth
Δ	difference, energy splitting
τ	relaxation time
χ	electric/magnetic/magnetoelectric susceptibility
η	fraction of contributing spins.

Acknowledgments

Finally, I want to thank all the people who contributed in one or another way to this thesis. Without their support, guidance and knowledge this work wouldn't exist.

- Andrei Pimenov, thank you for the possibility to do this work. Your trust, your guidance and your insights made this work possible. Thank you for always having an open door to ask questions.
- Dàvid Szaller, thank you for including me into your projects right at the start of my thesis and explaining me everything. Thanks to you I had the opportunity to travel to several amazing research facilities and conduct experiments there. Thank you for proof reading this thesis.
- Anna Pimenov, thank you for coordinating the group and helping during the everyday life. Thank you for showing me what happens when art meets science.
- Evan Constable, thank you for sharing your knowledge about a TDS spectrometer and for sharing your curiosity to try out different things in science. It was a pleasure to review all the different ways of brewing coffee with you.
- Alexey Shuvaev, thank you for always being there to answer any questions I had. Especially your knowledge about the PPMS and its data evaluation helped me a lot during my time in the group.
- Lorenz Bergen, thank you for our everyday discussions about everything and nothing. Thanks, for explaining all the little details about life in Austria and at the TU.
- Lukas Weymann, thank you for introducing me to the PPMS and explaining me everything I needed to know to conduct experiments on my own. Thanks for helping me out with the iron borates.
- Jan Gospodarič, Maksim Savchenko, Daniiar Khudaiberdiev, Maxim Ryzhkov, thank you for creating a friendly, fun and productive atmosphere in the office. I enjoyed all our discussions about science, life and lunch options. I hope Alexey can help you with all the administrative problems of Austria, after I left.
- Martin Parzer, thank you for the good teamwork. I hope you enjoyed your time in our group.

- Michael Reissner, thank you for always helping out at the PPMS and explaining me everything I wanted to know.
- Snezana Stojanovic, thank your for your help with orienting the samples using Laue diffraction.
- I want to thank our friendly secretaries for their help with all the administrative and organisational work.
- Artem Kuzmenko, thank you for your insights and discussions about ferroborates.
- Hans Engelkamp and Sanne Kristensen, thank your for your help in conducting high field measurements of the iron borates at the HFML in Nijmegen and for being wonderful hosts.
- Urmas Nagel, Toomas Rõõm and Kirill Amelin, thank you for measuring the iron borates with me at the NICPB Tallinn. Special thanks to Kirill for performing measurements while I gave the instructions remotely due to Covid 19 travel restrictions.
- Sergey Artyukhin and Louis Ponet, thank you for the nice collaboration on the $GdMn_2O_5$ project. It was a pleasure to show you all different kinds of data that you immediately tried to understand and model for us.
- Thanks to my friends for always being there for me despite geographical distances.
- Thanks to my parents for all your love and support. I deeply appreciate everything you've done for me.
- Lena, thanks for everything. I'm grateful for having you in my life.